ULTRASOUND IN REVERBERATING AND ABERRATING ENVIRONMENTS: APPLICATIONS TO HUMAN TRANSCRANIAL, TRANSABDOMINAL AND SUPER-RESOLUTION IMAGING

Danai Eleni Soulioti

A dissertation submitted to the faculty at the University of North Carolina at Chapel Hill in partial fulfillment of the requirements for the degree of Doctor of Philosophy in the Joint Department of Biomedical Engineering of the University of North Carolina at Chapel Hill and North Carolina State University.

Chapel Hill
2022

Approved by:

Gianmarco Pinton

Caterina Gallippi

Paul A. Dayton

Yueh Lee

Omer Oralkan

ABSTRACT

Danai Eleni Soulioti: Ultrasound in reverberating and aberrating environments: applications to human transcranial, transabdominal, and super-resolution imaging
(Under the direction of Gianmarco Pinton)

Ultrasound imaging in the human body is degraded by effects of reverberation and aberration. The heterogeneous acoustical properties of different tissue types distort and reflect the wavefront as it travels to the target and as the echos travel back to the transducer. Transcranial imaging, has been a persistent challenge for ultrasound because the phase aberration, reverberation and attenuation from the human skull reduce the spatial resolution, to a millimeter or more, and limit contrast. Similar challenges arise in human abdominal imaging especially for patients with a large body mass index. Identifying, quantifying, and modeling these complex mechanisms of degradation are a critical component to develop rational strategies that can improve image quality. In this work, an experimental and simulation framework, calibrated to soft tissue measurements, that isolates and characterizes the individual sources of image degradation in ultrasound imaging is established. We show that using this simulation framework we can span the parameter space of image degradation in an independent or orthogonal fashion. Such flexibility offers advantages in the generation of training databases for machine learning applications as well as the development of beamforming strategies for challenging imaging scenarios. We also explored the framework's applications to lung ultrasound imaging, where the interpretation of reverberation artefacts occurring at the pleural surface is used to determine the underlying lung pathology. Using our acoustical simulation tools, B-mode images showcasing primary clinical features used in diagnostic lung imaging were successfully reproduced. These simulations establish a clear relationship of the artifacts to known underlying anatomical structures in a quantitative way. Transcranial simulations in 2D and 3D demonstrate that reverberations, whose role was previously unappreciated, are the principal source of image contrast and resolution degradation at shallow depths below 4 cm and when scattering tissue is present. Finally in the current work, the potential improvements offered by super-resolution imaging were explored by establishing the feasibility of transcranial super-resolution imaging through an intact human

skull at a frequency of 2.5 MHz, with and without applying a phase correction, using with an existing clinical transducer.

TABLE OF CONTENTS

LIST OF TABLES viii

LIST OF FIGURES ix

CHAPTER 1 INTRODUCTION 1

1.1 Sources of image degradation 1

1.1.1 Phase aberration 2

1.1.2 Multiple reverberations 3

1.2 Simulating sound propagation in the human body 4

1.3 Transcranial ultrasound imaging 7

1.4 Super-resolution imaging 8

CHAPTER 2 DECONSTRUCTION AND RECONSTRUCTION OF DEGRADING EFFECTS IN ULTRASOUND IMAGING: ABERRATION, MULTIPLE REVERBERATION, AND TRAILING CLUTTER 11

2.1 Introduction 11

2.2 Methods 15

2.2.1 Sources of degradation 15

2.2.2 Simulations 15

2.2.3 Aberration RMS values 17

2.2.4 Reverberation curves 18

2.2.5 Speckle brightness 18

2.2.6 Coherence curves 19

2.2.7 Isolating components of degradation 20

2.3 Results 20

2.3.1 PSF analysis 20

2.3.2 Anechoic lesion analysis 26
2.4 Discussion 30
CHAPTER 3 QUANTIFICATION OF ABERRATION AND REVERBERATION IN TRANSCRANIAL ULTRASOUND IMAGING 33
3.1 Introduction 33
3.2 Methods 36
3.2.1 Acoustic propagation simulations 38
3.2.2 Skull map calibration 39
3.2.3 Speckle calibration 40
3.2.4 Isolation of the components of image degradation 41
3.2.5 3D Simulations 42
3.3 Results 42
3.3.1 2D transcranial simulations 42
3.3.2 3D transcranial simulations 46
3.3.3 The relative importance of clutter and aberration in image quality 49
3.4 Discussion 50
CHAPTER 4 DIAGNOSTIC ULTRASOUND IMAGING OF THE LUNG: A SIMULATION APPROACH BASED ON PROPAGATION AND REVERBERATION IN THE HUMAN BODY 55
4.1 Introduction 55
4.2 Methods 59
4.3 Results 62
4.4 Discussion & Conclusions 68
CHAPTER 5 ADAPTIVE MULTIFOCUS BEAMFORMING FOR CONTRAST-ENHANCED-SUPER-RESOLUTION ULTRASOUND IMAGING IN DEEP TISSUE 71
5.1 Introduction 72
5.2 Methods 74
5.2.1 Adaptive Multi Focus Sequence 74
5.2.2 Simulation 76

5.2.3 Experimental implementation of the adaptive multifocus sequence 77
5.2.4 Ex vivo experiment 78
5.2.5 Contrast enhanced super resolution imaging 79
5.3 Results 80
5.3.1 Simulations 80
5.3.2 Ex vivo experiment 82
5.4 Discussion and conclusion 84
CHAPTER 6 SUPER-RESOLUTION IMAGING THROUGH THE HUMAN SKULL 87
6.1 Introduction 87
6.2 Methods 92
6.2.1 Phase profile extraction for focal correction 93
6.2.2 Out-of-plane experiment 95
6.2.3 In-plane imaging 96
6.2.4 Simulations 97
6.3 Results 98
6.3.1 Out-of-plane imaging and simulations 98
6.3.2 In-plane transcranial imaging 103
6.3.3 Transcranial rat tail vein imaging 104
6.4 Discussion 106
6.5 Conclusion 110
CHAPTER 7 CONCLUSIONS 111
APPENDIX A PUBLICATIONS AND CONFERENCE PARTICIPATION 112
BIBLIOGRAPHY 113

LIST OF TABLES

1.1 Properties of various biological tissues and liquids [1, 62] 2

2.1 Average magnitudes, relative to the main lobe, of the three regions for a scatterer at 55 mm .. 23

2.2 CNR for the three lesions for different cases. 28

2.3 CNR for the three lesions for different cases of scaled maps..... 29

3.1 The acoustic properties of cortical bone in the skull used in the wave propagation simulations. 37

3.2 Mean magnitude of three PSF regions in dB for different scatterer depths..... 43

3.3 Sound speed and density values for different simulated brain regions. 45

3.4 Average magnitudes in absolute dB values of the three regions in different cases for a spherical target at 40 mm 47

4.1 Bubbles geometry and size description in different modeled lesions. Major (lateral) size (Dl), minor (axial) size (Da), lateral border-to-border distance (Lb) and equivalent volumetric fluid portion (EVFP) in an affected region..... 61

5.1 Comparison of point spread functions for plane wave, fixed focus and multifocus imaging.... 80

5.2 Signal to noise ratio in dB 81

5.3 Comparison of SNR from SVD filtered images for Plane waving imaging, fixed focus imaging and multifocus imaging..... 82

5.4 Comparison of estimated microtube sizes for plane wave and multifocus imaging. 84

6.1 Summary comparison for the experimental B-mode images of the out-of-plane experiment... 100

6.2 Summary comparison for the simulated B-mode images. 100

6.3 Summary comparison for the super-resolved images of the out-of-plane experiment..... 100

LIST OF FIGURES

1.1 A, illustration of sound speed maps for imaging point targets through the human skull at three different depths, namely: B, at 3 cm, C, at 5 cm and D, at 7 cm. No aberration correction has been applied. Gray scale units are in normalized dB. 3

1.2 Phase aberration correction using simulations and experimental methods based on time reversal. 8

2.1 A, in a homogeneous medium, a typical PSF is characterized by three different regions, preceding, trailing and the isochronous volume. In B, aberration degrades ultrasound focusing capability and compromised resolution. In C, multipath reverberation overlays acoustical noise to the echoes produced from the ballistic pulse, thereby reducing detectability. The lengthening of the pulse results in the appearance of trailing clutter. Both reverberation and aberration depend on body wall anatomy. 16

2.2 (A) Example of an input sound speed map for Fullwave2 simulations, as segmented and processed from the selected portion of (B), the visible female abdominal dataset. In (C), the result of a wave propagating through map (A) is shown. Highlighted are different characteristic regions of propagation: (D) is the highly incoherent portion of the wave as it travels through the abdominal wall. As the wave enters the preceding region in (E), coherence increases as it approaches its natural focal zone. In (F) the wave has reached its maximum coherence value at the focus. 17

2.3 A, Experimental B-mode of pork belly immersed in water using the C5-2v probe. B, Simulated B-mode of the visible human dataset used for calibration to experimental data. B-modes are normalized with respect to the maximum of each image. Units are in dB. C, comparison of experimental and simulation reverberation curves for the first 60 mm of depth. D, coherence plots comparison for simulation and experiment at the focal depth (50 mm), in the center of the transducer laterally. 19

2.4 A-E, B-mode images for a target at 55 mm from the transducer normalized by the maximum amplitude of the homogeneous case. A single transmit was used with apodization on half the transducer elements. A, is the homogeneous B-mode, B is the heterogeneous B-mode through the abdomen, C is the isovelocity B-mode. D is the isoimpedance B-mode through clutter subtraction whereas E is the isoimpedance B-mode through setting the isoimpedance to be constant. 21

2.5 Reverberation curves for the heterogeneous, the clutter subtraction and the isoimpedance B-mode images. 22

2.6 Isoimpedance via clutter subtraction B-modes for A, a target at 45 mm, B, a target at 55 mm, C, a target at 65 mm. D, Reverberation curves for B-modes A-C. 23

2.7 B-modes images with trailing clutter linearly subtracted in: A) Isovelocity B-mode, where the trailing clutter is isolated from via either correlation of thresholding at -20 dB in this case. B) The heterogeneous B-mode. C) The isoimpedance B-mode. 24

2.8 B-mode images for impedance mismatch between target and background scaled by background speed of: A, 110% B, 75% C, 40% of background speed. D, reverberation curves for different target impedance mismatch to showcase scaling of the trailing clutter. 25

2.9 Anechoic lesions at 40, 60 and 80 mm, A for the homogeneous case, B for a transabdominal heterogeneous case, and C for an isoimpedance case where the effects of reverberation are removed. D, isovelocity B-mode where the effects of aberration are removed and density is kept at its original value. E, isovelocity B-mode where the effects of aberration are removed and density is scaled to keep impedance constant. F, isovelocity B-mode with density increased by a factor of 4. All lesions are reconstructed from 64 independent transmit-receive events focusing at the depth of the deeper lesion (80 mm) and following the curvature of the C5-2v array. 27

2.10 Anechoic lesion B-mode images for different configurations A-E (top row) and the respective sound speed (middle row) and density (bottom row) maps used to generate each of them. Constant speed maps are used for isovelocity B-modes equal to a homogeneous 1570 m/s. 28

2.11 A, random lesions generated by a lesion generating algorithm. The highlighted porion will be used as an input in Fullwave simulations. B, B-mode image of the lesions in A when used as input in Fullwave in an otherwise homogeneous medium for reference. C, same lesions used through the human abdomen and D, lesions used in an isoimpedance medium. All B-mode images are in dB units and generated using a simulated C5-2v transducer at 3.7 MHz. 30

3.1 Schematic illustrating the effects of multiple reverberations and aberration on a PSF. Homogeneous case provided as a reference. 35

3.2 A, a 2D section of the 3D synchrotron data with an isotropic 10μm resolution. B, the same data set after it has been downsampled to a resolution of 800μm and then interpolated back to a 10μm resolution. C, the envelope detected amplitude of the imaging pulse after propagating through the high resolution map (solid) and the low resolution maps (dashed) shown in A and B. 37

3.3 A, a 2D section of the thin 3D synchrotron data with an isotropic 10μm resolution. B, the same data set after it has been downsampled to a resolution of 800μm and then interpolated back to a 10μm resolution. C, the envelope detected amplitude of the imaging pulse after propagating through the high resolution map (solid) and the low resolution maps (dashed) shown in A and B. 38

3.4 A, experimental B-mode for a 2.5MHz emission through a human skull. B, simulation B-mode using a skull map converted from a CT scan of the same skull specimen. C, reverberation curves for images A and B. 39

3.5 Input field maps for Fullwave2: Sound speed (A), density (B) and attenuation (C). The size of the target at 50mm is exaggerated. 40

3.6 A,homogeneous B-mode of a target at 50 mm. B, transcranial B-mode of the target. C, isovelocity B-mode where all effects of aberration are removed. D, isoimpedance B-mode where the clutter has been subtracted and multiple reverberations are removed..... 41

3.7 A, 2-D sparse array that is simulated in the 3D section of the paper and B, its actual element distribution in space. C-E, sound speed maps derived from a 3D CT scan shown in three different planes. Units are in m/s 43

3.8 PSFs of a point target at (A) 30 mm, (B) 40 mm and (C) 60 mm transcranially. Units are in normalized dB. 44

3.9 PSFs of targets that have their sound speed scaled by A, 10%, B, 20% and C 50% with respect to their original value. D, reverberation curves for the same images. Note how the trailing clutter scales with increasing impedance mismatch. 45

3.10 A, Transcranial B-mode including brain tissue. B, Reverberation curve comparison between simulation including brain and without brain tissue. 46

3.11 PSFs from an unapodized transducer in a homogeneous medium (left) and transcranially (right) for a target at a depth of 50 mm, for the fundamental frequency of 1.25 MHz (A,C) and the first harmonic frequency of 2.5 MHz (B,D). The PSFs have been normalized relative to their peak. All scales have units of decibels. E, beamplots for PSFs A-D. 47

3.12 B-mode images for 3D simulations (second row) corresponding to different imaging scenarios shown schematically (first row). 48

3.13 Anechoic lesions with a 1 cm diameter at different shown at different imaging depths for each row (3, 5 and 7 cm) and for a different imaging scenarios for each column, namely from left to right, for a homogeneous medium, transcranially, transcranially but with the effects of multiple reverberations removed and transcranially but with phase aberration removed..... 52

3.14 A, coherence curves for a homogeneous emission inside and outside the anechoic lesion. Theoretical curve for the ideal case is also shown as reference. B, coherence curves for a transcranial emission, C with the effects of phase aberration removed (isovelocity) and D with the effects of reverberation removed inside and outside the anechoic lesions. All plots generated from lesions at a depth of 3 cm. 53

3.15 Trend of CNR values for the isoimpedance and isovelocity cases as a function of imaging depth. 54

4.1 A, experimental B-mode image using a C5-2v transducer through porcine abdominal tissue. B, equivalent simulation B-mode generated by Fullwave. C, reverberation curves for experiment and simulation..... 60

4.2 Speed of sound map fitted to the final B-mode image size (A) with its magnified version (B) to show the bell-shaped synthetic structure used to model a localized subpleural exudative lung lesion. (C) shows the same image at a higher magnification demonstrating the air bubbles arrangement and size pointers related to Table 4.1. Illustration of the air bubbles' shapes corresponding to the different fluid portions in an affected region: 0.18 (D), 0.55 (E), 0.71 (F), 0.88 (G) and 0.98 (H). 61

4.3 Ultrasound images simulated from an emission through the abdominal wall with different underlying materials: medium of soft tissue properties, B-mode image (A) and corresponding sound speed map (B); underlying straight tissue/air interface mimics pleural line, B-mode image (C). Note horizontal artifacts, A-lines *in silico*. D. Corresponding illustrative sound speed map. E. Curves of acoustic pressure averaged laterally for both cases. Three spikes correspond to hyperechoic pleural line (1st) and A-lines of fading brightness (2nd and 3rd). 63

4.4 Illustration of the pulse propagation and multiple scattering in affected lung region at 5 elected moments in time. Acoustic pressure field (scale is compressed to emphasize small amplitudes). Air elements made visible for illustration purposes, note no sound propagation in the air. A. Ballistic pulse before hitting the lung surface, note trailing clutter. B. The wave is reflected from native lung areas and entering the affected lung region. C. The reflected wave travels back to the transducer, progressive wave propagation and multiple scattering occur in affected lung region. D. Continued backscattering, waves gradually leave the trap. E. Attenuation of the trapped wave, low intensity wave release is persisting. 64

4.5 Ballistic pulse (gray) and subsequent reverberation signals (black) originating from the acoustic trap and measured at its entrance. In red, the fitted exponential on the reverberation curve. 65

4.6 B-mode images showing step wise increase of EVFP in the affected area by: 0.18 (A), 0.55 (B), 0.71 (C), 0.88 (D) and 0.98 (E). Time gain compensation is applied. Note the interrupted vertical line in (B) that demonstrates fusion of bright elements only beneath the first A line. (F) Speed of sound map used to produce image (C) shown as an example, fitted to the final B-mode image size. (G) shows simulated B-mode image of one cm wide subpleural exudative lesion. EVFP in the affected area equals 0.88. Time gain compensation applied. (H) Speed of sound map fitted to the final B-mode image size. 66

4.7 Contrast-to-noise ratio measurement technique and results. (A) B-mode image illustrating the location of the samples: white central bar shows a region of interest (signal), gray ones - background regions (for comparison). No time gain compensation. (B) Plot CNR versus equivalent volumetric fluid portion in the affected region of the lung. 67

4.8 Simulated parasagittal (longitudinal) views with ribs. Note the ”bat sign” which identifies the upper and lower ribs with their acoustic shadows (the wings of the bat) and, a little deeper, the pleural line (the back of the bat). A. Tissue/air interface of concave shape mimics unaffected lung. A-lines *in silico*. B. Corresponding speed of sound map. C. Coalescent B-line *in silico*. Time gain compensation applied. D. Full and zoomed speed of sound maps. Acoustic trap simulates subpleural exudative lesion of size 2x5 mm. Volume portion of fluid in the affected area equals 0.88. ... 69

5.1 (A) Plane wave emission travelling along the vertical direction. (B) Conventional fixed focus sequence. Different colours mark different emissions. A total of 16 beams are propagated, 3 are shown here. (C) Adaptive multifocus sequence. An example emission is shown, with beams emitted following the direction of propagation. 73

5.2 Sound speed map of an abdominal human model. The three black spots represent the point targets artificially added to mimic microbubbles. Note that the size is exaggerated for visualization purposes. The real diameter was one pixel. 75

5.3 Theoretical (A) vs. experimentally realizable (B) focal profiles. Note that (B) represents a hardware, not a fundamental limitation. Different phase profiles and their respective foci are color coded with respect to the two foci. Lines marked as ”excitation of transducer” are repeated throughout the length of the array. 77

5.4 (A) Schematic of the porcine tissue phantom with two embedded microtubes.(B-D) B-mode images for the three imaging techniques. The dynamic range for all the B mode images is 50 dB. 78

5.5 Simulation results in a homogeneous medium (A, B, C) and in a human abdominal model (D, E, F). A and D show the B-mode images from the plane wave emission. B and E show the B-mode images from 16 transmit receive events with a focal depth of 38.5 mm. C and F show the B-mode images using a simultaneous triple targeting focus at the bubble location (note that this consists of a single emission). 80

5.6 SVD filtered image for plane wave imaging (A), fixed focus imaging (B) and adaptive multifocus imaging (C). The dynamic range of all these images was 10 dB. Contrast to tissue ratio was calculated from the tube region (yellow box) and the surrounding tissue region (green box) at the same depth. 81

5.7 Super resolution image reconstructed from plane wave imaging (A) and adaptive multifocus imaging (B). The image intensity is the number of detected microbubble events. The dynamic range is 50 counts. Detected tubes are also shown enlarged. The dynamic range on zoomed images was 200 counts. 83

6.1 Schematic of the experimental setup. A custom 3D printed holder secured the skull in place while a separate tube holder allowed for both tube configurations with 90 degree rotations. 92

6.2 (A) The detected profile of the microtube underneath the skull measured with the correlation detection method (black line), plotted on the RF data. (B) Detected profile of the target without the skull and the target through the skull in time units. The RMS difference between the two profiles was measured as 90.3 ns. 94

6.3 Standard B-mode images for (A) the tube without skull, (B) uncorrected and (C) corrected emissions through skull, all in the out-of-plane direction. Scale for all images is in dB. The amplitude improves by 3.9 dB in the corrected case. 99

6.4 (A) Beamplots for all three experimental cases, the lateral registration error of the tube's position in the uncorrected case was 990 μm and in the corrected case it was 50 μm, as measured in the point target B-mode images. (B) Simulation beamplots for a different position of the skull in the temporal region. Correction was derived from a point source in the place of the target. 101

6.5 Super-resolved images for the (A) uncorrected and (B) corrected emissions through the skull. Scale in both cases is normalized number of bubble counts. 103

6.6 Sum of bubble counts as a function of (A) lateral position and (B) depth, for the uncorrected and corrected super-resolved images. The tube profiles are also provided for reference and registration error estimation ground truth. Sensitivity improves by a factor of 1.48 for the corrected case. 103

6.7 Super-resolved images for (A) the corrected emission through the skull, (B) the uncorrected emission through the skull and (C) the microtube without the skull. Scales are in number of bubble counts. (D) Laterally averaged counts as a function of depth for the corrected and uncorrected images with the skull and the microtube only as reference. Solid boxes show the location from where plot (D) was generated. 105

6.8 Schematic of the setup used for the rat tail vein experiments. 105

6.9 B-mode images of the rat tail vein through a human skull specimen and the zoomed in counterparts for an uncorrected focused emission and a phase corrected focused emission, as labeled. Units are in normalized dB. 106

6.10 Top to bottom: Super-resolved image of the rat tail vein using a corrected transcranial emission, super-resolved counterpart using a conventional focused emission and axial profiles of the two images to establish Full-Width at Half-Max (FWHM) sizes of the vein. 107

CHAPTER 1

INTRODUCTION

Ultrasound waves have a frequency higher than 20 kHz. Ultrasound medical imaging is typically performed using frequencies between 1 to 10 MHz. The generation of an ultrasound image is based on the time it takes for the ultrasonic wave to propagate from the transducer to a target (forward propagation) and the time for the resulting echo to return to the probe (backward propagation). Image reconstruction, or beamforming, generally relies on assumptions of uniformity of the wave speed, with a value of 1540 m/s typically assumed for tissue, uniformity of attenuation, and absence of multiple scattering. Even though we know the soft and hard tissue of the human body can deviate significantly from assumptions of uniformity, modern ultrasound scanners can produce high quality images in a broad range of organs and locations.

However, there are still locations cases where the image quality is degraded or imaging is impossible. For example, in transcranial ultrasound and transabdominal ultrasound, image quality is compromised given the magnitude of image degrading phenomena that take place. In this work, we isolate and quantify these phenomena mainly in the context of transcranial imaging and how different imaging methods and modalities can be used to achieve higher quality images in a clinically translatable manner.

1.1 Sources of image degradation

The main sources of distortion during the propagation of the ultrasonic wave can be divided into two broad categories, stemming from the heterogeneous composition of the medium of propagation which can distort the phase and amplitude of the wave (aberration), and the presence of layers of different physical properties within the medium that can generate multiple reflections (reverberation). Reverberation can be further categorized as multiply-reflected sound that returns towards the transducer, causing a hazing overlay on the image, and multiply-reflected sound that is transmitted beyond the layered media that contributes to a lengthening of the transmit pulse, hereby referred to as trailing clutter. These effects degrade the image

resolution and contrast. The two main effects, aberration and reverberation, will be discussed in detail separately in the following sections.

1.1.1 Phase aberration

The local wave speed of ultrasonic propagation is unknown in medical ultrasound imaging but generally in biological soft tissues average values ranges between 1400-1700 m/s. An ultrasound scanner typically assumes homogeneous value of 1540 m/s during image reconstruction. This value can be adjusted depending on the image conditions. However, even in a weakly heterogeneous medium, small variation in speed leads to phase aberration, which then leads to sub-optimal image reconstruction. Some tabulated values for sound speed, density and attenuation constant for tissues and liquids commonly found in the human body are summarized in table 1.1.

Table 1.1: Properties of various biological tissues and liquids [1, 62]

Tissue type	Sound speed (m/s)	Density (kg/m^3)	Attenuation (Np/m)
Blood	1578.2	1050	2.3676
Water	1482.3	994	0.025
Brain	1546.3	1046	6.8032
Fat	1440.2	911	4.3578
Muscle	1588.4	1090	7.1088
Bone (cortical)	3514.9	1908	54.553
Bone (cancellous)	2117.5	1178	47

The degradation in image quality become more severe with increasing medium heterogeneity. The region possessing significant variations in speed or attenuation properties is called an aberrator. An aberrator can be a layer of different properties (fat, skull bone) or a circumscribed area (inclusion, cyst, calcification). Aberrating tissue types commonly encountered in medical imaging include fat, muscle, connective tissue, and bone. Fat is at one end of the impedance range since it has a low wave speed and a low mass density and bone, which has a high wave speed and a high mass density is at the other end. Average values for the two are shown in table 1.1, however, and especially in the case of bone, its final acoustic properties are highly dependent on its morphology, especially its porosity and micro-structure.

Phase aberration is often characterized by measuring the amplitude of the arrival time fluctuations and the spatial variation of wavefront distortion along the array aperture [186, 178, 92]. The amplitude of these fluctuations is measured with the root-mean-square (RMS) value which characterizes the strength of the phase aberration. This definition is also used in this work. The arrival time profiles for an aberrated pulse as well as

a reference pulse in a homogeneous medium are calculated by cross-correlation between the radiofrequency waveforms from adjacent elements using the following equation:

$$\rho_n = \frac{\sum_{j=1}^{k}(X_j - Xavg)(Y_j + n - Yavg)}{[\sum_{j=1}^{k}(X_j - Xavg)^2 \sum_{j=1}^{k}(Y_j + n - Yavg)^2]^{\frac{1}{2}}} \tag{1.1}$$

Where ρ_n is the calculated correlation coefficient between column k of data received at element X and the corresponding column of adjacent element Y displaced by n samples, with the mean value of X and Y being X_avg and Y_avg respectively. Once the arrival time profiles are calculated for the aberrated case and the homogeneous case for the same array and emission the root mean square difference of the two multiplied by the sampling period will yield a temporal measure of aberration, typically reported in ns.

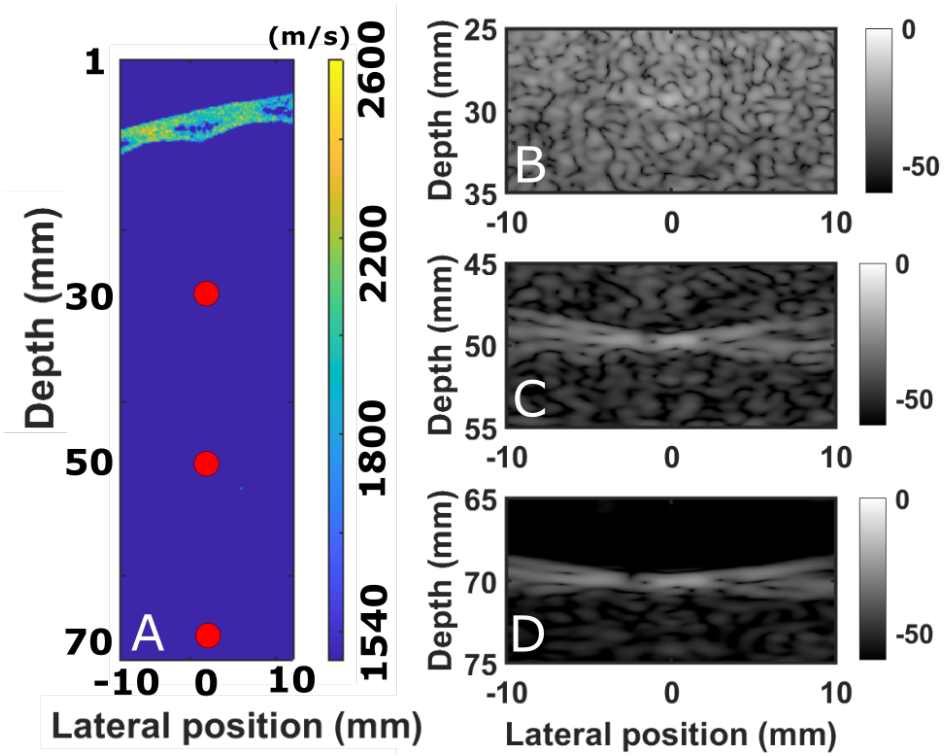

Figure 1.1: A, illustration of sound speed maps for imaging point targets through the human skull at three different depths, namely: B, at 3 cm, C, at 5 cm and D, at 7 cm. No aberration correction has been applied. Gray scale units are in normalized dB.

1.1.2 Multiple reverberations

Especially in transcranial imaging, the role of phase aberration is a well known and extensively characterized as a source of image degradation. Reverberation has not been studied to the same extent but, we

hypothesize that it also significantly degrades image quality, by reducing the target amplitude and compromising spatial resolution. Reverberation effects are more pronounced at shallower depths, but their contribution persists at depth albeit at a smaller level. The role of reverberation in image quality will be characterized and quantified in the following chapters, specifically in the context of abdominal imaging in chapter 2 and in brain imaging in chapter 3. The role of reverberation in artefact generation will also be examined in chapter 4.

Tissue harmonic imaging (THI), also known as native harmonic imaging leverages the generation of harmonic waves from nonlinear distortion as the ultrasound beam insonates body tissues during the transmit phase of the pulse echo cycle. As the ultrasonic pulse travels through tissue, it gets altered with time due to the fact that the waveform peaks move faster than the troughs because of the propagation speed difference between the compressed regions of tissue and the expanded areas. The degree of this signal distortion in tissue depends on the amplitude of the emitted pulse and the distance of propagation [113, 202]. THI can aid in the decrease of reverberation clutter in imaging because of its low amplitude in the near field where most of the reverberations occur [192]). Trailing clutter can also potentially be reduced, since it is generated in the near field, because of its low amplitude which makes it less prone to nonlinear distortion compared to the main pulse. Most of the energy in the pulse tail will remain in the fundamental frequency with propagation and will not appear in the harmonic image [152]). Harmonic imaging and its effect on transcranial image quality will be a topic in chapter 3.

1.2 Simulating sound propagation in the human body

Simulations of ultrasound imaging in the body are an invaluable tool since they can be used for beamforming and image quality optimization, transducer design and other applications, especially where rapid design iterations are required or where experiments are impossible. Experiments are often limited by clinical constraints, the availability of tissues, material types, medium characterization, or hardware, and furthermore experimental design constraints are sometimes limited by physics, e.g. where the pressure field at depth inside the body needs to be measured. Transition to clinical applications can also be facilitated by increasing the translatability of acoustical design and reducing the need for validation and patient recruitment.

Throughout this work, Fullwave [151] and Fullwave2 [143] acoustic simulation tools were used to accurately model non-linear sound propagation through a variety of acoustical environments, namely the human abdomen, the human skull and the lung-tissue interface. Fullwave is a finite difference based numerical

solver employing a high-order grid stencil that has been extensively tested in various implementations in previous work [129, 147, 144, 153]. In its latest adaptation, Fullwave2 solver models the nonlinear wave equation with multiple relaxations and relaxing perfectly matched layers for high-order numerical finite-difference solutions.

More specifically, for a nonlinear fluid that is homogeneous, isotropic, and lossless, the propagation of acoustic waves in this may be described by the set of first-order acoustic equations [68]:

$$\nabla \mathbf{p} + \rho \mathbf{D_t} \mathbf{v} = f \tag{1.2}$$

$$\nabla \cdot \mathbf{v} + \kappa \mathbf{D_t} \mathbf{p} = q \tag{1.3}$$

where p is the acoustic pressure, v is the particle velocity, f and q are the volume densities of force and injection rate, the density of mass is ρ, the compressibility is κ and lastly $D_t = \partial_t + v \cdot \nabla$. The non-linear effect caused by the second term in D_t and the equation of state for the medium is accounted for by taking:

$$\rho = \rho_0[1 + \kappa_0 p] \tag{1.4}$$

$$\kappa = \kappa_0[1 + \kappa_0(1 - 2\beta)p] \tag{1.5}$$

where ρ_0 is the ambient density of mass, κ_0 is the ambient compressibility, and $\beta = 1 + B/2A$ the coefficient of non-linearity. Setting volume densities f and q as zero and neglecting third order products of p and v and the locally nonlinear terms given by $v \cdot \nabla v$ and $v \cdot \nabla p$ Eqs. (1.2)- (1.3) become:

$$\nabla \mathbf{p} + \rho[\mathbf{1} + \kappa_\mathbf{0}\mathbf{p}]\frac{\partial \mathbf{v}}{\partial \mathbf{t}} = \mathbf{0} \tag{1.6}$$

$$\nabla \mathbf{v} + \kappa[\mathbf{1} + \kappa_\mathbf{0}(\mathbf{1} - \mathbf{2}\beta)\mathbf{p}]\frac{\partial \mathbf{p}}{\partial \mathbf{t}} = \mathbf{0} \tag{1.7}$$

Removing all non-linear terms, this final system of equations reduces to the lossless Westervelt equation. Equations (1.2) - (1.7) do not include attenuation. In order to include relaxation terms into the first order

system (1.6)-(1.7) a complex coordinate transformation of the spatial derivatives denoted by $\vec{\nabla}_1$ and $\vec{\nabla}_2$ is introduced as follows:

$$\vec{\nabla}_1 p + \rho \frac{\partial \vec{v}}{\partial t} = 0 \tag{1.8}$$

$$\vec{\nabla}_2 \cdot \vec{v} + \kappa \frac{\partial p}{\partial t} = 0 \tag{1.9}$$

For $\vec{\nabla}_1$ the above can be written as a scaling of the partial derivative and a sum on convolutions with N relaxation functions:

$$\frac{\partial}{\partial \tilde{x_1}} = \frac{1}{\kappa_{x_1}} \frac{\partial}{\partial x} + \sum_{\nu=1}^{N} \zeta_{x_1}^{\nu}(t) * \frac{\partial}{\partial x} \tag{1.10}$$

$$\frac{\partial}{\partial \tilde{y_1}} = \frac{1}{\kappa_{y_1}} \frac{\partial}{\partial y} + \sum_{\nu=1}^{N} \zeta_{y_1}^{\nu}(t) * \frac{\partial}{\partial y} \tag{1.11}$$

$$\frac{\partial}{\partial \tilde{z_1}} = \frac{1}{\kappa_{z_1}} \frac{\partial}{\partial z} + \sum_{\nu=1}^{N} \zeta_{z_1}^{\nu}(t) * \frac{\partial}{\partial z} \tag{1.12}$$

with convolution kernels in equations (1.10),(1.11) and (1.12) (ν index) being respectively:

$$\zeta_{x_1}^{\nu}(t) = -\frac{d_{x_1}^{\nu}}{\kappa_{x_1}^2} e^{-(d_{x_1}^{\nu}/\kappa_{x_1} + \alpha_{x_1}^{\nu})t} H(t) \tag{1.13}$$

$$\zeta_{y_1}^{\nu}(t) = -\frac{d_{y_1}^{\nu}}{\kappa_{y_1}^2} e^{-(d_{y_1}^{\nu}/\kappa_{y_1} + \alpha_{y_1}^{\nu})t} H(t) \tag{1.14}$$

$$\zeta_{z_1}^{\nu}(t) = -\frac{d_{z_1}^{\nu}}{\kappa_{z_1}^2} e^{-(d_{z_1}^{\nu}/\kappa_{z_1} + \alpha_{z_1}^{\nu})t} H(t) \tag{1.15}$$

where $\kappa_{x_1}(\vec{x})$, $\kappa_{y_1}(\vec{x})$, $\kappa_{z_1}(\vec{x})$, represent a linear scaling of the derivative that is outside of the convolution, $d_{x_1}^{\nu}(\vec{x})$, $d_{y_1}^{\nu}(\vec{x})$, and $d_{z_1}^{\nu}(\vec{x})$ represent a scaling-dependent damping profile and $\alpha_{x_1}^{\nu}(\vec{x})$, $\alpha_{y_1}^{\nu}(\vec{x})$, $\alpha_{z_1}^{\nu}(\vec{x})$, represent a scaling-independent damping profile. Here $H(t)$ is the Heaviside or unit step function. The full numerical adaptation and implementation of the solver is described in recent work [148].

Acoustic wave propagation in ultrasound imaging involves several physical phenomena such as diffraction, reflection, scattering, frequency dependent attenuation and non-linearity. Although models and simulation tools that simplify the propagation physics, such as convolutional models or angular spectrum approaches, offer significant benefits in terms of computational speed, it comes at a cost of reduced physical realism [74, 117]. In the studies performed in this work, however, more complex phenomena such as

scattering and attenuation become increasingly important to the accuracy of imaging in clinically challenging environments such as the human brain and abdominal area and less assumptions can be used. In the simplest case scenario we would like to be able to generate an image based on the physics of an acoustic wave propagating to a target, reflecting, and then propagating back to the transducer. Furthermore, assumptions of linearity are not always an accurate predictor of diagnostic ultrasound since the wave distorts as it propagates creating harmonics and even acoustic shocks. In many clinical applications large amplitudes and propagation lengths are used, rendering linear approximations unsuitable. Applications such as focused ultrasound therapy, radiation force, and lithotripsy depend on the non-linear deposition of peak energies. Tissue harmonic imaging (THI) is also an invaluable clinical imaging tool that improves axial resolution and reduces clutter signal caused by reverberation in various applications such as echocardiography and transcranial imaging [156, 175].

It is also worth mentioning that even though these acoustic propagation solvers have been validated in previous work, as mentioned above, in this work extensive calibration was performed on a case by case basis. To accurately calibrate each implementation a combination of experiments and simulations are matched using different metrics such as aberration values, reverberation strength, coherence curves and speckle brightness values. Calibration is always performed at the same frequency for both counterparts and the same imaging sequence method is used. For the experiments, $ex\ vivo$ biological tissues and bone specimens are used to acquire a set of realistic measurements. For the simulations, optical or computed tomography datasets of the same body portion are processed and converted to sound speed, density, attenuation and non-linearity input maps. Even though tabulated values are used as a calibration guide to assign initial values to the maps, the final simulation map values are tailored to match the experimental results. Tissue is separately calibrated for each frequency and transducer modeled using average speckle brightness as a metric.

1.3 Transcranial ultrasound imaging

Transcranial imaging has been a persistent challenge for ultrasound, especially in terms of spatial resolution, which is limited to the range of 1 mm [120]. The challenges of transcranial imaging are mainly a result of the aberration, reverberation and attenuation effects of the human skull. Ultrasound has been successfully used in therapy for decades, [124, 70], however, transcranial imaging requires a two-way wave propagation, which renders it more challenging than the one-way emissions used in therapy. Transcranial

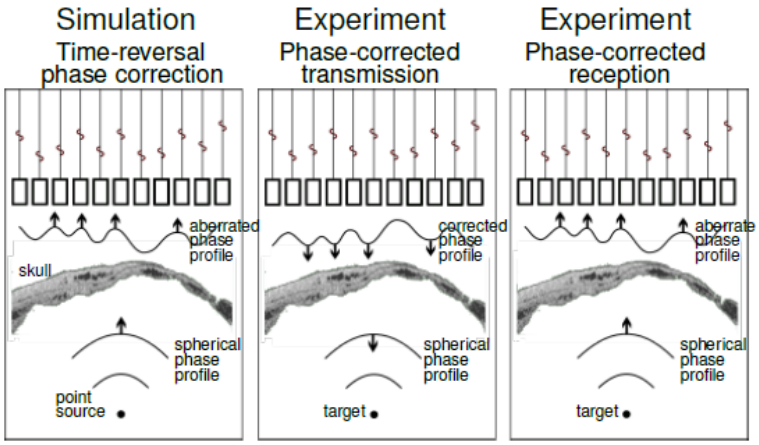

Figure 1.2: Phase aberration correction using simulations and experimental methods based on time reversal.

Doppler imaging has been extensively used to observe and monitor brain vascular blood flow, however, the method is limited by the diffraction limit in resolution, especially at the lower frequencies used to penetrate the skull more efficiently [77].

The degrading effects of aberration and multiple reverberations on a B-mode image are practically impossible to fully isolate experimentally, let alone clinically. We aim to develop simulation tools that can describe and quantify the degrading mechanisms governing transcranial imaging in the context of brain imaging. The role of multiple reverberations needs to be particularly addressed, since in literature most efforts have been focused towards aberration correction [179, 72]. A method of phase aberration correction based on time reversal is illustrated in Fig. 1.2, where a wave is emitted from a point source though an aberrator, recorded by the transducer and time reversed back towards the direction of the original target. This method is highly effective in correcting for aberration $in\ silico$ as well as in $ex\ vivo$ experiments, and actually used in chapter 6, however its clinical implementation is not possible.

1.4 Super-resolution imaging

Super-resolution imaging in ultrasound, also known as ultrasound localization microscopy (ULM), allows the ability to super-resolve vasculature well beyond the diffraction limit ($\lambda/2$) [26, 41]. Super-resolved images can be generated by accumulating the positions of the source centers in hundreds or thousands of images. For ultrasound, gas-filled encapsulated micro-bubbles act as contrast agents with a mean diameter in the order of 1-5 μm. The micro-bubbles, which are injected in the bloodstream, flow within the circulatory system, where they appear and disappear from the imaging region, enabling the sub-resolution localization of

the center of each individual micro-bubble. In order to super-localize bubble appearances they must be able to be spatio-temporally separated. Spatio-temporal separation is highly dependent on the concentration of microbubbles in the bloodstream which has to be sufficiently low to allow for independent stochastic bubble appearances in the B-mode images in slow time.

In terms of high resolution brain imaging, the imaging modalities used include computed tomography (CT) and magnetic resonance imaging (MRI) methods, whereas ultrasound has had more limited clinical applications [120]. The gold standard imaging methods used clinically, Computed tomography angiography (CTA) and Magnetic resonance angiography (MRA) have been reported to successfully detect vessels in the order of 300-400 μm [190, 63]. The advent of super-resolution imaging and the use of microbubble contrast agents allows ultrasound imaging to attain spatial resolution far beyond the diffraction limit [26]. Transcranial super-resolution imaging can improve resolution to the range of 100-200 μm [120, 173], and has the potential to map the human brain vasculature with unprecedented resolution.

ULM in the brain, can shed light on brain vascular systems in various disease processes, such as cancer, diabetes, vascular dementia, Alzheimer or Parkinson disease [20], since the high complexity of the human brain requires techniques that provide a more detailed view than conventional ultrasound imaging. Since transcranial ultrasound is generally performed at lower (¡2 MHz) frequencies, super-resolution imaging can provide us with adequate resolution to observe small vessels (0.3 mm) that we normally would not be able to properly localize that might provide crucial information in diagnosis and disease monitoring. This potential improvement of brain vasculature resolution in the clinical setting can be crucial to the assessment of these pathologies that surpass the traditional transcranial ultrasound resolution limit, such as smaller aneurysms. The high temporal resolution of ultrasound, with a framerate in the order of 6000 images/s, may also provide blood flow velocity measurements.

In this work, proof-of-concept transcranial super-resolution experiments were performed and the application of phase aberration correction and its impact in bubble detectability was explored. It was found that the resolution of a microtube target improved by at least a factor of 10 compared to conventional B-mode ultrasound. Compared to the current standard for super-resolution imaging, which uses plane waves that cannot adequately penetrate and image targets through the human skull, targeted and efficient deposition of energy through focusing combined with super-resolution, can resolve structures beyond the diffraction limit. Furthermore we propose phase corrections to compensate for aberration. These corrections can be derived

experimentally, as well as through the use of simulation tools, to further improve image quality and accuracy. The results and process are described in chapter 6.

CHAPTER 2

DECONSTRUCTION AND RECONSTRUCTION OF DEGRADING EFFECTS IN ULTRASOUND IMAGING: ABERRATION, MULTIPLE REVERBERATION, AND TRAILING CLUTTER

Ultrasound image degradation in the human body is characterized by complex propagation and reflection physics. Its heterogeneous nature, comprising different tissue types with varying sound speed, density, and attenuation, distort the ultrasonic beam causing deterioration in image quality, loss of resolution and contrast. Here, we establish a simulation based framework that deconstructs the sources of image degradation into a separable parameter space that includes phase aberration from speed variation, multiple reverberations, and trailing reverberation. This builds on previous work where the image degradation mechanisms were determined $in\ silico$. It is shown here that these mechanisms are separable and can be used reconstruct images with known and independently modulable amounts of degradation using methods that depend on the additive or multiplicative nature of the degradation. Experimental measurements and Fullwave simulations in the human abdomen demonstrate this calibrated process in abdominal imaging by matching relevant imaging metrics such as phase aberration, reverberation strength, speckle brightness and coherence length. This general framework was tested for values in acoustical ranges that significantly synthetically and independently enhance or reduce the effects of aberration, multiple reverberation, or trailing clutter compared to levels naturally occurring in the body. Identifying, quantifying, and modeling these complex mechanisms of degradation are a critical component to develop rational strategies that can improve image quality.

2.1 Introduction

The heterogeneous acoustical properties of different tissue types, namely sound speed, density, and attenuation, distort and reflect the wavefront as it travels to the target and as the echoes travel back to the transducer. In human abdominal imaging, for example, multiple layers of connective tissue and fat generate reverberation clutter and aberrate the beam to the point where diagnostic imaging becomes difficult or impossible for some, with additional MR imaging required for the diagnosis of certain conditions [13]. These

factors usually occur in overweight and obese individuals, typically a BMI higher than 30, who have thicker layers of subcutaneous fat as well as more fascial or connective tissue layers that supports this additional fat [15].

Aberration occurs due to the inhomogeneity of the speed of sound in tissue which deviates from the constant value used in ultrasound beamforming (typically 1540 m/s) and distorts the ultrasound wave. The wave front distortion decreases image resolution and introduces noise that obscures the target of interest. There has been a broad research interest aimed at mitigating or correcting aberration and a wide variety of techniques have been proposed to compensate for aberration as well as speed of sound deviations. Near-field correction techniques, for example, assume that the distortion can be approximated by a thin phase screen at or near the transducer surface [53, 54, 115]. However, even though this class of phase aberration correction techniques is relatively simple to implement, in many cases it results in limited improvements in image quality [185, 160, 30]. Distributed aberration models and correction techniques have been developed based on the more physically realistic assumption that aberration occurs deep within soft tissue [52, 91, 181]. Distributed aberration correction is typically more complex in terms of estimation and implementation. Some implementations, for example, require the presence of point reflectors within the body, which are not commonly found in tissue. Acoustic refraction, a component of aberration, leads to geometric distortions if not accounted for. Jaeger $et\ al$ [106], showed that for moderate speed-of-sound variations, refraction can be mathematically described within the concept of straight ray propagation, and is mainly manifested in the receive delays during beamforming, with aberrations having an insignificant effect on the lateral position of echoes. More recently, real-time correction methods to correct for the wavefront distortion due to refraction have been explored in 3D [89], however assuming a constant aberrator thickness. Others developed this method for layered aberrators using realistic assumptions of direction and thickness for the aberrator to accurately model refraction in intraosseous ultrasound [159]. Accurate speed of sound measurements are also a crucial part of breast cancer ultrasound tomography applications, where the density of breast tissue is measured as a biomarker [201]. Variations of this technique to a more clinically accessible environment involving approaches targeting speed of sound reconstruction have also recently been explored [163].

Reverberations occur when an acoustic wave is reflected multiple times and it typically appears as clutter that is overlaid on the underlying tissue image thus resulting in significant degradation of image quality. Its effects on image quality are broad and can be characterized by loss in resolution and contrast. Reverberation clutter arises from multiple reverberation between layers of tissue with different properties,

scattering from off-axis targets or side and grating lobes, and aberrations. Reverberation and aberration are the main degrading mechanisms responsible for poor image quality, however reverberation correction has been less investigated, perhaps due to the inherent difficulty of correcting multiple scattering events [29]. Tissue harmonic imaging is perhaps the most widely used method that has been shown to improve image quality in the presence of clutter and it is used extensively in ultrasound imaging [**?** 29]. Imaging methods based on the short-lag spatial coherence (SLSC) of backscattered echoes have been proposed to reduce background clutter and increase signal to noise ratio [79]. Applications of this method as well as its harmonic counterpart have been shown in $in\ vivo$ fetal imaging where the contrast to noise ratio doubled for the latter [75]. Other post-processing approaches to reduce reverberation and off-axis clutter include algorithms such as the aperture domain model image reconstruction (ADMIRE) beamforming, validated in $in\ vivo$ fundamental and harmonic imaging scenarios [32].

Inter-layer reflections that are transmitted in the direction of pulse propagation instead of returning to the transducer surface, add a long, low-amplitude tail to the pulse causing it to appear lengthened, resulting in additional clutter further away from the transducer and compromising resolution [29]. This phenomenon is known as trailing clutter and is often included in total reverberation clutter. In previous work, the role of phase aberration and reverberation as two major mechanisms in the degradation of ultrasound image quality were analyzed [134]. It was also hypothesized that reverberation clutter from subcutaneous tissue layers limited the effectiveness of phase aberration correction techniques by corrupting the RF channel signals. [133, 134, 136].

The generation of an ultrasound image of the soft tissue in the body relies on the physics of acoustic wave propagation in heterogeneous media which includes the effects of diffraction, reflection, scattering, frequency dependent attenuation and non linearity. Simulation tools are an invaluable tool in characterizing and quantifying the relationship between wave propagation, human anatomy, and the resulting ultrasound image. A direct simulation of the propagation to a target, reflection, and then propagation back to the transducer is computationally costly due to two fundamental physical scales: i) the propagation distance(100λ) and ii) sub-resolution scatterers ($< \lambda/10$). To represent both length scales in 3D, simulation fields with large number of points in space (10^9) are required. Furthermore, numerical methods are challenged by the extremely high dynamic range because the backscattered wave may be 100 dB smaller than the transmitted pulse. Therefore any numerical errors from the large amplitude forward propagating wave must be 100 dB smaller than the backscattered wave. Given these challenges, it is unsurprising that simulations of ultrasound images make approximations that remove the need to model propagation directly. The most widely used simulation tool,

Field II, for example, relies on the spatial impulse response and Hankel functions to replace propagation with a convolution approach [73]. However, by not simulating wave propagation directly, effects such as multiple scattering, reverberation, distributed aberration, and non linearity, which can be determining factors of ultrasound image quality, cannot be modeled. There are a number of simulation tools that model nonlinear propagation [22, 157, 28] and they have been used successfully in modeling therapeutic acoustic fields. However they cannot model multiple reflections and backpropagation, which are necessary for imaging. Ultrasonic propagation through fine scale heterogeneities has been simulated previously with a finite difference time domain (FDTD) solution of the 2D and 3D linear wave equation [100, 99], but they use low order stencils that generate forward propagation errors that are large compared to the backscattered wave. Other simulation tools also exist that can model nonlinear ultrasound propagation based on spectral domain or k-space methods [189]. These numerical tools can model the fundamental wave physics of backpropagation, non linearity, and attenuation. However, since the Fourier transform of spatially localized structures has broad support in the Fourier domain, spectral methods do not accurately model the low amplitude reflections from sub-resolution scatterers or small structures, that are a key component of ultrasound images.

Identifying, quantifying, and modeling these complex mechanisms of degradation are a critical component to develop rational strategies that can improve image quality. The mechanisms of multiple reverberations and phase aberration in the abdomen have been described in previous work using Fullwave simulations [133, 134, 136]. Since its first publication [150], Fullwave has been updated and into a higher-order version, Fullwave2 [148]. In this work we introduce an experimentally calibrated platform that allows for the isolation of each component of degradation, and its subsequent removal or addition from or into a B-mode image. Trailing reverberations are also characterized in depth. This general framework was calibrated to soft tissue measurements for specific transducers and imaging sequences for human abdominal to characterize the depth and target brightness dependence for these different reverberating and aberrating environments. We show that using this calibrated simulation method we can span the parameter space of image degradation in an independent or orthogonal fashion. This enables the generation of realistic and propagation physics-based image degradation that includes and exceeds ranges that would be encountered clinically in transabdominal or transcranial imaging. Such flexibility offers advantages in the generation of training databases for machine learning applications as well as the development of beamforming strategies for challenging imaging scenarios.

2.2 Methods

A C5-2v abdominal imaging transducer was connected to a Vantage 256 ultrasound research scanner (Verasonics, Inc., Kirkland, WA) to capture RF channel signals for all experiments in this work. The same median frequency of 3.7 MHz and a 2 cycle focused wave emission is used in both experiment and simulations.

A porcine abdominal phantom was used to obtain measurements required to measure characteristics of the wave propagation physics, namely aberration values, reverberation curves, speckle brightness and coherence curves, and then appropriately calibrate the acoustical maps in the simulation tool. These four calibration processes are described in detail in the following subsections 2.2.3,2.2.4,2.2.5 and 2.2.6. Subsection 6.2.4 focuses on the generation of the input maps to the simulation tool.

2.2.1 Sources of degradation

The effects of aberration on a point target are illustrated in Fig. 2.1B. Since phase aberration is dependent on the acoustical properties of the aberrator, once the wave has propagated through the aberrating volume, the phase distortion remains relatively unchanged with imaging depth. Furthermore the image degradation arising from aberration is independent of target brightness.

The effect of reverberation on the image is schematically shown in Fig. 2.1C where the overall blurring of the image is evident. Multiple reverberation clutter is largest close to the degrading source and its effect attenuates with increasing depth. The degradation arising from reverberation is more severe for dim targets than for bright targets.

The last component of degradation examined in this work is trailing clutter, also illustrated in Fig. 2.1C, directly following the target. Trailing clutter is hypothesized to be independent of imaging depth.

2.2.2 Simulations

In previous work, we have used and characterized a 3-D heterogeneous tissue model of a human abdominal layer [140, 148]. The discrete structures in the model are assigned one of three tissue types: fat, muscle, or connective tissue and each type is given tabulated values for speed of sound, density, non-linearity, and attenuation [62]. Pixel sized scatterers are also introduced into the entirety of the abdominal wall portion to realistically simulate the scattering physics of tissue. The scatterer properties are discussed in detail in

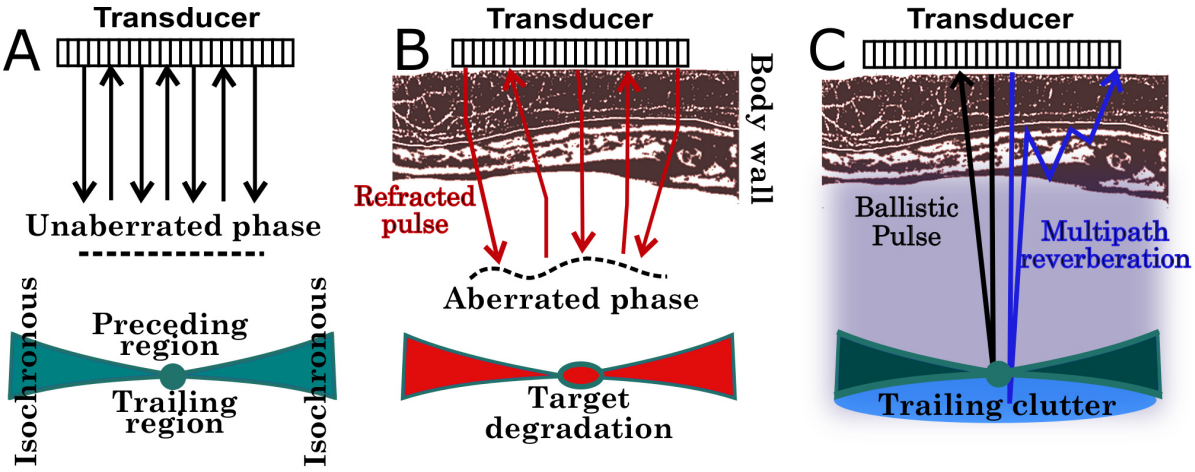

Figure 2.1: A, in a homogeneous medium, a typical PSF is characterized by three different regions, preceding, trailing and the isochronous volume. In B, aberration degrades ultrasound focusing capability and compromised resolution. In C, multipath reverberation overlays acoustical noise to the echoes produced from the ballistic pulse, thereby reducing detectability. The lengthening of the pulse results in the appearance of trailing clutter. Both reverberation and aberration depend on body wall anatomy.

2.2.5. Based on calibration measurements the tabulated values for different tissue types are subject to change since gaussian filtering is performed on the maps to ensure proper matching based on metrics described below. The final maps were filtered using a 2-D Gaussian smoothing kernel with standard deviation of 1.5. This filtering precedes and excludes any pixel sized scatterers since it would compromise their distribution. Since the C5-2v transducer modeled is curved, its geometry is accurately represented during compression, as shown is Fig. 5.2A by the yellow arc portion. The pulse is emitted from the last pixels of the arc. The optical dataset from where the abdominal maps were derived is shown in Fig. 5.2B and the actual region depicted in A is derived from the portion boxed in white.

Fig. 5.2C, shows the raw data of a focused wave propagating through the abdomen overlaid on the input sound speed map in A, and three distinct regions can be identified. Fig. 5.2D shows the wave having traveled through the abdominal wall, hence the signal is highly incoherent. As the wave propagates in the homogeneous medium region in Fig. 5.2E, coherence increases, and maximizes near the focal zone (80 mm) as shown in Fig. 5.2F. Here, all three regions that comprise the PSF can be seen, namely the preceding region, the isochronous volume and the trailing region where the pulse appears to be lengthened.

All simulations were performed on a Linux Fedora 25 (v.4.10.13-200.fc25.x86 64) system running Intel Xeon® E5-2630 v4 Processors at 2.20 GHz. The simulation code was written in C and post-processing was performed on MATLAB. Each simulation for each individual emission case has an approximate duration of 30 min. The imaging medium is described with a spatial resolution of 34.7μm.

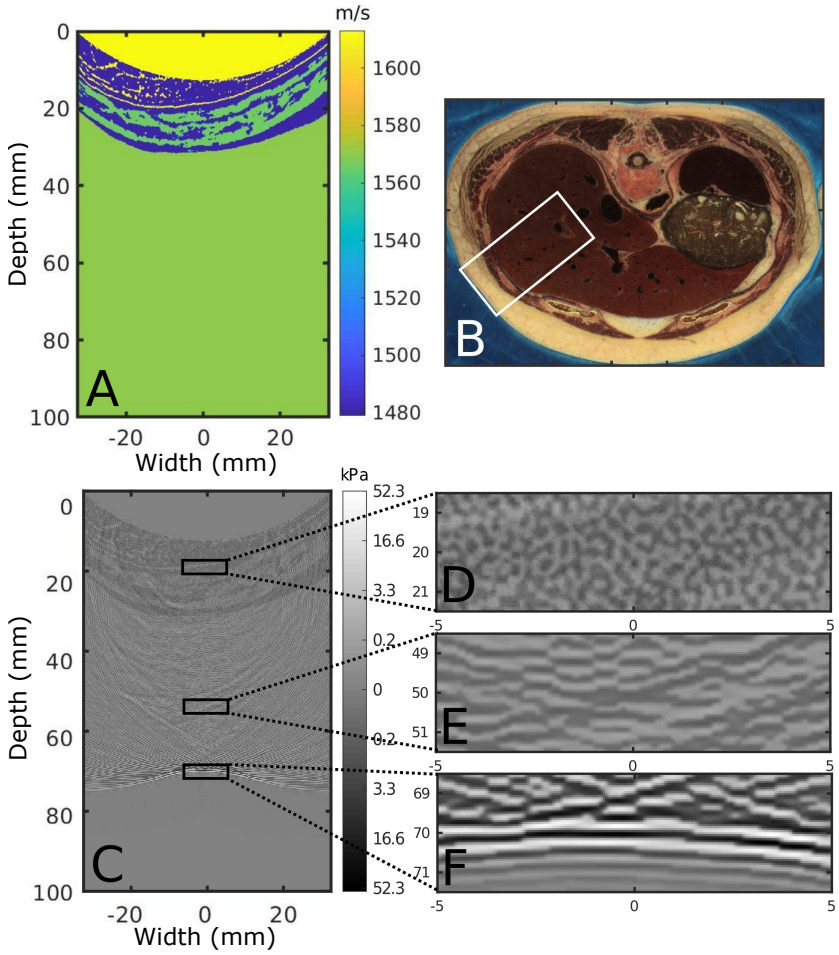

Figure 2.2: (A) Example of an input sound speed map for Fullwave2 simulations, as segmented and processed from the selected portion of (B), the visible female abdominal dataset. In (C), the result of a wave propagating through map (A) is shown. Highlighted are different characteristic regions of propagation: (D) is the highly incoherent portion of the wave as it travels through the abdominal wall. As the wave enters the preceding region in (E), coherence increases as it approaches its natural focal zone. In (F) the wave has reached its maximum coherence value at the focus.

2.2.3 Aberration RMS values

The phantom was comprised of a 20 mm thick porcine abdomen that was immersed inside a water tank kept at room temperature. This abdomen included a thin layer of hairless skin, followed by fat and muscle tissue. Connective tissue was also found throughout the abdominal layers. No liver was introduced in this experiment. The C5-2v transducer was placed directly above and in contact with the abdomen. To obtain the root mean square (RMS) value of aberration for the abdomen, a thin wire was placed perpendicular with respect to the long axis of the transducer, thus acting as a point target, and its backscattered echo through the abdomen was recorded. This was compared against the same wire target at the same depth from the

transducer in a water tank without any tissue (homogeneous medium) which served as a reference. By means of correlation the two profiles fitting the backscattered echoes of the target through the abdomen and the target in water were compared. The RMS difference of the two profiles in time served as a measure of aberration strength. The RMS value of the aberration for the experiment was calculated at 143.7 ns whereas for the simulations the RMS value was calculated at 146 ns.

2.2.4 Reverberation curves

The same phantom described above without a wire target was used to measure the reverberation strength of the abdominal wall. Liver is not included in this configuration and a homogeneous medium follows the abdomen in both simulations and experiments (water). Reverberation curves were acquired by laterally averaging the beamformed RF data and plotting them as a function of depth. The same process was followed for both experiments and simulations. In Fig. 6.3A and B, the B-modes for both experiment and simulation are shown respectively. The thickness of the abdomen is roughly the same at approximately 20 mm, with localized reverberation apparent until roughly the depth of 40 mm. The two B-modes were beamformed using a conventional delay-and-sum algorithm for a uniform beamforming speed of 1540 m/s. Note that after 20 mm there is no tissue, yet there is still signal in the B-mode images due to reverberation which persists for lengths of time that are coincident with reflections from depths greater than 20 mm. Fig. 6.3C shows the reverberation curves for both experiment and simulation cases derived from images A and B, laterally averaged and displayed as a function of depth which demonstrates an agreement between the two cases.

2.2.5 Speckle brightness

To estimate mean tissue brightness, a piece of porcine liver was inserted under the abdomen. The liver was thick enough to span a total of 6 cm in depth, including the abdomen, and long enough to cover the length of the transducer, approximately 3 cm. The liver is rather homogeneous and is used to calibrate speckle brightness in simulations for the given frequency and transducer using the average speckle brightness as a metric, calculated as the mean B-mode brightness value for the focal region. In simulations, tissue is modeled using a random distribution of pixel-sized scatterers which are characterized by a given density (number of scatterers per resolution cell) and an impedance variation expressed as a percentage of variation. Different sets of simulations were ran for different scatterer characteristics until a satisfactory match between experimental and simulation values was achieved. The final calibrated speckle brightness values matched

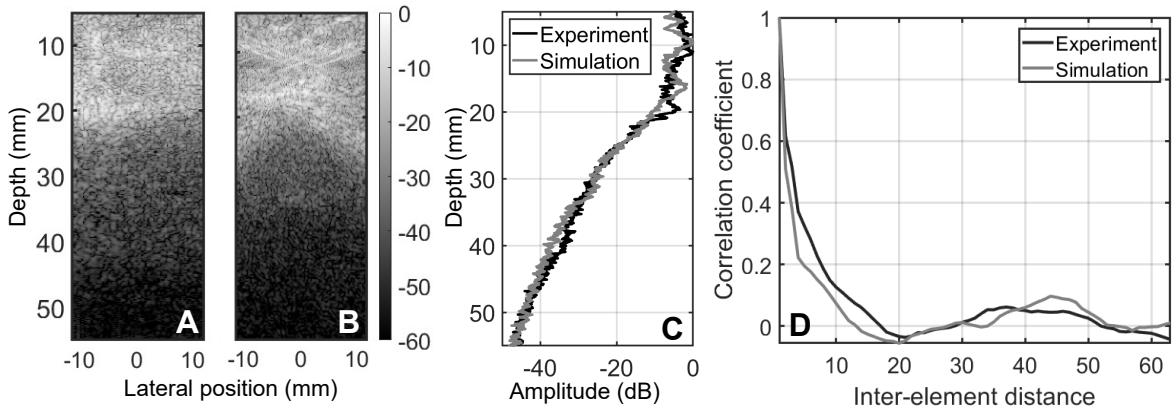

Figure 2.3: A, Experimental B-mode of pork belly immersed in water using the C5-2v probe. B, Simulated B-mode of the visible human dataset used for calibration to experimental data. B-modes are normalized with respect to the maximum of each image. Units are in dB. C, comparison of experimental and simulation reverberation curves for the first 60 mm of depth. D, coherence plots comparison for simulation and experiment at the focal depth (50 mm), in the center of the transducer laterally.

for the experiment (-43 dB) and the simulation dataset (-43.2 dB) for simulation values of a density of 18 scatterers per resolution cell with an impedance variation of 3.5%. The same scatterer distribution is used in the abdominal wall portion as well as in homogeneous tissue simulating liver, which is used later in the anechoic lesion analysis.

2.2.6 Coherence curves

Spatial coherence for the experimental and simulated data during the calibration process was measured in the same manner as in Pinton et al. (2014) [136], by means of correlation of the signals received by the transducer as a function of inter-element distance, or lag. This coherence curve is shown in Fig. 6.3D. The correlation coefficients are calculated for a single full-aperture focus at 5 cm of depth and in the lateral midline where liver tissue is present for both the experiment and simulation. Lag-one coherence (LOC), introduced by Long et al. [93], can also be used as an image quality metric and was found to be correlated to traditional image quality indicators such as CNR. LOC leverages the spatial coherence between nearest-neighbor array elements to provide a local measure of thermal and acoustic noise. LOC was measured at 0.95 for the experiment and 0.96 for the simulation.

2.2.7 Isolating components of degradation

Having established the calibration match between the real and simulated abdomen, we proceeded to show that each component of degradation can be separably characterized using simulation tools. The same simulation environment described in subsection 6.2.4 is used, and a single transmit, focused emission, focusing directly on the point target region is used, in order to achieve maximum deposition of energy. The transducer was also apodized on emission at half the aperture to eliminate border reflections due to the size and curved shape of the transducer.

In order to linearly isolate image degrading effects into their individual components, isoimpedance and isovelocity images were produced. To generate isovelocity images, the sound speed maps in the simulation were set to be constant at a reference value of 1570 m/s, while conserving the heterogeneous density, and attenuation maps. Non-linearity maps are kept at a zero value to allow for the linear separation and potential recombination of the aforementioned elements. To remove reverberations from the image, two different simulation scenarios, one without a point scatterer and its identical counterpart including the scatterer are used. Subtracting the former from the latter results in removing the effects of reverberation, whilst preserving aberration. An additional simulation scenario was explored where sound speed and attenuation maps remained identical to the heterogeneous case but density was scaled accordingly for impedance to match a constant reference value equal to the homogeneous case. In these isoimpedance images the effects of reverberation were removed but at the same time trailing clutter also reduced in the B-mode image.

2.3 Results

2.3.1 PSF analysis

The PSF can be divided into three regions: First the isochronous volume, which is the bow-tie shaped figure centered at the focus. Signals within this volume have had time to travel from any point on the transducer surface to the target and back again to any point on the transducer surface. The second region, referred to as preceding region, is situated above the isochronous volume which corresponds to values in time that precede the arrival from the isochronous volume, in this case these signals can physically only arise from multiple reverberation paths within the abdominal wall that are shorter than the isochronous paths. The third region trails the isochronous volume and corresponds to times that follow the arrival of the target

signal. This corresponds to two distinct types of signals, i.e. multiple reverberations with a path that is longer than isochronous paths or trailing distortions of the ballistic pulse which constitute the trailing clutter. This distinction is important because the amplitude of multiple reverberation is independent of target brightness whereas the reflection magnitude of trailing clutter depends on target brightness.

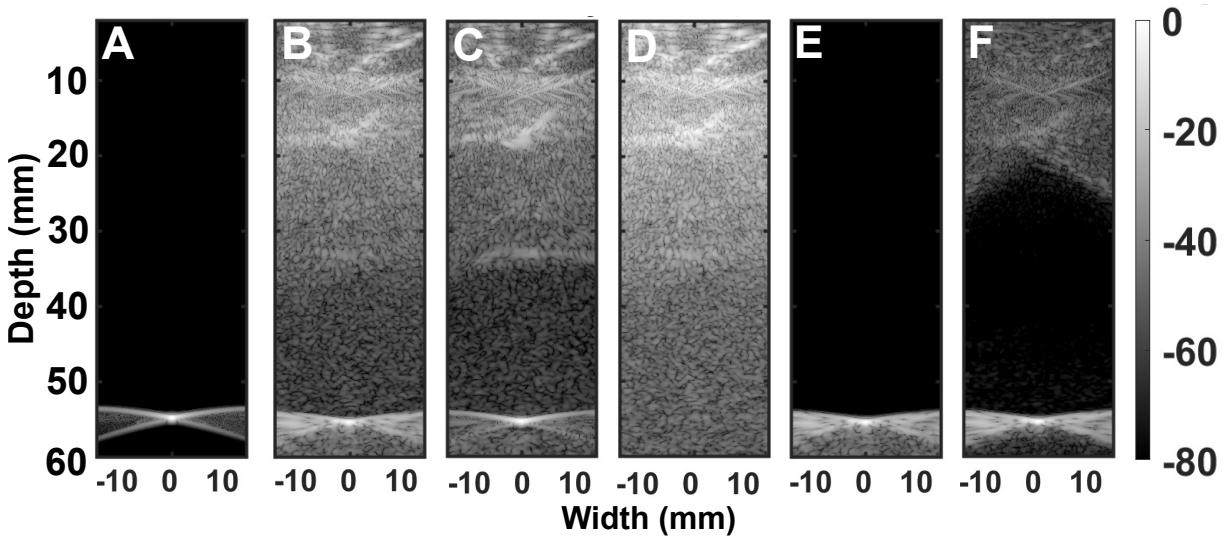

Figure 2.4: A-E, B-mode images for a target at 55 mm from the transducer normalized by the maximum amplitude of the homogeneous case. A single transmit was used with apodization on half the transducer elements. A, is the homogeneous B-mode, B is the heterogeneous B-mode through the abdomen, C is the isovelocity B-mode. D is the isoimpedance B-mode through clutter subtraction whereas E is the isoimpedance B-mode through setting the isoimpedance to be constant.

PSF simulations for these five cases are shown in Fig. 2.4. A scatterer was placed 55 mm away from the transducer in a homogeneous medium for reference, shown in Fig. 2.4A, and under an abdominal slice, cases Fig. 2.4B-D. Qualitatively, it appears that aberration appears to play a crucial role in this imaging scenario, as in the isovelocity case, Fig. 2.4C, the point target appears to be almost fully restored to its homogeneous state. Reverberation in this case appears to play a secondary role, since the target in Fig. 2.4E and F is still as degraded as in B. This is due, in part, to the fact that the point target is bright and not at a shallow depth, and therefore is less sensitive to reverberation degradation, whereas its sensitivity to aberration is independent of target brightness.

The mean amplitude of each of these three regions, preceding, trailing, and isochronous, is shown in Table 5.1. In more detail, for the preceding regions, inserting the abdomen resulted in a 31 dB increase

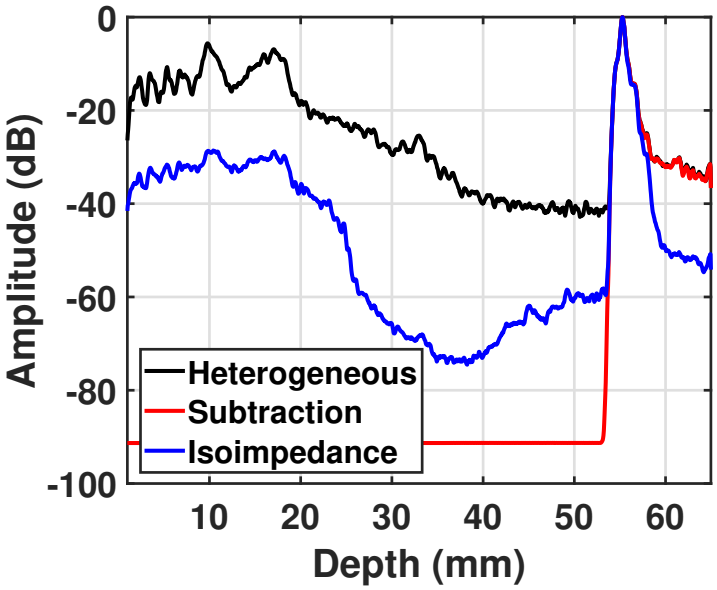

Figure 2.5: Reverberation curves for the heterogeneous, the clutter subtraction and the isoimpedance B-mode images.

compared to the reference homogeneous case, while removing phase aberration had little effect, decreasing the amplitude by an additional 3 dB. Removing reverberations via setting impedance to be globally constant restored the mean amplitude to 83.5% of its original homogeneous value and subtracting the background clutter has the greatest effect on the preceding region, bringing it to 90% of its original value in the homogeneous case. The amplitude of the isochronous regions remains constant for all reverberation manipulations, but is significantly restored when removing phase aberration, reaching 82% of its homogeneous reference value.

The addition of the abdomen in the heterogeneous case increases the trailing region amplitude by 43 dB, compared to the original value of -93 dB for the homogeneous case. The trailing region amplitude, is restored closest to its reference value for the isoimpedance case, at -68 dB. Removing multiple reverberations via subtraction of clutter as well as removing phase aberration does not significantly affect the amplitude of the trailing region as compared to the heterogeneous case, with its values remaining at -50 and -52 dB respectively. The effects of reverberation decreasing operations described above can be seen schematically in Fig. 2.5 for the isoimpedance and isoimpedance via clutter subtraction methods as compared to the heterogeneous case. As also shown in Table 5.1, for the isoimpedance via subtraction case, the mean amplitude of the image up to the depth of the target drops to the lowest level comparable to the homogeneous case but there is no difference in the amplitude of the trailing region. For the isoimpedance case, the reduction of the amplitude of the trailing region is significant. The residual appearance of reverberation within the abdominal tissue

layer in this case however, indicates imperfect cancellation of reflections with the simulation tool, likely due to small numerical errors at complementary speed/density boundaries which cause spurious reflections.

Table 2.1: Average magnitudes, relative to the main lobe, of the three regions for a scatterer at 55 mm

	Preceding	Trailing	Isochronous
Homogeneous	-91	-93	-60
Heterogeneous	-60	-50	-32
Clutter subtraction	-82	-50	-32
Isovelocity	-63	-52	49
Isoimpedance	-76	-68	-32

To elucidate the dependency of phase aberration on target depth, the same simulation setup though the human abdomen was used for targets placed at 45, 55 and 65 mm, with a single pulse focusing at the depth of each target. For the three simulation case the RMS values of aberration were found to be 143, 130 and 139 ns respectively, showing that no significant variation in aberration occurs due to different imaging depth. The effects of reverberation were removed from the RF data via clutter subtraction before performing the RMS calculations to minimize any variability not stemming from phase aberration. The B-mode images for these three cases described are shown in Fig. 2.6A-C.

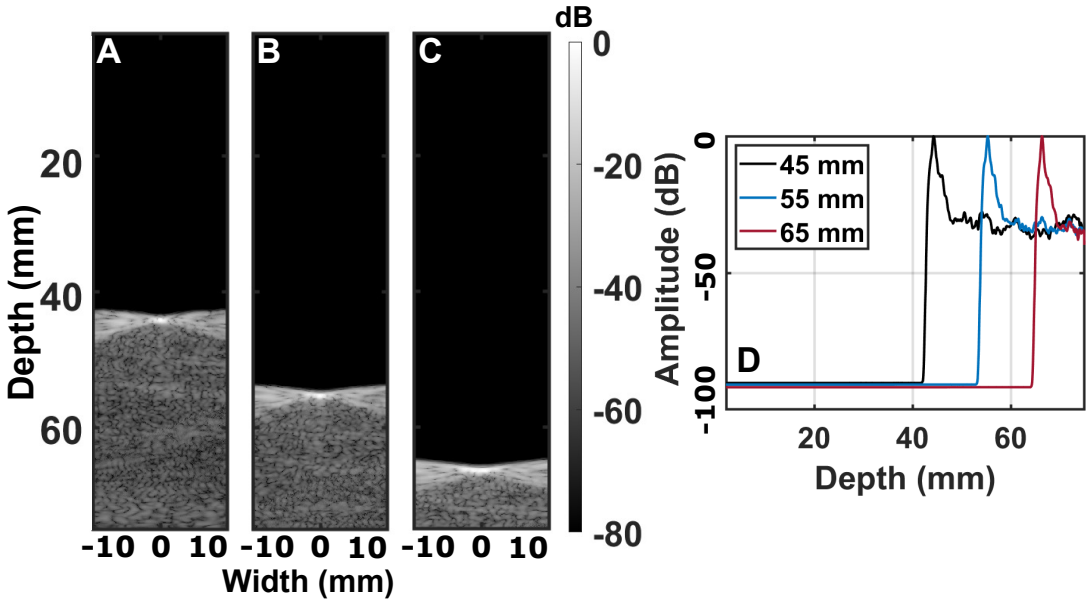

Figure 2.6: Isoimpedance via clutter subtraction B-modes for A, a target at 45 mm, B, a target at 55 mm, C, a target at 65 mm. D, Reverberation curves for B-modes A-C.

Trailing clutter is a degradation or lengthening of the transmit pulse that was hypothesized to be independent of target depth. In Fig. 2.6D the reverberation curves for the isoimpedance B-mode images

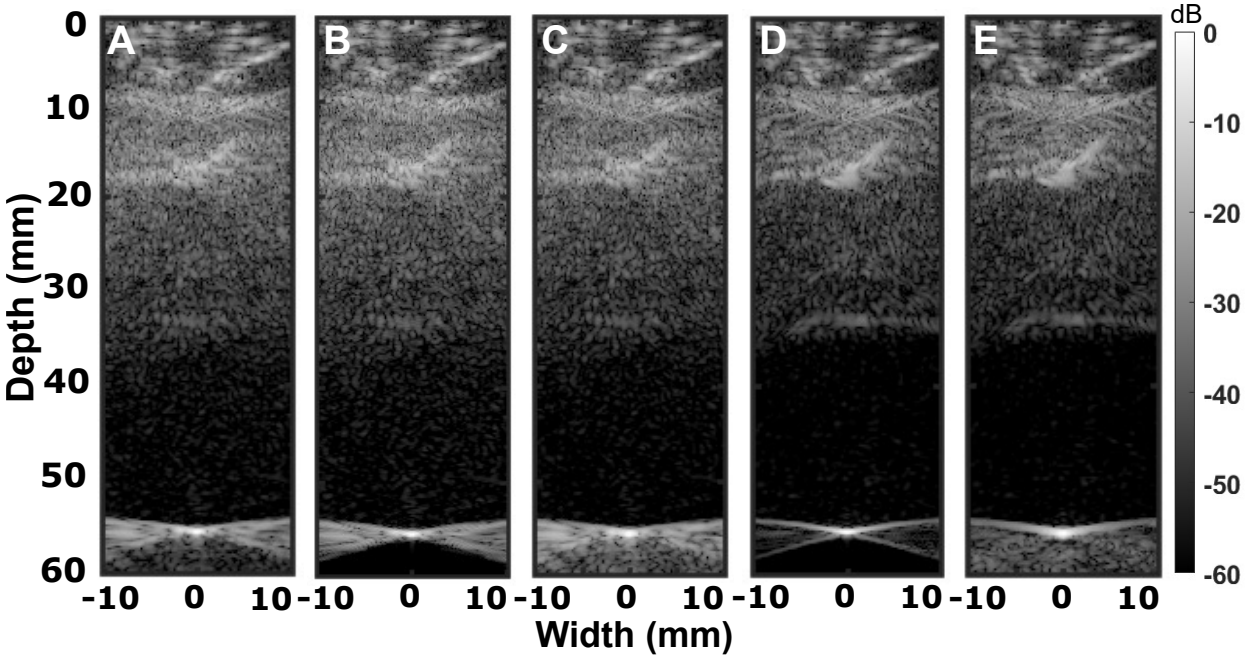

Figure 2.7: B-modes images with trailing clutter linearly subtracted in: A) Isovelocity B-mode, where the trailing clutter is isolated from via either correlation of thresholding at -20 dB in this case. B) The heterogeneous B-mode. C) The isoimpedance B-mode.

2.6A-C are shown and it can be corroborated that indeed the magnitude of the trailing clutter remains the same regardless of the depth of the target. In Fig. 2.7 it is shown that trailing clutter can be completely removed from a given B-mode since it is isolated in the area following the point target. Following its isolation, it can also be scaled and re-introduced back into the RF data of the image. Isolation is achieved by first identifying the point of the highest correlation value between the emission pulse and the target echo in the RF simulation data. The signal following these highly correlated regions correspond to the lengthened trailing pulse. Fig. 2.7A shows the same heterogeneous B-mode as in Fig. 5.5B but in a different dynamic range for comparison. In Fig. 2.7B, trailing clutter is removed from A and in Fig. 2.7C it has been increased by a factor of 2. Fig. 2.7D shows the isovelocity B-mode image with the trailing clutter removed and in Fig. 2.7E it has again been scaled by a factor of 2.

Target brightness or the impedance mismatch between the sub-resolution scatterer and the background tissue, elucidates how the difference in target reflectivity affects image degradation mechanisms, especially in terms of reverberation. In Fig. 3.9 we used targets of varying reflectivity with respect to the background in an otherwise identical simulation setup, also used in Fig. 2.4B. In Figures 3.9A-F, the target impedance

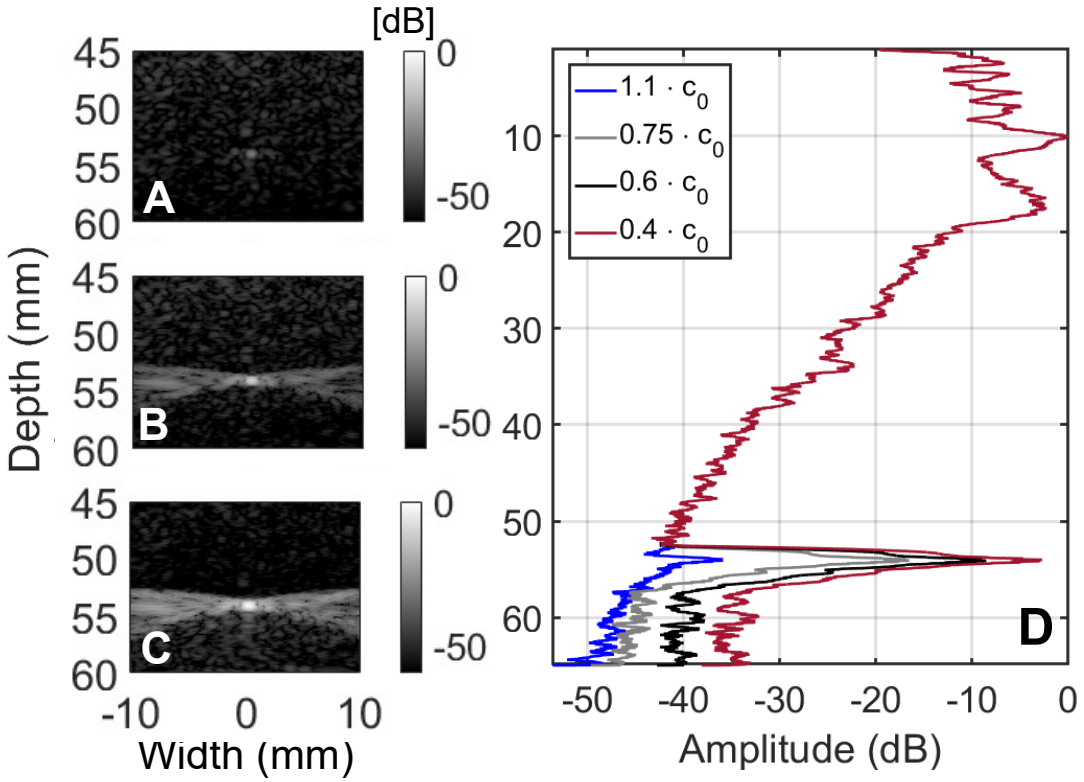

Figure 2.8: B-mode images for impedance mismatch between target and background scaled by background speed of: A, 110% B, 75% C, 40% of background speed. D, reverberation curves for different target impedance mismatch to showcase scaling of the trailing clutter.

mismatch was altered to yield reflectivity values ranging from 0.93 to 0.05. We hypothesized, based on the propagation physics, that target characteristics such as brightness, do not affect the magnitude of multiple reverberation, which depends only on the properties of reverberating structures, in this case the abdomen. This is evident in Fig. 3.9G, where reverberation curves preceding the target remain unchanged since the target reflectivity is the only variable.

In terms of overall image quality, a dim target will only be visible above the acoustical noise floor arising from reverberation, whereas a bright target will have higher contrast. This distinction is visible in Fig. 3.9A, for a very bright target, in comparison to Fig. 3.9F, for a target close to the noise floor. The impact of reverberation on image quality is thus *dependent* on target brightness. Conversely, the degradation from aberration is independent of target brightness because the phase distortion accumulated by the wave front on its path to the target is reflected by the point target. A brighter or dimmer target does not reflect more or less phase distortion. In other words the impact of phase aberration on image quality is *independent* of target brightness. Indeed the RMS value for phase aberration for a bright target (Fig. 3.9B) was 133 ns and for a dim

target (Fig. 3.9E) was 143 ns. Aberration values were measured from the isoimpedance versions of the PSFs in order to eliminate any effects of reverberation that degrade the profiles used to measure RMS differences.

Trailing clutter appears due to the pulse lengthening of the wave that does not depend on the target brightness, however its amplitude scales according to target reflectivity. Fig. 3.9G shows how targets of high reflectivity produce high amplitude trailing clutter whereas for low reflectivity targets it gradually lessens.

2.3.2 Anechoic lesion analysis

Having shown that image degradation components can be successfully isolated and characterized, it is demonstrated that selected degradation effects can be introduced in B-mode images in an orthogonal manner. For this purpose anechoic lesions were simulated with a field of random scatterers inserted in the acoustical maps with the calibrated density and impedance values described in subsection 2.2.5. This models a uniform liver. In this field, three circular anechoic lesions were introduced at depths of 40, 60 and 80 mm respectively by removing all scatterers within a radius of 5 mm. Even though PSFs accurately capture the imaging capabilities, it can be hard to understand the clinical relevance based on PSF analysis along. Anechoic lesions yield a more relevant to clinical relevant characterization of the imaging characteristics and degradation effects.

For that reason, the simulated imaging sequence was extended to model 64 focused transmit-receive events. Each event, directs the wave to a different focal location laterally in a sector scan format that follows the curvature of the C5-2v probe. The 64 individual foci, were placed at intervals of beamwidth/2, corresponding to 173 μm for the modeled transducer. One line per transmit was used for beamforming, resulting in the B-mode images shown in Figures 2.9 and 2.10.

First, a reference lesions image was established by inserting sub-resolution scatterers and the anechoic scatterer-free lesions in an otherwise homogeneous medium (Fig. 2.9A). Then, the abdominal wall is inserted, to simulate a trans-abdominal emission, hereon referred to as a heterogeneous case. Illustrated in Fig. 2.9B, the abdomen reduces both contrast and resolution in the image. The top lesion has the greatest reduction in image quality, since the effects of reverberation are more pronounced at this depth, while aberration is also present. In Fig. 2.9D, the background clutter shown in Fig. 2.9C was linearly subtracted from image B, thus removing the effects of multiple reverberations. In Fig. 2.9E, the product of sound speed and density was kept at a constant value equal to the homogeneous value to produce the isoimpedance B-mode. This was achieved by scaling the density maps appropriately. Lastly, setting the speed of sound to be constant

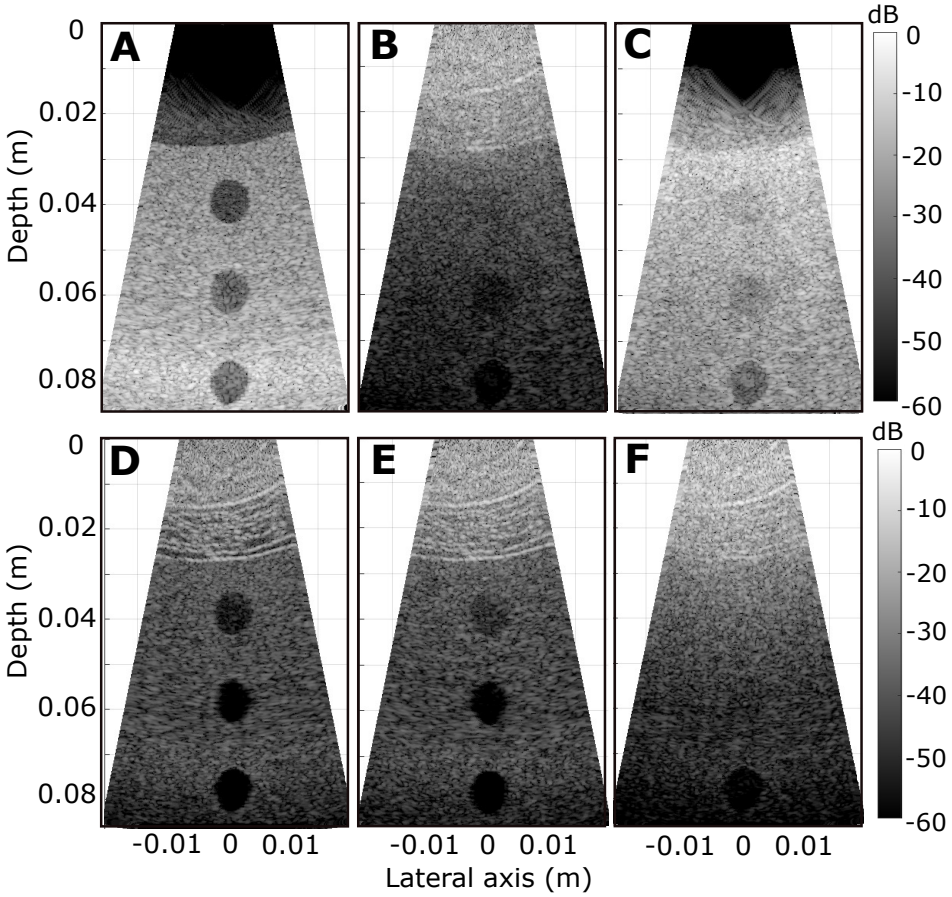

Figure 2.9: Anechoic lesions at 40, 60 and 80 mm, A for the homogeneous case, B for a transabdominal heterogeneous case, and C for an isoimpedance case where the effects of reverberation are removed. D, isovelocity B-mode where the effects of aberration are removed and density is kept at its original value. E, isovelocity B-mode where the effects of aberration are removed and density is scaled to keep impedance constant. F, isovelocity B-mode with density increased by a factor of 4. All lesions are reconstructed from 64 independent transmit-receive events focusing at the depth of the deeper lesion (80 mm) and following the curvature of the C5-2v array.

while simultaneously scaling the density maps accordingly to preserve the original impedance value for the heterogeneous case, the isovelocity B-mode was obtained, shown in Fig. 2.9F, in which the effects of phase aberration were removed, while impedance mismatch, and therefore reverberation strength were retained.

Apart from the isolation and removal of reverberation and aberration from the image, it was also shown that these effects can be separately exaggerated. The sound speed maps and density maps were modified to vary impedance mismatch between the different layers of the abdominal wall and the background tissue, which was kept at a constant speed of 1570 m/s (c_0) and a density of 1064 kg/m^3 (rho_0), values characteristic for liver tissue. For the generation of higher impedance sound speed maps the expression $c' = (c - c_0) \times \gamma + c_0$ was used, where γ is an integer signifying the increase of impedance. The same equation was used to scale

density. Each layer of the map was linearly scaled to a lower or higher value according to its difference from the original value. Based on preceding PSF results, we hypothesize that increasing the impedance mismatch between the abdomen and the surrounding tissue will cause further deterioration of the image, primarily by increased aberration at this range of depths.

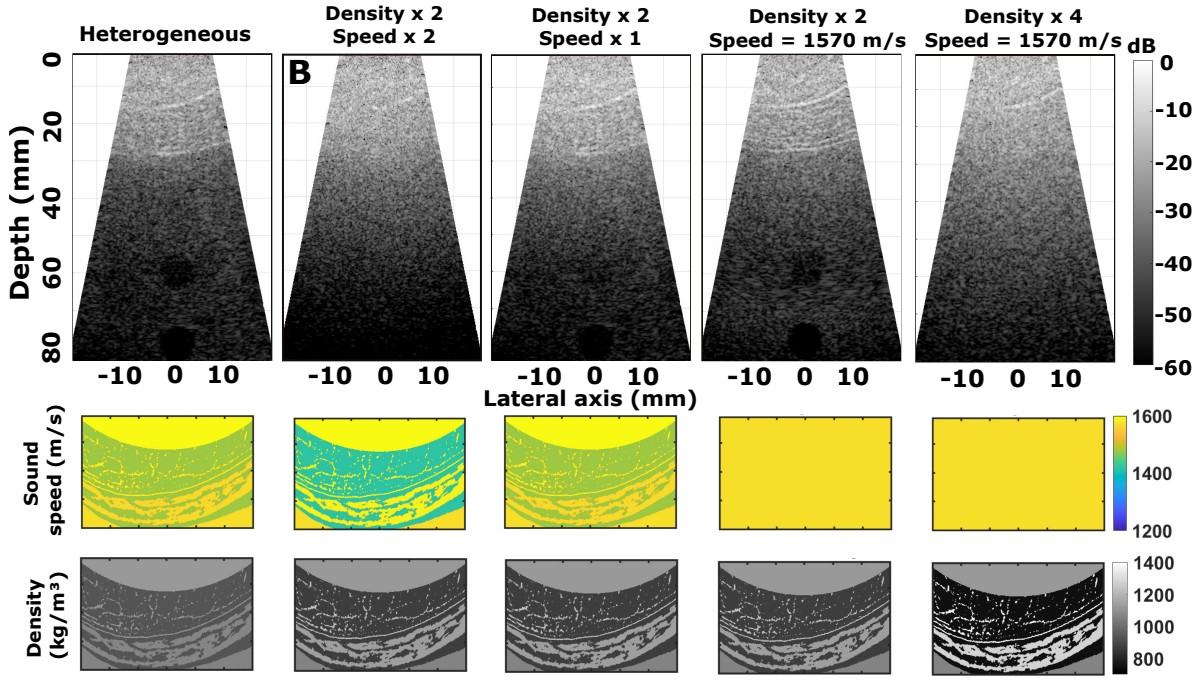

Figure 2.10: Anechoic lesion B-mode images for different configurations A-E (top row) and the respective sound speed (middle row) and density (bottom row) maps used to generate each of them. Constant speed maps are used for isovelocity B-modes equal to a homogeneous 1570 m/s.

Table 2.2: CNR for the three lesions for different cases.

Type of emission	40 mm	60 mm	80 mm
Homogeneous	3.25	4	3.9
Heterogeneous	ND	0.56	1.5
Isovelocity scaled density	1.9	3.3	3.6
Isoimpedance	0.78	0.72	1.5

To further quantify these results, the contrast to noise ratio (CNR) for each of the three lesions was calculated in some of the aforementioned cases as proposed by Patterson and Foster [122]. The results are summarized in Table 2.2 where ND stands for not detectable lesion. Adding the abdominal layer reduces the CNR of the homogeneous reference image as expected for all three lesions, while the shallow lesion at 40 mm is rendered indiscernible due to the combined effects of aberration and strong reverberation at this depth. With the presence of the abdomen but having the effects of aberration removed (isovelocity B-mode

Fig. 2.9F) the deeper lesions are fully restored in terms of CNR but the shallow lesion still shows poor contrast due to the remaining effects of reverberation. Removing reverberation from the abdominal B-mode, results in a CNR improvement for both shallow lesions but at a smaller scale than for the isovelocity B-modes. There is no CNR improvement for the deep lesion at 80 mm after removing the effects of reverberation. The isoimpedance B-mode (Fig. 2.9E) shows better contrast than the isoimpedance via subtraction counterpart (Fig. 2.9D) for the lesions at 40 and 60 mm.

Table 2.3: CNR for the three lesions for different cases of scaled maps.

Type of emission	40 mm	60 mm	80 mm
Factor 2 - Heterogeneous	ND	ND	ND
Factor 2 in density	ND	0.14	2.3
Factor 4 - Isovelocity	ND	0.38	2

As described above, the sound speed and density maps can be linearly scaled either simultaneously or one at a time and the results of some combinations are shown in Fig. 2.10B-E. The corresponding CNR values are reported in Table 2.3. Increasing both density and speed by a factor of 2 in Fig. 2.10B completely blurs the B-mode image and no lesions can be seen. Increasing only density in Fig. 2.10C by a factor of 2 renders the shallowest lesion indiscernible while the two deeper lesions can still be observed albeit with a CNR lower than for the original heterogeneous image in Fig. 2.10A. If the effects of aberration are removed while density is scaled by a factor of 2 (Fig. 2.10D), the lesion at 40 mm is still not detectable but the CNR is improved for the two deeper lesions as compared to Fig. 2.10C. Finally, in Fig. 2.10E, increasing density by a factor of 4 in an isovelocity B-mode renders all lesions indiscernible. The two bottom rows of Fig. 2.10 show a zoomed in version of the different levels of scaling of sound speed (second row) and density (third row) maps used to the B-mode image of each column A-E.

The fact that we can generate volumes of data that realistically simulate body habitus as well as break up the various components of degradation withing those data sets allows us to explore applications in fields such as machine learning. Clinical ultrasound data is not easy to come by mainly due to privacy issues. What data sets do exist are also extremely variable in target, pathology and user dependence. In order to train a neural network for i.e. improved ultrasound image processing and pathology recognition, huge volumes of data are required. With simulation tools we can generate data sets only limited by hard drive storage, thus we can have ample data for training purposes. Moreover, this data is produced in a completely controlled manner, meaning certain elements of the image can be eliminated, decreased, or amplified on demand. Using

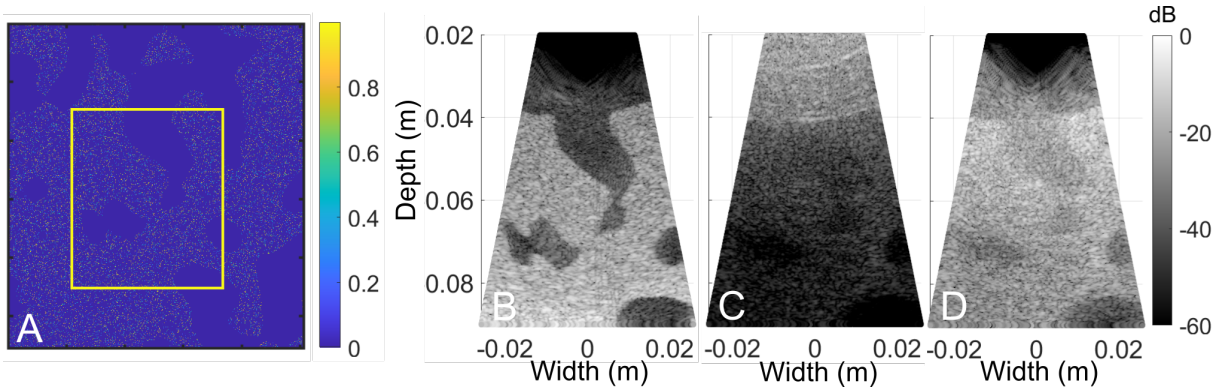

Figure 2.11: A, random lesions generated by a lesion generating algorithm. The highlighted porion will be used as an input in Fullwave simulations. B, B-mode image of the lesions in A when used as input in Fullwave in an otherwise homogeneous medium for reference. C, same lesions used through the human abdomen and D, lesions used in an isoimpedance medium. All B-mode images are in dB units and generated using a simulated C5-2v transducer at 3.7 MHz.

only one dataset of human abdominal data, in this work the VisHuman dataset, we can have practically tens of thousands of different imaging scenarios, either via translation in the 3-dimensional space or via scaling or various tissue properties, meaning certain elements of the abdomen can be removed or introduced. For example the muscle tissue can be removed during segmentation, leaving only skin, connective tissue and fat. On the other hand, extra layers can be added on top of the existing map to make the abdomen more challenging to image though. The acoustical properties of the tissue can also be tuned to affect certain image degrading properties as described above.

For each given abdominal imaging scenario, random realistic anechoic, hypoechoic or hyperechoic lesions can be easily introduced into the image. As shown in image 2.11A, lesions generated from an algorithm are converted into anechoic lesions inside a dense random distribution of scatterers. The lesions are controlled in maximum size but can be randomized enough to create a training database diverse enough to cover hundreds of different imaging scenarios.

2.4 Discussion

In this work we have shown how the individual image degradation components can be reversibly and linearly isolated, quantified and modulated in B-mode imaging through the human abdomen using the Fullwave2 simulation tool. The isolation into separate components was used to evaluate the contribution of

each depending on factors such as the brightness and the depth of the target. Initially, hypotheses regarding target brightness and depth as they relate to phase aberration and reverberation were tested, and it was indeed shown that phase aberration is independent of both target brightness and depth. It was also shown that reverberations are more pronounced for dim shallow targets, but less important for bright targets especially at large depths. It is therefore dependent on both depth and target brightness. This is due to the fact that changing the target brightness will increase the target signal magnitude compared to the reverberation signal magnitude. The effects of trailing clutter on image quality, on the other hand, are independent of target brightness. This is due to the fact that changing the target brightness will proportionally increase the magnitude of the reflected imaging pulse, which includes the trailing clutter component. In other words, trailing clutter magnitude scales with target brightness and reverberation clutter does not. Consequently, the effects of reverberation clutter on image quality depend on target brightness and the effects of trailing clutter on image quality do not depend on target brightness.

The effects of phase aberration remain relatively constant as a function of depth as well as a function of target impedance mismatch. By linearly removing its effects from the image $in\ silico$ we are able to assess the magnitude of the degradation by calculating the RMS difference between the target backscattered profile to a reference profile. In a more clinically relevant setting, we have shown that for expected values of sound speed and density mismatch, CNR values of anechoic lesions at larger depths (8 cm) are fully restored when removing aberration, whereas removing reverberations makes no perceivable difference at this depth. At a shallow depth of 4 cm, as showcased in the case of shallow anechoic lesions, removing phase aberration seems to have a similar effect to removing reverberations in terms of CNR. Determining the relative contribution of aberration and multiple reverberation is thus depth- and brightness-dependent.

Reverberation appears to have a hazing effect on the image that is largest shallower depths below the reverberating structure, in our case less than 4 cm in depth. For bright point targets reverberation has a small effect on image or PSF quality. Removing reverberation in the bright PSF analysis was only instrumental in ensuring the accurate measurement of aberration in 3.9, as it obscures correlation based measurements. In the human body, however, we seldom find such bright structures and are mostly interested in lesion-like hypoechoic or anechoic areas, like the ones discussed in Section III-B.

The contribution of reverberation in a clinically relevant anechoic lesion does affect final image quality, even if aberration relatively contributes more to degradation. If we were to estimate degradation sources only based on phantom measurements involving bright deep targets, clinical translatability at shallow depths could

be compromised due to the underestimation of reverberation effects in imaging regions of interest that are shallow and lack bright structures.

We also show that using this simulation method and by modifying the input maps we can cover ranges of impedance mismatch that include and exceed those encountered clinically. Even non-realistic scenarios of, for example, four times denser abdominal layers can be explored and the effects of image degradation can still be isolated and quantified, as we show in Fig. 2.10. This flexibility along with the freedom to simulate a variety of anatomical structures is a key advantage for the generation of a large volume of datasets for purposes of algorithm training in machine learning applications. This is supported by the fact that in silico there is an inherent advantage of having a reference, or ground truth, for B-mode images, something that cannot be achieved experimentally, let alone clinically.

CHAPTER 3

QUANTIFICATION OF ABERRATION AND REVERBERATION IN TRANSCRANIAL ULTRASOUND IMAGING

The skull bone, due to its acoustical properties and morphology, significantly aberrates ultrasound imaging pulses. The large impedance mismatch between tissue and high sound speed bone is also responsible for multiple reverberations between the surfaces of the skull and transducer. Even though a significant amount of research has been dedicated to correcting the phase aberration, comparatively few results exist on multiple reverberation. The objective of this paper is to quantify reverberation clutter in brain imaging with high resolution measurements of the skull morphology, 2D and 3D nonlinear acoustic simulations of ultrasound propagation, point spread function analysis of image quality in 2D and 3D and lastly anechoic lesion measurements through the skull, using spatial coherence and contrast to noise ratio (CNR) measurements as metrics of image quality. A full-wave equation simulating nonlinear propagation in a heterogeneous medium is solved numerically with finite differences in the time domain, to explore the degrading effects of the human skull. The simulations were calibrated using registered experiments through a human skull sample, which was subsequently converted from a CT scan to input maps of sound speed, density and attenuation. Phase aberration and reverberations were isolated in the resulting B-mode images and their contribution to image quality degradation was quantified while imaging bright point targets and anechoic lesions in the presence of scattering tissue.

3.1 Introduction

Research on ultrasound propagation in the brain has been directed towards therapeutic applications [180, 9, 69] and to a lesser extent towards brain imaging. The skull is a strong phase aberrator that degrades the image quality and several methods have been developed in the past decades to correct this aberration [180, 72]. However, multiple reverberations, between the skull and the transducer or within the skull, also have an impact on image quality, yet their effect has not been extensively studied or characterized. We thus hypothesize that

in transcranial imaging, two sources of image degradation are the most prevalent: phase aberration, stemming from the heterogeneous composition of the skull which distorts the phase and amplitude of the wave, and reverberation, caused by the multiple reflections in the heterogeneous layers of the skull. The objective of this paper is to quantify the reverberation clutter in brain imaging and to determine its effect on image quality, and it contribution to image degradation relative to phase aberration.

Fig. 3.1 illustrates schematically the effects of reverberations and aberration on the point spread function (PSF) generated from a point scatterer in a homogeneous medium and in the absence of reverberations and aberration respectively. The PSF is described by the "X" shaped region at the depth of the scatterer, with the main lobe being the lateral center of the "X" and is illustrated in the bottom row of Fig. 3.1. Three distinct regions can be identified with respect to the arrival time of the wave and the PSF. The preceding region contains signal that has not traveled to the PSF yet, and includes the effects of reverberations from structures closer to the transducer. The isochronous volume contains signals originating from inside the bow-tie area, and lastly the trailing region temporally trails the isochronous volume, with signals that have had time to travel past the bow-tie shaped part of the PSF and back to the transducer. Phase aberration and its effect on the transmitted and reflected wavefront is illustrated in the second column of Fig. 3.1. Aberration is generally depth-independent and target-brightness independent. Reverberation can be broken up into two sources of image degradation: multiply-reflected sound that returns to the transducer and is overlaid on top of sound returning from deeper ranges, and multiply-reflected sound that is transmitted beyond the layered media that contributes to a low-amplitude lengthening of the transmit pulse [**?**]. Their effect is illustrated in the third column of Fig. 3.1. Reverberation causes the hazing effect overlaid on top of the PSF, stemming from consecutive reflections on the layers of the skull characterized by different impedance values. Since bone is a strong reflector, apart from the classic multipath reverberation following the different impedance interfaces, such as the skull, the distance of the skull from the transducer is also important, since reflections occur not only from within the skull region but also between the very skull surface and the transducer, causing reverberations in the are preceding the skull.

In the past techniques to quantify and correct for phase aberration have been established and validated in the context of brain therapy, where the use of hydrophones was considered the gold standard [23]. In other studies [180, 145], the phase aberration was calculated by transmitting an outward propagating pulse from a point target at the focus to the transducer, and the corrected wave was re-transmitted from the transducer to the point target. Recent literature focuses on estimating the true sound speed in transcranial imaging using

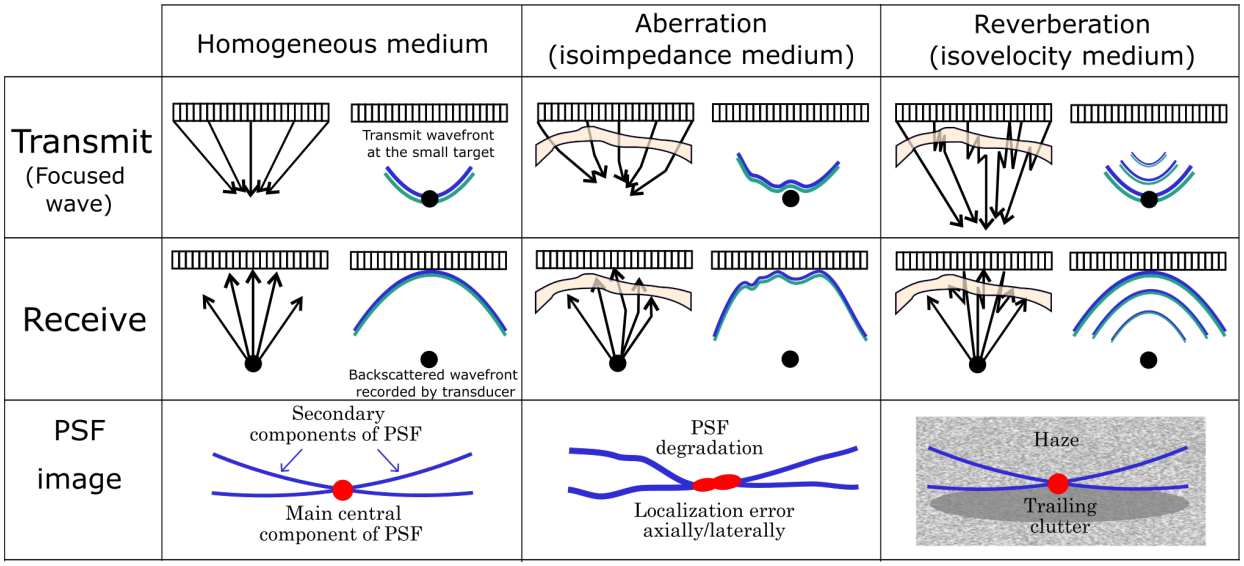

Figure 3.1: Schematic illustrating the effects of multiple reverberations and aberration on a PSF. Homogeneous case provided as a reference.

synthetic aperture imaging to mitigate the effects of refraction [112]. Deep learning approaches have also recently used neural networks to correct for the skull induced distortion from the acquired RF signal [45]. For the characterization of reverberation clutter in conventional ultrasound imaging, as well as the quantification of the contribution of aberration and reverberation to the degradation of the 3D PSF at both the fundamental and first harmonic frequency, phase aberration maps and point spread functions (PSF) have been previously used in human abdominal imaging [150, 134]. Clutter reducing methods, such as tissue harmonic imaging have also been applied to transcranial ultrasound to improve image quality in order to better visualize distinct brain regions [**?**], however the role of reverberations on image quality has not been looked at in detail.

Characterization of acoustic waves that propagate nonlinearly in an inhomogeneous medium has numerous applications in diagnostic and therapeutic ultrasound. The nonlinearity of wave propagation is used to the advantage of diagnostic scanners that use the harmonic components of the ultrasonic signal to improve the resolution and penetration of clinical scanners [188]. Ultrasonic propagation through fine scale heterogeneities has been simulated previously with a finite difference time domain (FDTD) solution of the 2D and 3D linear wave equation [100, 99]. Recently, we have developed a numerical solution [150, 148] to a full-wave equation that, in addition to simulating the nonlinear propagation of waves, describes arbitrary frequency dependent attenuation and variations in density. This full-wave nonlinear acoustic (FNA) code has been used to generate ultrasound images and to study therapeutic ultrasound for treatment of the brain [134, 145]. In this paper,

we quantify aberration and reverberation clutter in 2D and 3D through the temporal acoustic window of the human skull, which was measured with computed tomography. The simulation was calibrated to a water tank experiment using a registered skull sample in terms of reverberation strength and root mean square aberration values. Tissue simulating random scatterer distributions were also calibrated in terms of average speckle brightness.

In this paper, we quantify aberration and reverberation clutter in 2D and 3D through the temporal acoustic window of the human skull using experiments and Fullwave simulations. Water tank measurements are used to determine reverberation strength and root mean square aberration values. The acoustical properties of the skull sample are then measured with computed tomography and converted into simulation maps. The simulation is calibrated to a water tank experiment using this registered skull sample. Soft tissue is also calibrated in terms of average speckle brightness. To elucidate the relative contribution of phase aberration and reverberation in transcranial image quality, two imaging scenarios will be explored: Bright point targets at various imaging depths though the skull as well as transcranial anechoic lesion imaging in calibrated tissue at different focusing depths will be described in the next sections. The combination of both analyses at multiple depths will better showcase the dependency of these mechanisms on the nature of the target (reflectivity, presence of scattering environment) and the imaging depth.

3.2 Methods

Bone has a complex architecture. It has an anisotropic heterogeneous porous structure with strong variations in its material properties (more than a factor of two variations in the speed of sound between bone and bone marrow). The average trabecular element is between 50μm and 150μm, with a separation that ranges in between 0.5mm and 2mm, which is close to the typical wavelengths used in brain imaging. Conventional computed tomography does not have a sufficient resolution to image these properties.

In a previous publication we measured the bone micro-architecture of a human skull sample with 3D microtomography at a 10μm resolution [147]. This quantitative X-ray phase contrast imaging was performed with the experimental station ID19 of the European Synchrotron Radiation Facility (Grenoble, France). Prior to quantifying the main degradation mechanisms transcranially, the aforementioned 3D data set was used to determine whether a conventional CT is sufficiently accurate to model the reverberating properties of the cortical and diploe regions of the skull bone. The left image in Fig. 3.2 shows a 2D section of the synchrotron

data with an isotropic 10μm resolution. The image on the right shows the same data set after it has been downsampled to a resolution of 800μm, which is the typical resolution of CT scanner, and then interpolated back to the original 10μm resolution. This data was then converted to maps of the acoustical properties of bone, as shown in Table 3.1. In this section the attenuation of the cortical bone was set to 2.8 dB/MHz/cm. In the following sections, where low resolution images are used, the attenuation is set to 13 dB/MHz/cm to compensate for the lack of microstructure [147].

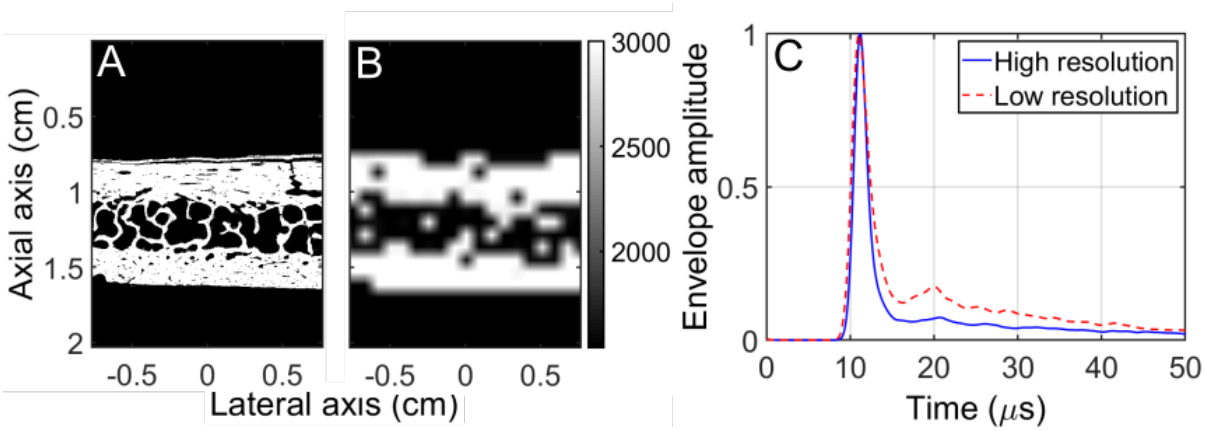

Figure 3.2: A, a 2D section of the 3D synchrotron data with an isotropic 10μm resolution. B, the same data set after it has been downsampled to a resolution of 800μm and then interpolated back to a 10μm resolution. C, the envelope detected amplitude of the imaging pulse after propagating through the high resolution map (solid) and the low resolution maps (dashed) shown in A and B.

Table 3.1: The acoustic properties of cortical bone in the skull used in the wave propagation simulations.

Material Parameter	Cortical Bone	Soft tissue
Density (ρ)	1850 kg/m^3	1000 kg/m^3
Speed of sound (c)	3000 m/s	1540 m/s
Nonlinear parameter (B/A)	7.6	7.6
Attenuation (dB/MHz/cm)	2.8 or 13	0.3

A 1 MHz 2 cycle Gaussian enveloped pulse was transmitted into this medium from a planar surface at 0.4 cm depth. The simulated signal was recorded following propagation through the bone, along the plane at depth 1.65 cm for a duration of 50μs. This received signal was envelope detected and averaged over the plane. It is plotted in Fig. 3.2C as a solid line for the high resolution medium, and as a dashed line for the low resolution medium. The ballistic pulse can be observed at approximately 12μs and the reverberating coda can be observed following the pulse. The low-resolution map results in a significantly more reverberating

medium, with a coda amplitude that is almost twice as large as observed in the high-resolution map. However the bone sample in Fig. 3.2A and B comes from a thick part of the skull, with a thickness of approximately 8-9mm. The temporal window that is typically used for imaging, on the other hand, is much thinner, between 1 and 3 mm, and it is composed entirely of cortical bone. The map was truncated at a depth of 1.1 mm so that the only cortical bone with a thickness of 3 mm is included (shown in Fig. 3.3).

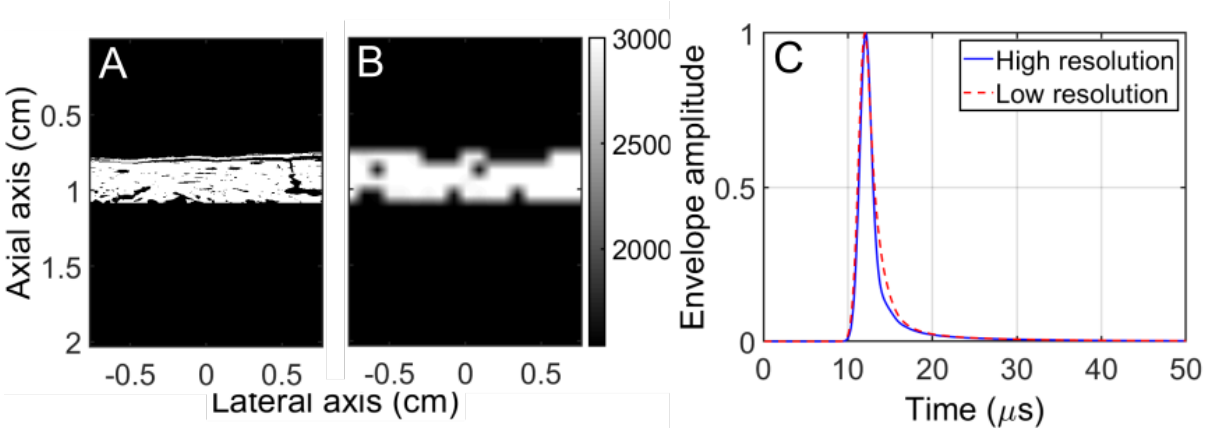

Figure 3.3: A, a 2D section of the thin 3D synchrotron data with an isotropic 10μm resolution. B, the same data set after it has been downsampled to a resolution of 800μm and then interpolated back to a 10μm resolution. C, the envelope detected amplitude of the imaging pulse after propagating through the high resolution map (solid) and the low resolution maps (dashed) shown in A and B.

The envelope detected pulse for this more realistic map as measured at 1.65 cm is shown in Fig. 3.3C. In this case there is an excellent agreement between the high-resolution and low-resolution maps.

3.2.1 Acoustic propagation simulations

In recent work, a model of the quadratically nonlinear wave equation with multiple relaxations as a function of space that can model perfectly matched layers was shown [148]. This model is solved using finite differences in the time domain on a parallel architecture, and solutions are demonstrated in 2D and 3D [141] for ultrasound imaging applications involving heterogeneous media simulating the human body. In this work, for the 2D simulations described, a Linux Fedora 25 (v.4.10.13-200.fc25.x86 64) system running Intel Xeon® E5-2630 v4 processors at 2.20 GHz was used. for the 3D simulations, a Linux Ubuntu 20.10 system running Intel Core® i9-9820X processors at 3.30 GHz was used.

3.2.2 Skull map calibration

Experiments using a P4-1 probe at 2.5 MHz were performed using a 250 μm nylon wire (Berkley Nanofil) as an imaging target in water and through a human skull specimen. Specifically, a temporal piece of a human skull was used, since it usually provides a realistic case in transcranial imaging. A 3D printed custom holder that holds the P4-1 transducer and the skull piece in a registered manner was used for the experiment. The wire target was placed at 50 mm of depth from the transducer, and a fixed focus pulse was emitted, focusing at the depth of the target. The PSF acquired for this out-of-plane target was then compared with a PSF of the same target in water to calculate the root mean square difference value between the backscattered profiles of the wire transcranially and in the homogeneous medium.

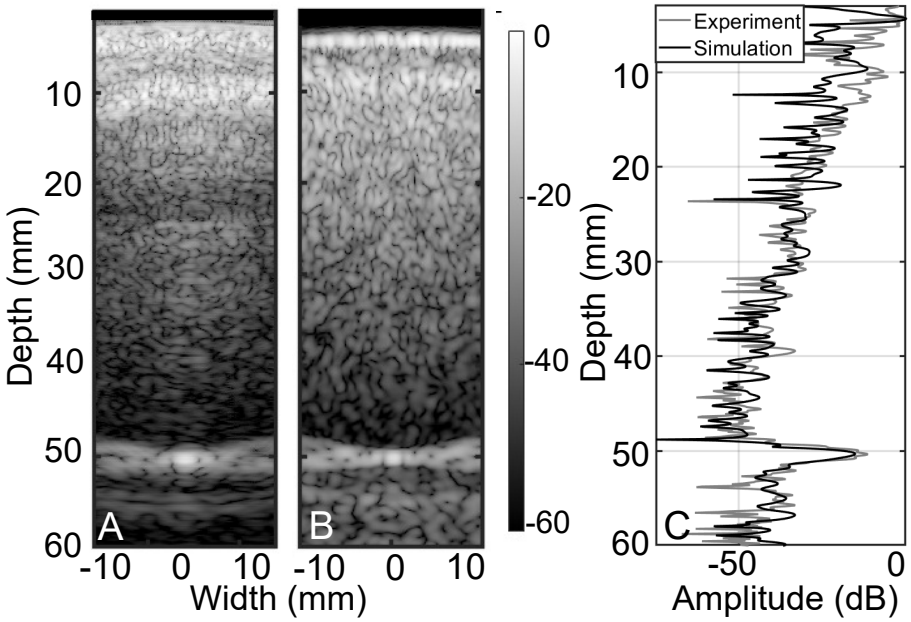

Figure 3.4: A, experimental B-mode for a 2.5MHz emission through a human skull. B, simulation B-mode using a skull map converted from a CT scan of the same skull specimen. C, reverberation curves for images A and B.

To make the calibration as accurate as possible, the same transducer holder with the skull piece attached was CT-scanned using a micro CT. The CT maps in Hounsfield units were converted to density and the 2D slice corresponding to the middle of the physical transducer was chosen for the simulations. To ensure calibration, reverberation curves between simulation and experiment were compared. As shown in Fig. 3.4, the reverberation pattern is acquired by laterally averaging the beamformed images of the both simulation and experiment counterparts and then plotting them as a function of depth. The aberration values were measured

by the root mean square values of the target backscaterred profiles transcranially and in a homogeneous medium (water) and were 53 ns for the experiment and 57 ns for the simulation. At this aberration value the specific skull specimen is considered mildly aberrating.

Simulations were run at the same frequency of 2.5 MHz, with an initial pulse pressure of 0.3 MPa. Two realisations were explored, one in a homogeneous medium (uniform sound speed of 1540 m/s and density of 1000 kg/m^3) and one transcranially, using the same acoustical maps shown in Fig. 3.5. To ensure the introduction of non-linearity in the medium, a constant value equivalent to that of tissue (Goss et al.) was assigned to the non-linearity map.

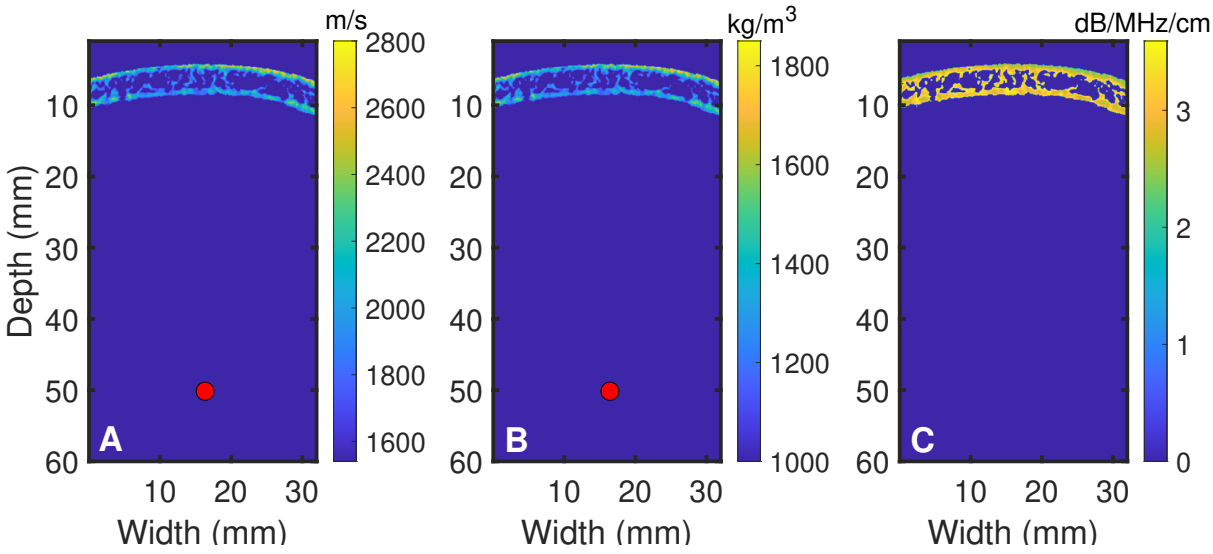

Figure 3.5: Input field maps for Fullwave2: Sound speed (A), density (B) and attenuation (C). The size of the target at 50mm is exaggerated.

3.2.3 Speckle calibration

To simulate tissue realistically, calibration against tissue liver tissue data was performed. The pressure output as a function of voltage for the transducer used in experiments (P4-1 at 2.5MHz) was measured via hydrophone and at a transmit of 5V, a pressure of 259 kPa is emitted. Data of fresh porcine liver immersed in water were also acquired, using a focused wave with a fixed focus at 50mm. From the B-mode images we measured the average brightness of the liver tissue, while averaging through 10 different elevation slices as well as 100 frames per elevation position at -33 dB.

In silico, tissue was simulated by inserting multiple scatterers with a density of 15 scatterers per wavelength cell, with a density variation in the order of 0.5% compared to a background density of 1000 kg/m^3.

Using this speckle distribution, anechoic lesions, where scatterers are completely absent, can be inserted in our sound speed input maps. Lesions are also set to be non-attenuating, while the scattering medium has an attenuation value equal to 0.5 dB/cm/MHz, which is typical for healthy liver for which the speckle calibration was performed [94]. To successfully resolve a circular anechoic lesion with a radius of 5 mm transcranially, a multi-focused emission approach is used, where at 2.5 MHz, 48 individual foci are used, spaced 0.4 mm apart laterally, at a constant focal depth equal to the center of the lesion. The raw data acquired is beamformed and then combined into a single B-mode, with each lateral area corresponding to its respective focus. Isoimpedance and isovelocity versions of these simulations are also ran to evaluate how aberration and reverberation affect the ability to resolve the lesion, as well as its contrast to noise ratio.

3.2.4 Isolation of the components of image degradation

To quantify the contribution of aberration and reverberation in the total clutter produced by the insertion of the human skull, using the acoustical skull maps shown in Fig. 3.5 isoimpedance and isovelocity B-mode images are generated.

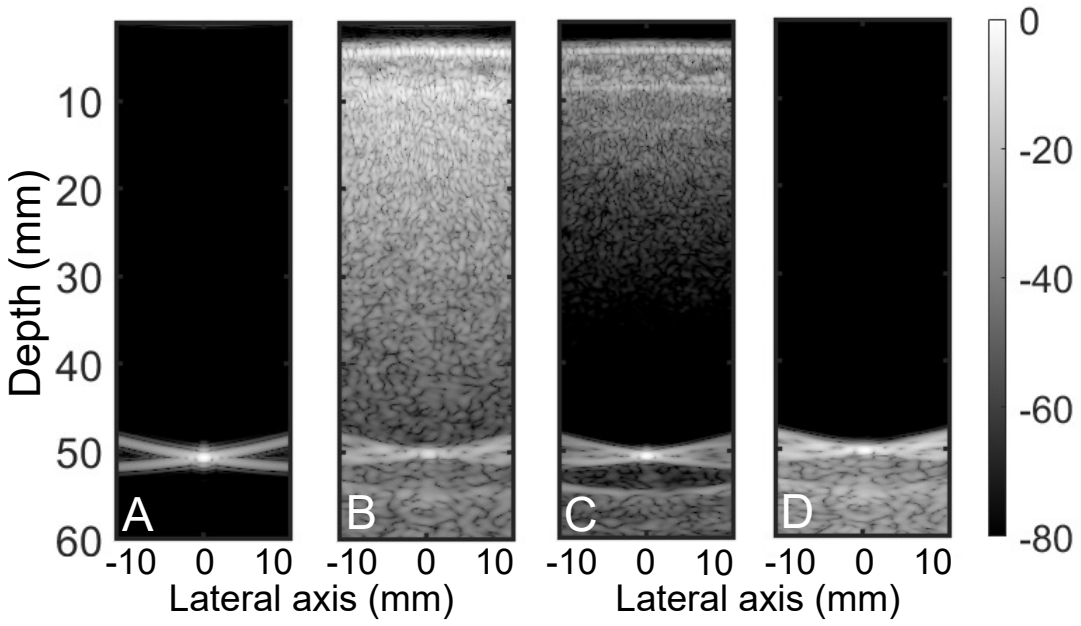

Figure 3.6: A,homogeneous B-mode of a target at 50 mm. B, transcranial B-mode of the target. C, isovelocity B-mode where all effects of aberration are removed. D, isoimpedance B-mode where the clutter has been subtracted and multiple reverberations are removed.

Isoimpedance B-modes result in the elimination of the effects of reverberation, whilst preserving aberration. This process comprises two steps, propagating a wave through the acoustical maps alone, without the presence of a scatterer, and then linearly subtracting it from the heterogeneous B-mode image as shown in Fig. 3.6B described to finally obtain isoimpedance B-mode shown in Fig. 3.6C. To generate the isovelocity B-mode, where aberration is removed and reverberations persist, sound speed is set to be constant at a value of 1540 m/s through the entire field, while density is scaled appropriately so that impedance retains its original value, yielding image Fig. 3.6D.

3.2.5 3D Simulations

The effects of the skull in ultrasound imaging were also explored in the 3D space. In this case, instead of the P4-1 transducer, a custom designed 1.5MHz 1024-channel 2-D sparse array shown in Fig. 3.7A was used. This array was optimized for human transcranial imaging and has a 65-mm circular aperture, with elements arranged in a sparse tapered spiral. This allows for the transmit of an apodized beam with high focal gains and low side lobes. The custom sparse array transducer is shown in is shown in Fig. 3.7A and an illustration of the arrangement of the elements on the transducer surface is shown in Fig. 3.7B.

A 3D CT data set was obtained from a healthy volunteer made with a Siemens CT VA1 (Siemens Medical Solutions, Erlangen, Germany) machine with a slice thickness of 1 mm, and an in plane resolution of 0.78 mm. Using a temporal window, a 3D segment of the skull was selected for imaging and converted from its original Hounsfield units to density, speed of sound and attenuation maps. The maximum and minimum values for the above properties of the skull were selected in the same way as for the 2D simulations. The sound speed maps used in the simulations are shown in Fig. 3.7C-E in all 3 configurations. Note that configuration Fig. 3.7E most closely corresponds to the direction in which the wave propagates for one elevational slice.

3.3 Results

3.3.1 2D transcranial simulations

Transcranial 2D simulations were run for different focusing depths ranging from 30 to 70 mm. For a shallow depth of 30 mm, we hypothesize that the reverberation will contribute more to image degradation whereas at depths of 60-70 mm, we hypothesize that aberration will play the main role in image degradation, while reverberation will be insignificant due to the large distance from the reverb zone. This is indeed

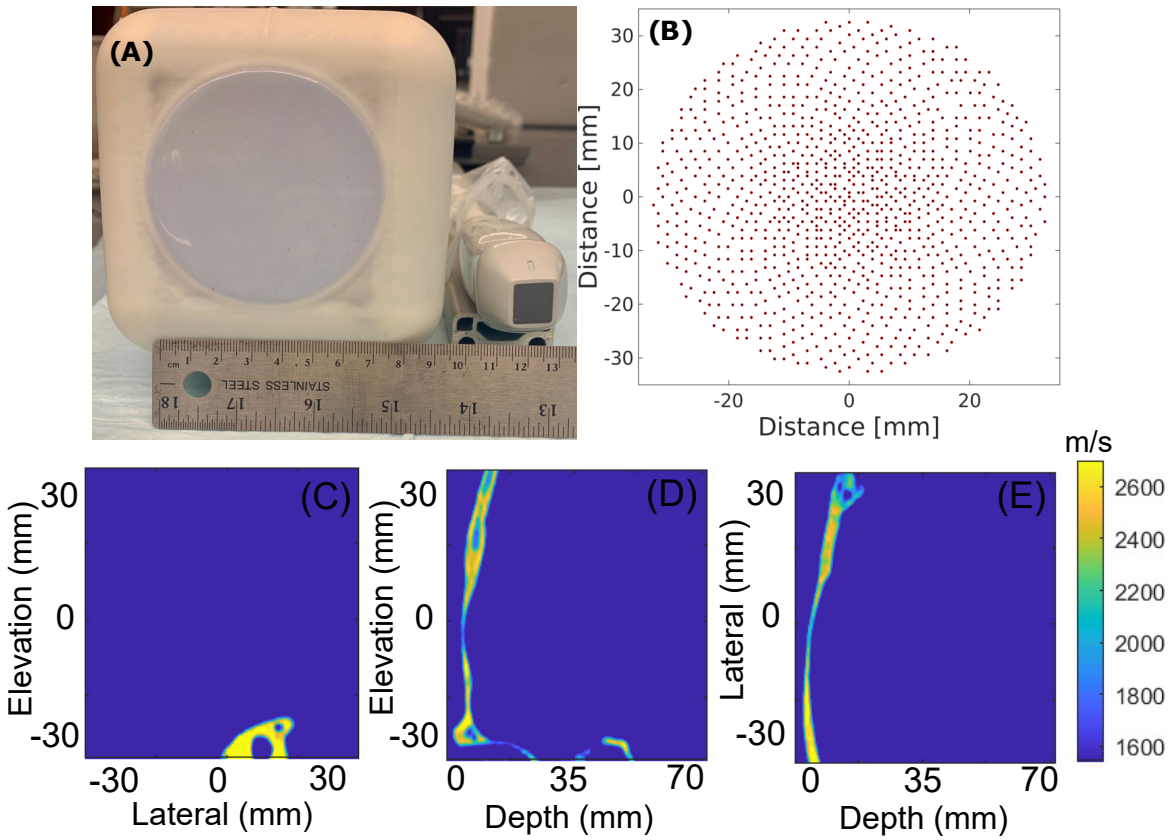

Figure 3.7: A, 2-D sparse array that is simulated in the 3D section of the paper and B, its actual element distribution in space. C-E, sound speed maps derived from a 3D CT scan shown in three different planes. Units are in m/s

corroborated in Fig. 3.8, where we see that in case A reverberation severely impacts the quality of the psf. In image B the effect decreases but is still evident and finally in image C and at a depth of 60 mm, reverberation has already subsided to values below -60 dB.

Table 3.2 summarizes the average dB values of the preceding regions, isochronous volume and trailing regions of the PSFs for different depths of the scatterer, as also shown in Fig. 3.8.

Table 3.2: Mean magnitude of three PSF regions in dB for different scatterer depths.

	3 cm	4 cm	5 cm	6 cm
Preceding region	-33	-42	-52	-60
Trailing region	-34	-38	-42	-45
Isochronous volume	-34	-35	-38	-39

In Fig. 3.9, the same simulation shown in Fig. 3.8B for a target at 40 mm is ran, but the target impedance is changed with respect to the background to values of 1, 0.5 and 0.01 MRayl. There is no difference in either

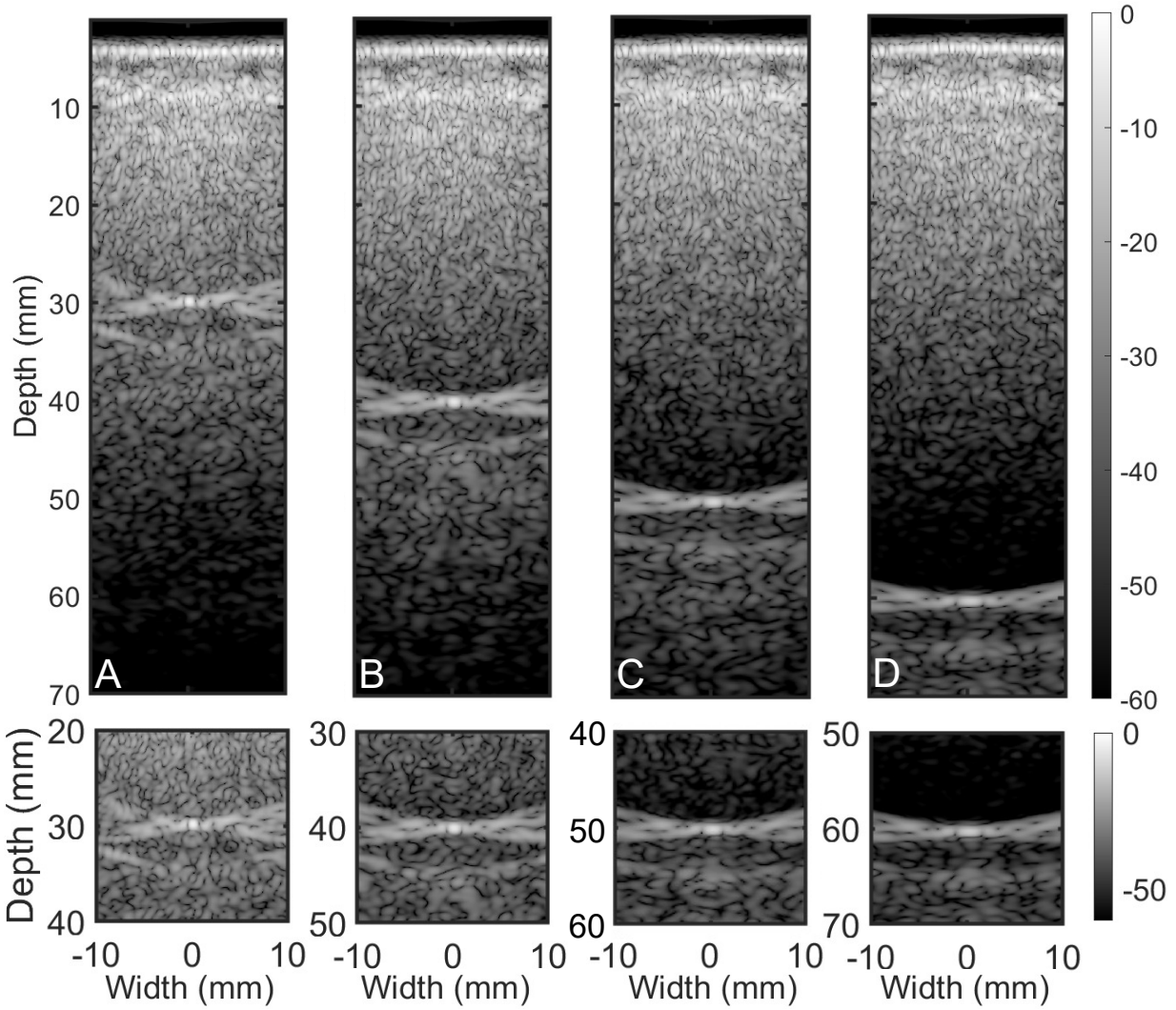

Figure 3.8: PSFs of a point target at (A) 30 mm, (B) 40 mm and (C) 60 mm transcranially. Units are in normalized dB.

aberration values or multiple reverberations originating from the skull itself, as shown in Fig. 3.9D, however trailing clutter scales proportionally with increasing impedance mismatch. For a low impedance mismatch trailing clutter is at the same amplitude level as the preceding region, but as impedance increases so does the trailing clutter, reaching values only 5 dB lower than the PSF maximum value for an impedance mismatch of 1 MRayl.

Even though a PSF of a bright point target inside a homogeneous medium allows us to measure aberration and extract reverberation curves easily, it is not a realistic indicator of physics inside the brain. To showcase how the insertion of tissue affects the PSF we previously analyzed, the equivalent of brain tissue was introduced in the simulations. As shown in Fig. 3.10C and D, gray and white matter regions,converted from

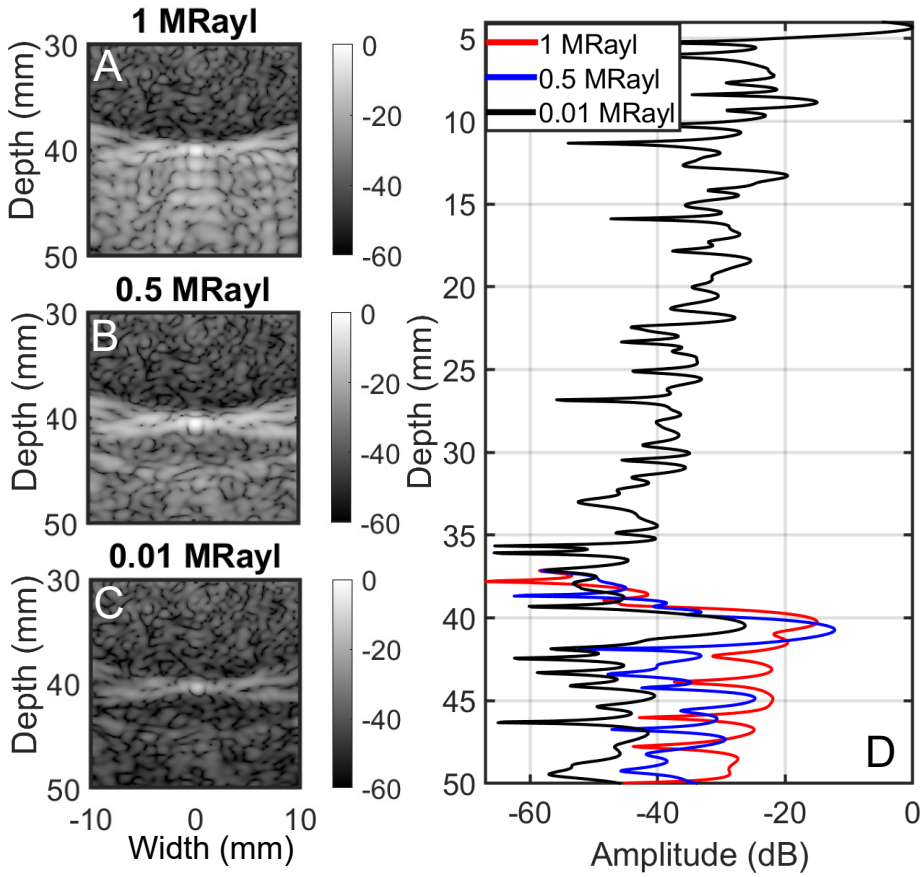

Figure 3.9: PSFs of targets that have their sound speed scaled by A, 10%, B, 20% and C 50% with respect to their original value. D, reverberation curves for the same images. Note how the trailing clutter scales with increasing impedance mismatch.

an optical histological brain image, were inserted in the input maps along with a random distribution of scatterers of a sound speed of 1552 m/s as shown in Fig. 3.10D. Table. 3.3 summarizes the values of different regions corresponding to the brain. The point target is kept at a depth of 40 mm and if we compare the B-mode image in Fig. 3.10A to Fig. 3.8B it is evident how reverberation plays a far more dominating role in the presence of tissue. Fig. 3.10B shows the reverberation curves for both cases and how inserting brain tissue reduces the target brightness by 18dB, mainly due to multiple scattering.

Table 3.3: Sound speed and density values for different simulated brain regions.

	White matter	Gray matter	Fluid
Sound speed (m/s)	1552.5	1500	1504
Density (kg/m^3)	1046	1045	1041

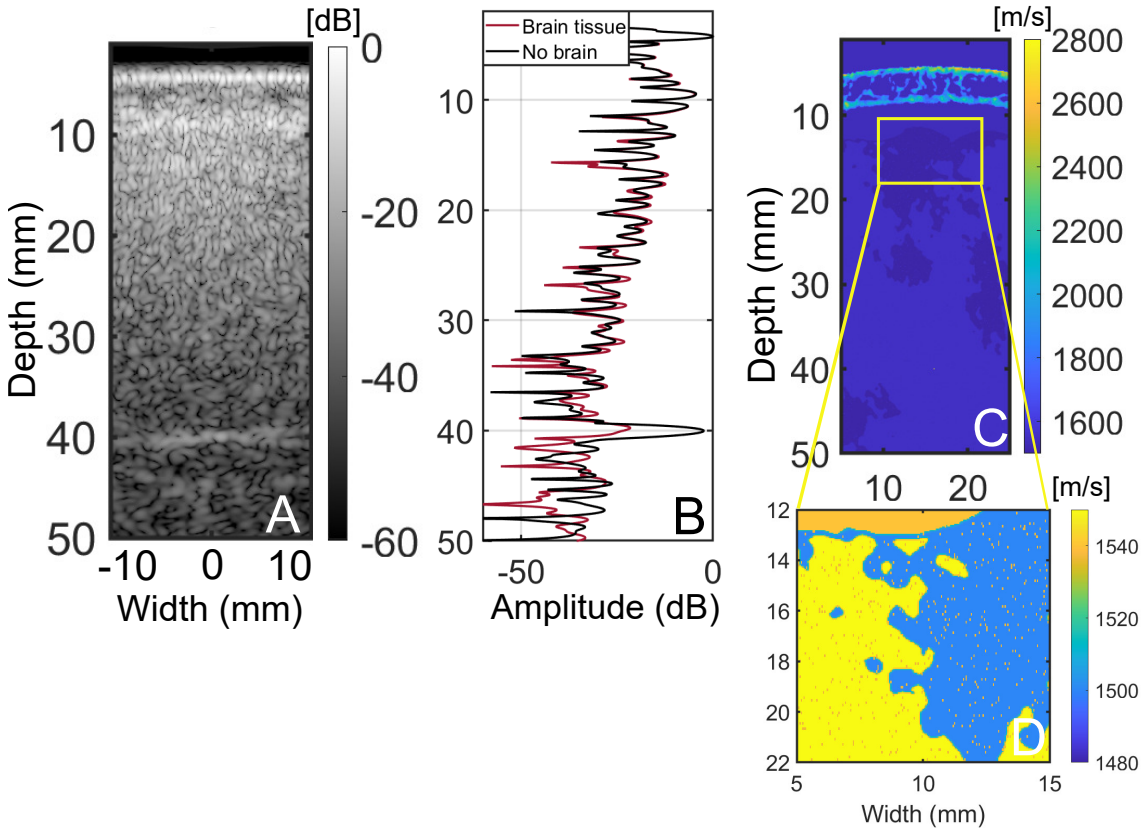

Figure 3.10: A, Transcranial B-mode including brain tissue. B, Reverberation curve comparison between simulation including brain and without brain tissue.

Lastly the effect of harmonic imaging on the PSF was explored. The emission was set at a frequency of 1.25 MHz instead of the 2.5 MHz used in the previous cases and the resulting RF data was filtered at the fundamental and first harmonic, as shown in Fig. 3.11A and B respectively for a homogeneous reference case and Fig. 3.11C and D for the transcranial case. Fig. 3.11E shows the beamplots for all cases A-D. Harmonic imaging reduces the width of the main lobe in both homogeneous and transcranial cases. As far as reverberation clutter is concerned, harmonic imaging decreases its amplitude by an average of 15 dB.

3.3.2 3D transcranial simulations

The simulation is 8 cm deep, 6.5 cm wide, and 6.5 cm in elevation, which corresponds to the physical dimensions of the sparse array, as shown in Fig. 3.7A. The transducer emits a focused imaging pulse towards a bright spherical target at a depth of 40 mm. As the wave propagates part of the energy is trapped in multiple reverberations between the bone surfaces and the transducer. Part of the pulse is reflected by the point

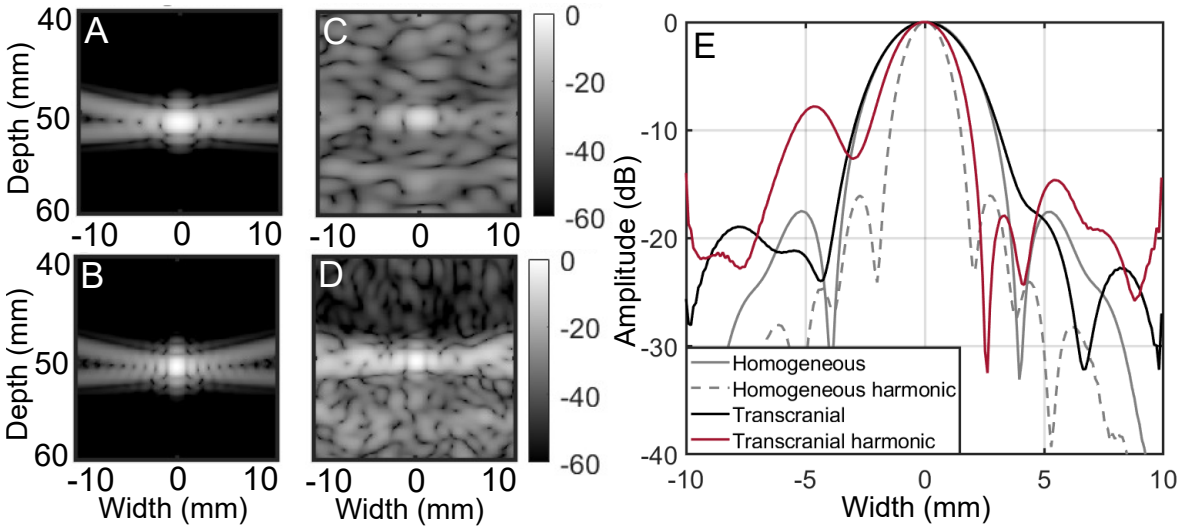

Figure 3.11: PSFs from an unapodized transducer in a homogeneous medium (left) and transcranially (right) for a target at a depth of 50 mm, for the fundamental frequency of 1.25 MHz (A,C) and the first harmonic frequency of 2.5 MHz (B,D). The PSFs have been normalized relative to their peak. All scales have units of decibels. E, beamplots for PSFs A-D.

scatterer at the focus. The signal is then measured at the transducer surface and used for 2D delay and sum beamforming operations.

Table 3.4: Average magnitudes in absolute dB values of the three regions in different cases for a spherical target at 40 mm

	Preceding	Trailing	Isochronous
Homogeneous	76	83	106
Heterogeneous	102	99	100
Isoimpedance	63	87	93
Isovelocity	91	86	93

The PSF can be determined by making an image of the point target. The total PSF includes both the effects of phase aberration, reverberating clutter, and trailing clutter. The PSFs for for different cases are shown in Fig. 3.12. The PSF for a spherical target in a homogeneous medium is shown in the leftmost column of Fig. 3.12. The PSF with the skull bone in place with both the effects of aberration and reverberations included is shown in the second column and the clutter in the absence of a target is shown in the middle column. Since there is no point target this PSF is calculated entirely from signal that is reverberating between the bone and the transducer. The fourth column shows the result of the subtraction of column three from column two, i.e. the subtraction of clutter from the PSF. Note that in the area preceding the isochronous volume there is no signal. However there is signal following the PSF. This corresponds to the trailing

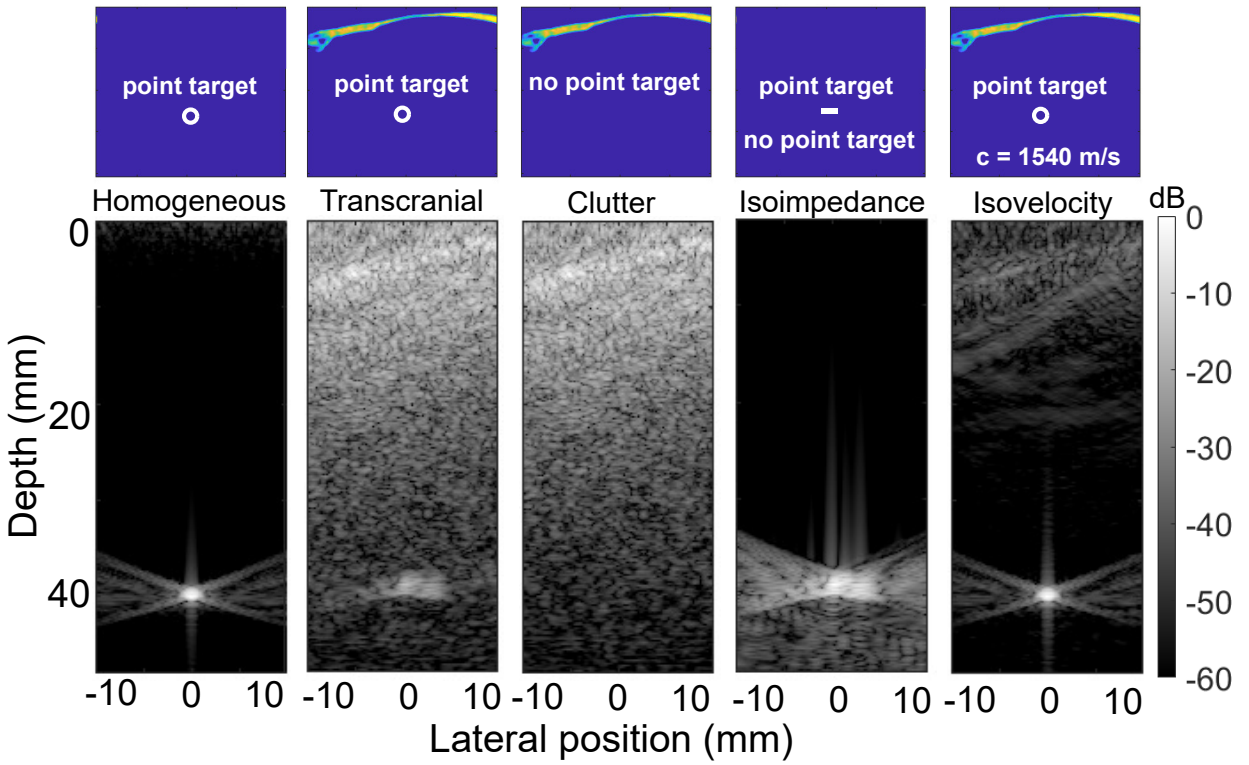

Figure 3.12: B-mode images for 3D simulations (second row) corresponding to different imaging scenarios shown schematically (first row).

distortions of the ballistic pulse. Lastly removing the effects of aberration by setting the speed of sound to be constant and scaling density appropriately to preserve impedance, yields the image in the last column of Fig. 3.12. Qualitatively, removing phase aberration restores the shape of the PSF completely. All B-mode images are normalized with respect to their maximum, the actual amplitude of the PSF regions cannot be accurately interpreted in the images.

To further quantify the contribution of each degradation mechanism mesurements of the average amplitude in absolute dB units of different PSF regions is summarized in Table 5.1. The PSF can be divided into three regions: First the isochronous volume, which is the bow-tie shaped figure centered at the focus. Signals within this volume have had time to travel from the transducer to the target and back again. Second, the region above the isochronous volume which corresponds to times that precede the arrival of the target signal. For example: multiple reverberations. Three, the region trailing the isochronous volume which corresponds to times that follow the arrival of the target signal. Interpreting Table 5.1, and using the homogeneous values as a reference, inserting the skull in the heterogeneous case increases the dB values of the preceding and trailing regions by 26 and 16 dB respectively. Removing the effects of phase aberration restores the amplitude of the

preceding and trailing regions by 11 and 13 dB respectively, while removing the effects of reverberations restores the amplitude of the trailing region by 12 dB. In the case of the preceding region, the mean values of the preceding region is lower even than the homogeneous case. This is due to the clutter subtraction operation which removes not only reverberation clutter, but also any remnants of emission signal that might persist and might be exaggerated by post-processing operation (envelope detection, filtering around emission frequency).

3.3.3 The relative importance of clutter and aberration in image quality

For a bright point target in a homogeneous background,as shown in the previous section for the 3D simulation analysis, reverberation appears to have a secondary effect on image quality. However, to model a realistic brain imaging scenario where scattering tissue is present and imaging targets are not as bright, an anechoic lesion of a 1 cm diameter was inserted in the calibrated scattering medium, at different imaging depths.

Fig. 3.13, shows the B-mode images of the anechoic lesions for 4 different imaging scenarios and at different depths. The homogeneous case, without the human skull is used a reference. The human skull is inserted in the transcranial case, the effects of multiple reverberations are removed in the isoimpedance case and the effects of aberration are removed in the isovelocity case. These simulations were performed for the lesion situated at 3, 4, 5, 6 and 7 cm of depth, while only three of these cases are illustrated in Fig. 3.13. It appears that reverberations are the dominant source of image degradation at least up to 5 cm of depth, with phase aberration improving image quality mainly after the 5 cm mark. In the transcranial case, where both mechanisms are present, the lesion is not clearly discernible until 7 cm of depth, where reverberations are substantially lower and phase aberration is virtually the only source of image degradation.

Coherence curves as well as Lag-One Coherence (LOC) measurements are also performed for the different anechoic lesion cases shown in Fig. 3.13. Spatial coherence is sensitive to wavefront degradation due to aberration as shown in literature [80]. It has also been shown that in the presence of reverberation clutter, rapid decorrelation in spatial coherence at very short lags occurs [**?**].

In Fig. 3.14A, the spatial coherence curves are shown for the homogeneous B-mode for a shallow depth of 3 cm. The correlation coefficients are calculated as a function of inter-element lag for RF data corresponding to the anechoic interior of the lesion, the surrounding tissue outside of the lesion and lastly the ideal theoretical case as described by the Van Cittert-Zernike theorem for a random scatterer distribution [96]. For tissue without added noise the curve approximates the Zernike curve, whereas for an anechoic lesion

as expected it decorrelates very quickly, since tissue is absent. In Fig. 3.14B, the coherence curves for the transcranial case are shown and C and D for the isovelocity and isoimpedance cases respectively. All curves are derived from lesions at 3 cm of depth. Even though conclusion based on the quality of the interior of the anechoic lesion are hard to establish between B,C and D, it is evident that at a shallow depth, tissue outside of the lesion is less affected by removing aberration (Fig. 3.14C) than removing reverberations (Fig. 3.14D), since the curve better approached the homogeneous case. Both heterogeneous and isovelocity cases seem to be equally decorrelated inside and outside the lesion, signifying the image is degraded.

CNR measurements can indicate the quality of the lesion in the B-mode image and by extension the relative contribution of reverberation and phase aberration when comparing isoimpedance and isovelocity B-modes respectively. Fig. 4.7 shows the CNR values for the isovelocity and isoimpedance B-modes as a function of lesion depth. The absolute CNR values measured are not of note here, since each B-mode case measured is normalized by its local maximum which differs significantly between isoimpedance and isovelocity cases given that in the isovelocity B-modes the maximum is found within the skull region, whereas in the isoimpedance case the skull is artificially removed. What is of importance is the trend of the curves, which can be used to evaluate how CNR behaves as depth increases, with isovelocity values increasing and isoimpedance values decreasing with increasing depth. In Fig. 4.7 the qualitative observation that phase aberration and reverberations start to equally contribute to image degradation around 5 cm of depth is corroborated. Past that depth removing aberration appears to have a higher impact on image quality, whereas at shallower depths multiple reverberations are the main degrading mechanism, something that is also shown in the equivalent B-mode images in Fig. 3.13.

3.4 Discussion

For bright targets at a depth of 40 mm, the PSF analysis performed showed that while taking both average dB values for all three regions of the PSF as well as the shape of the PSF in consideration, phase aberration had a greater impact in image quality.

For an imaging scenario where calibrated tissue is present, described in section 3.3.3, the role of reverberation is much more prominent especially at depths shallower than 5 cm, as shown by the trend of the CNR values for anechoic lesions at multiple depths.

In conclusion, reverberation clutter significantly degrades ultrasound imaging in the scattering environment of the human brain compared to phase aberration especially at depths shallower than 5 cm. The results suggest that clutter reduction methods, such as harmonic imaging, or spatial coherence imaging, may contribute significantly to image quality improvements for large 2D arrays in brain imaging.

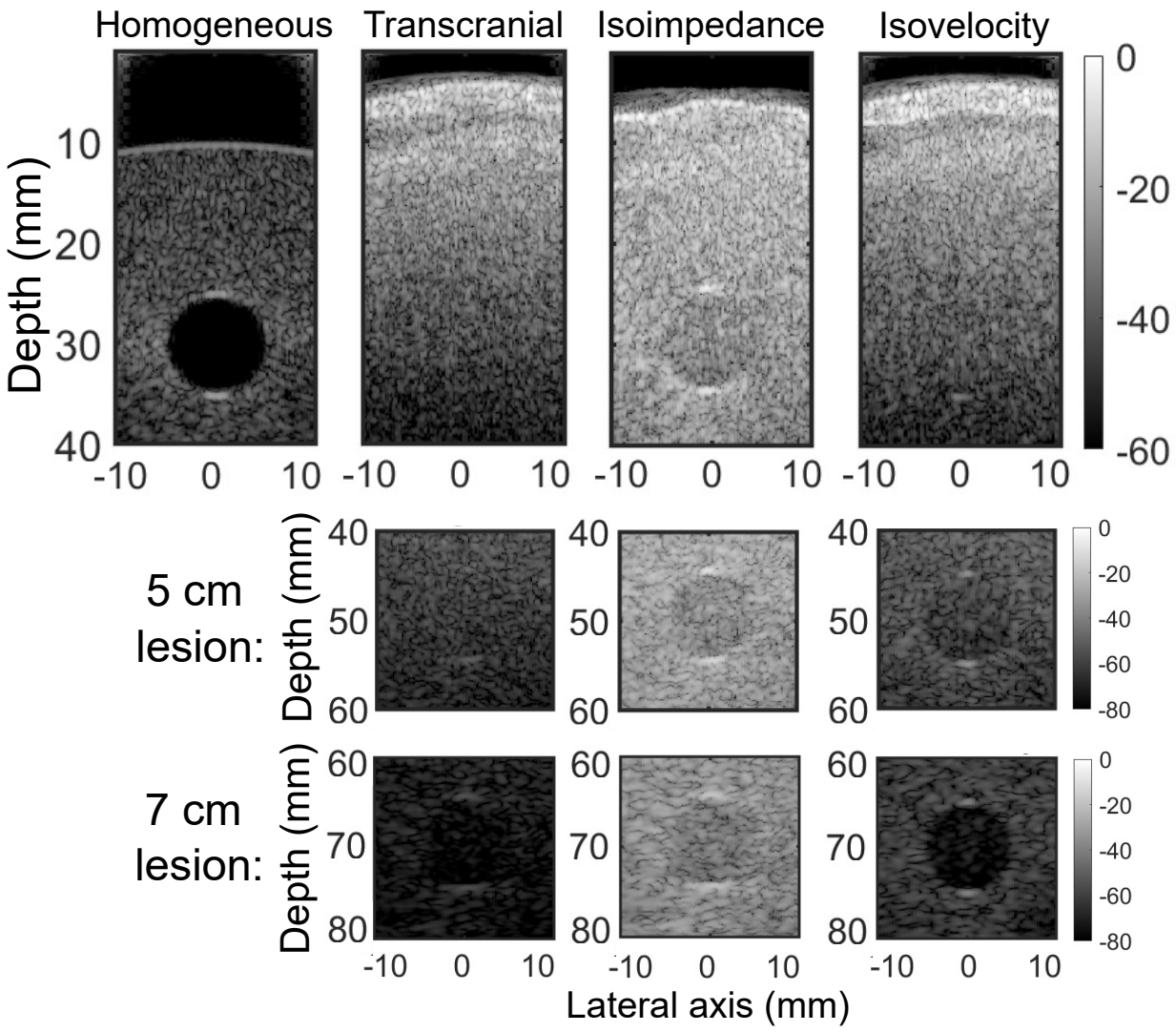

Figure 3.13: Anechoic lesions with a 1 cm diameter at different shown at different imaging depths for each row (3, 5 and 7 cm) and for a different imaging scenarios for each column, namely from left to right, for a homogeneous medium, transcranially, transcranially but with the effects of multiple reverberations removed and transcranially but with phase aberration removed.

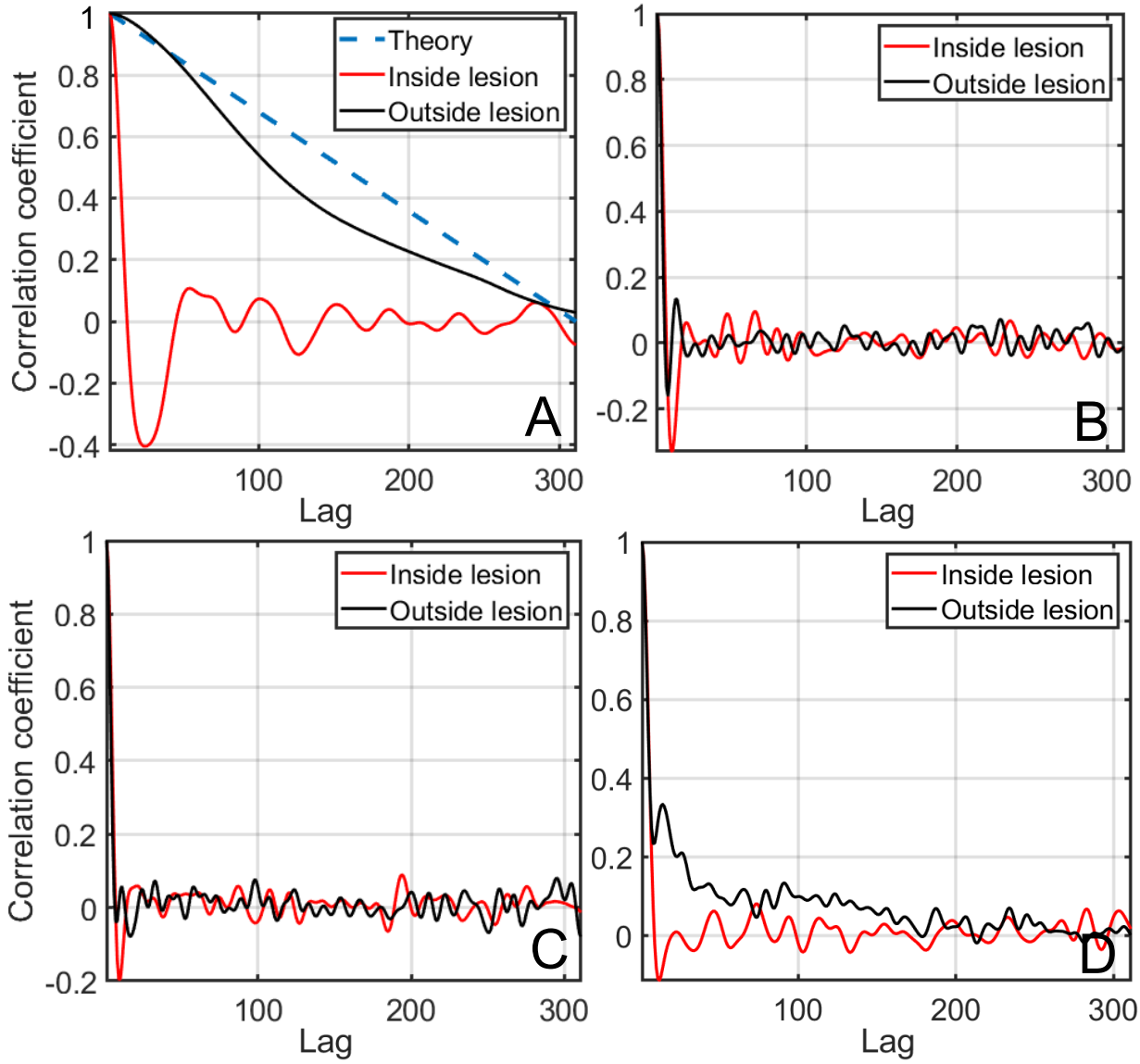

Figure 3.14: A, coherence curves for a homogeneous emission inside and outside the anechoic lesion. Theoretical curve for the ideal case is also shown as reference. B, coherence curves for a transcranial emission, C with the effects of phase aberration removed (isovelocity) and D with the effects of reverberation removed inside and outside the anechoic lesions. All plots generated from lesions at a depth of 3 cm.

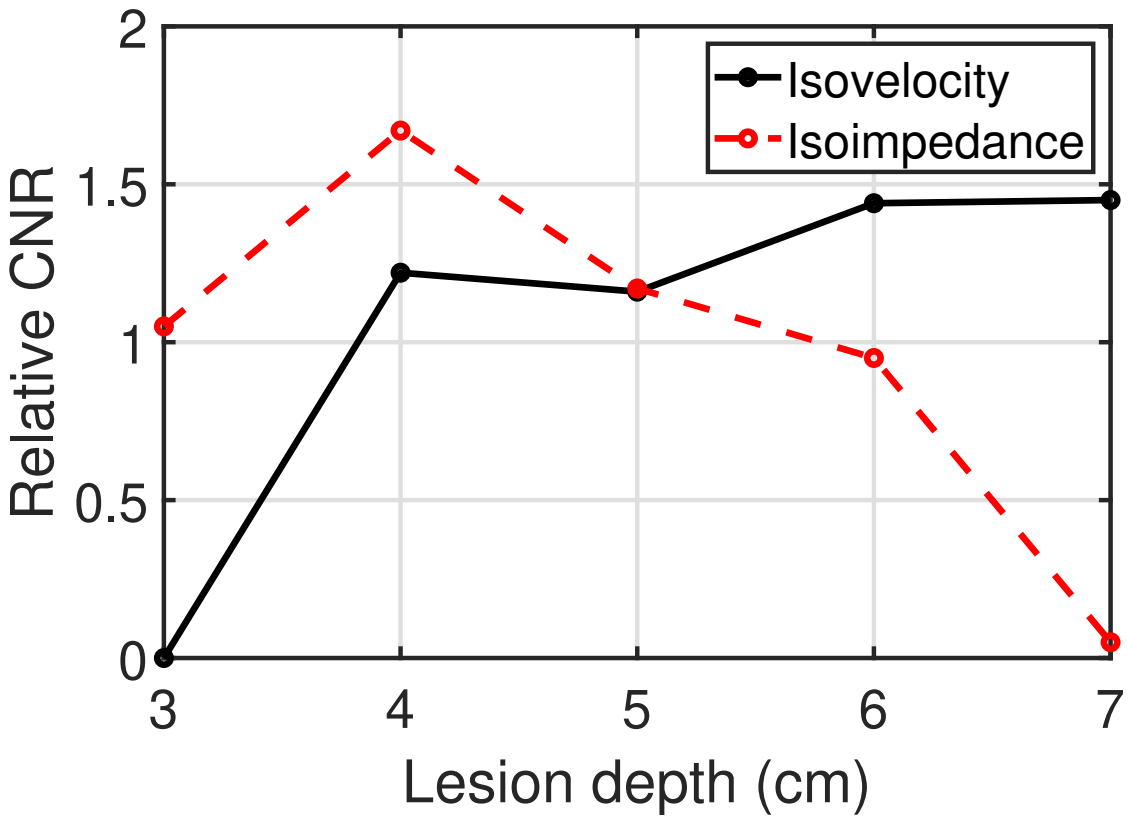

Figure 3.15: Trend of CNR values for the isoimpedance and isovelocity cases as a function of imaging depth.

CHAPTER 4

DIAGNOSTIC ULTRASOUND IMAGING OF THE LUNG: A SIMULATION APPROACH BASED ON PROPAGATION AND REVERBERATION IN THE HUMAN BODY

Even though ultrasound cannot penetrate a tissue/air interface, it images the lung with high diagnostic accuracy. Lung ultrasound imaging relies on the interpretation of ”artifacts” that arise from the complex reverberation physics occurring at the lung surface but appearing deep inside the lung. This physics is more complex and less understood than conventional B-mode imaging where the signal directly reflected by the target is used to generate an image. Here, to establish a more direct relationship between the underlying acoustics and lung imaging, simulations are used. They model ultrasound propagation and reverberation in the human abdomen and at the tissue/air interfaces of the lung in a way that allows for direct measurements of acoustic pressure inside the human body and various anatomical structures, something that is not feasible clinically or experimentally. It is shown that the B-mode images beamformed from these acoustical simulations reproduce primary clinical features used in diagnostic lung imaging, i.e. A-lines and B-lines with a clear relationship to known underlying anatomical structures. Both oblique and parasagittal views are successfully modeled, with the latter producing the characteristic ”bat sign” arising from the ribs and intercostal part of pleura. These simulations also establish a quantitative link between the percentage of fluid in exudative regions and the appearance of B-lines, suggesting that B-mode may be used as a quantitative imaging modality.

4.1 Introduction

The standard modalities that diagnose and monitor lung disease are X-ray imaging and computed tomography (CT) due to their extensive diagnostic capabilities [200, 4]. Ultrasound may not be normally thought of as a primary lung imaging modality. However, in the hands of an expert user it has a sensitivity and specificity ranging from 90% to 100% relative to CT for disorders that include pleural effusions, lung consolidation, pneumothorax, and interstitial syndrome [82]. Since ultrasound cannot penetrate the soft-

tissue/air interface, lung ultrasound relies on the interpretation of imaging ”artifacts” that appear to come from deep inside the air space of the lung, but are actually complex reverberations from the pleural interface [66]. This indirect imaging and clinical interpretation approach is fundamentally different from soft tissue imaging, where echos come directly from the structures being imaged. Despite the counter-intuitive aspect of imaging an air-filled organ using ultrasound, lung ultrasonography (LUS) has been an invaluable tool in assessing lung-related conditions.

In recent years, LUS has been preferred over physical examination or traditional chest radiography as the means to assess pulmonary congestion, a common finding in patients with heart failure [102], due to its high sensitivity and quantitative capabilities [107]. Pulmonary ultrasound strongly agreed with specific CT findings when analyzed by both lung- and lobe-specific location among a diverse population of mechanically ventilated patients with acute respiratory failure [182]. Diagnostics of pulmonary congestion with LUS can assess the presence of extravascular lung water [127]. Identifying a decrease in lung air content with LUS can also serve as an indicator of silent pulmonary edema or pulmonary fibrosis [56]. The use of LUS has recently had a significant impact on the study of the effects of COVID-19 on the human respiratory system, to stratify as well as monitor patient disease progression [105, 125]. LUS can be characterized as an essential intensive care modality due to its broad availability and low cost [16, 6, 101].

LUS is heavily based on the visual observation and interpretation of visual artifacts appearing in clinical B-mode images, namely A-lines (also known as horizontal artifacts) and B-lines (also known as vertical artifacts) [42]. A-lines represent reverberation artifacts and appear as horizontal, parallel lines that are equidistant and characteristic to the healthy lung and pneumothorax [82]. B-Lines are defined as discrete laser-like vertical hyperechoic reverberation artifacts which arise from the pleural line, eradicate A-lines without fading and they move synchronously with lung sliding [197]. These artifacts are related to a loss of subpleural lung aeration due to interstitial disease or lung deflation [168]. B-lines appear in a variety of lung diseases, such as cardiogenic pulmonary edema [155], lung contusions [170], acute respiratory distress syndrome (ARDS) [193], pneumonia [197], and in pulmonary fibrosis [158], however they alone cannot differentiate the cause [168]. With the mentioned image artifacts (A-lines, B-lines) or anatomical images (lung consolidations, pleural effusions), LUS provides significant information that can be integrated with the clinical signs and symptoms of the critically ill patient [193].

A variety of probes can be used in LUS. The possibility of detecting B-lines with different transducers is one of the advantages of the method [57]. Linear probes with a frequency range of 5–12 MHz are used

to obtain high resolution images when deep penetration is not required. Microconvex probes offer a wide viewing angle. Frequencies at this range are ideal for imaging superficial structures like the pleura [76]. The lung and pleural structures are assessed using B-mode, or brightness mode imaging, whereas M-mode imaging is used to assess and monitor movement of visceral pleura [194]. The ultrasonic probe can be positioned both longitudinally - perpendicular to the ribs, or obliquely along the intercostal spaces of the patient. When imaging longitudinally, or also referred to as parasagittally, a so-called bat sign commonly indicates the upper and lower ribs followed by a parallel the pleural line [82]. Even though the ribs limit the acoustic window, "lung sliding" sign on real-time LUS is typically imaged using longitudinal scanning [78, 197]. Its presence has a high negative predictive value for the diagnosis of a pneumothorax [78, 197, 191, 81]. In the oblique view a wider portion of the pleural line is imaged without interruptions from the rib structures [57, 110, 169].

According to Soldati et al. [168], separate B-lines (also called septal rockets or B1 in the other sources), which indicate distended interlobular or intralobular septa, can be divided into two subgroups, depending on presence or absence of modulation recognizable in B-mode image. Vertical reverberation artifacts, which are thickened laterally and fuse together to form coalescent B-lines (also called glass rockets or B2) represent peripheral lung ground glass opacities seen in high resolution computed tomography [114, 168]. An evenly white echographic lung field without horizontal reverberation may be described as a white lung artifact and is related to the condition of the subpleural lung parenchyma, preceding consolidation. Furthermore, additional classification criteria have been proposed for B-lines of nodular origin and columnar B-Lines (both are pseudo B-Lines) and short vertical artifacts, showing rapid fading [168]. Despite a significant variety of B-lines' appearance, from a clinical point of view, they can be classified as related to cardiogenic or pneumogenic conditions [24]. Compared to conventional ultrasound imaging, where the ballistic ultrasound signal represents a direct reflection of the underlying anatomy, LUS imaging is more complex because the sound does not come directly from the target. Rather it is sound that has bounced off of the pleura and reverberated multiple times in structures in the lung or in the thoracic layer [164, 17, 60, 36].

Many technical investigations of ultrasound imaging and quantitative ultrasound assessment of lung disease rely on methods that leverage the complex reverberation physics in the lung. Spectroscopic imaging relies on the hypothesis that B-lines arise from multiple reflections. Results obtained on lung mimicking phantoms have demonstrated the possibility that imaging of bubbly structures can be enhanced when insonicating at the resonant B-line frequency [171, 38]. The influence of the imaging frequency on visualization of B-lines has been demonstrated in both *in vitro* and *in vivo* studies [104, 35, 103]. Ultrasound multiple-scattering

characterization has been used to measure a diffusion constant of the medium by characterizing the impulse response of the system and, although this is not an imaging technique, it offers the possibility of relating the complex scattering physics to quantitative metrics for different regions of the lung [109]. Ultrasound simulations have also been performed to investigate the relation between wavelength, domain geometry, and the B-lines using bubble distributions placed in an otherwise homogeneous background [126].

Accurate qualitative and quantitative evaluation of lungs with ultrasound imaging would have a significant impact on our ability to understand, monitor, and treat lung disease. If obtainable, such measurements would generate accurate relationships between the local pleural and alveolar state, e.g. fluid percentage, from B-modes or from specifically designed lung ultrasound beamformers. However, understanding the relationship between acoustic propagation and diagnostic ultrasound B-mode images in the lung has been a persistently difficult challenge [37]. An improved understanding of the fundamental acoustics at the complex soft-tissue/air interface would enable the rational design of ultrasound imaging sequences that would be more clearly sensitive to disease.

Our previous studies based on combining *in vivo* measurements with our custom simulation tool (Full-wave) have generated highly realistic ultrasound images based on the first principles of propagation in anatomically accurate maps of the human body. By describing wave propagation directly from first principles, effects such as multiple scattering, reverberation, nonlinearity, and distributed aberration, which we have shown to be determining factors of ultrasound image quality [153], can be modeled. Their use in modeling ultrasound propagation in the body has been exhaustively validated experimentally in a wide variety of scenarios, including *ex vivo* abdominal measurements, water tank measurements, *in vivo* human abdominal measurements, intercostally, transcranially for brain therapy, and in the brain for therapy and traumatic brain injury [129, 153, 146, 31, 147, 149, 154, 137, 48, 187, 14, 140, 142, 18].

Here we develop simulations of the lung tissue and air interfaces with fine control over the underlying lung pathology, which would not be possible experimentally or *in vivo*. The key advantage is that these simulations can directly measure the pressure inside the human body, which gives us an insight into the physical interactions occurring at the tissue/air interface which cannot be observed clinically. Additionally, *in silico* we are able to obtain reference images that characterize normal and pathological cases, relying on the known and controlled anatomy, which is also impossible at a clinical setting. In a clinical, or even experimental setting, it is very challenging to fill an alveolus with fluid in a controlled manner. The broad range of acoustical interaction with the body wall and lung is modeled based on the fundamental principles

of propagation and interaction with the human anatomy to generate the key diagnostic features of LUS, i.e. A-lines and B-lines, and their relationship to disease. It is shown that these imaging scenarios can be modeled both transabdominally and transcostally using anatomically accurate human body walls. A model of alveolar structures is presented and it is shown how different levels of fluid within the alveoli, a critical indicator of lung health, modify the resulting ultrasound B-mode images.

4.2 Methods

Detailed speed of sound, density, attenuation and nonlinearity 2D maps serve as an input representing the heterogeneous acoustical properties of the human body [140]. The acoustic maps of the abdominal wall, as described in previous work, were derived from optical data from The National Library of Medicine's Visible Human data set [176]. Each component of the segmented visible female database images is assigned a tabulated value of density and sound speed, namely fat properties will differ to those of lean muscle, connective tissue and bone. All simulations in this work are performed in a 2D field. First, the simulation was calibrated to experimentally match the reverberation estimates in a porcine wall phantom. A piece of fresh porcine abdomen with the same thickness as the human data was placed within a water-tank to measure the reverberation ringdown, a metric for reverberation clutter. The B-mode images corresponding to the simulated and experimental data, as well as the reverberation curves, are shown in Fig. 4.1. This calibration method has been described in detail in recent work [174]. The numerical solver used in our simulations, Fullwave2, which is an higher order version of the previously developed tool Fullwave [150], is also extensively described in recent work [148].

Speckle brightness values in the simulation were also validated experimentally by placing fresh porcine liver under the body wall and it was found that the difference between experimental and simulated speckle brightness differed by less than 2 dB as a function of depth.

Air filled regions were represented in the simulations by areas of zero pressure values in the initial condition map to accurately model reflections between the tissue/air interfaces. The original optical Visible Human dataset has a resolution of 330 μm, however the simulation grid is finer, thus 25.7 μm diameter scatterers were generated in random spatial arrangement and amplitude and added to the acoustic maps to accurately model the acoustical scattering properties in tissue. The scatterer density was set at 20 scatterers per resolution cell. The resolution cell size was calculated for the fundamental frequency of 5 MHz and focal

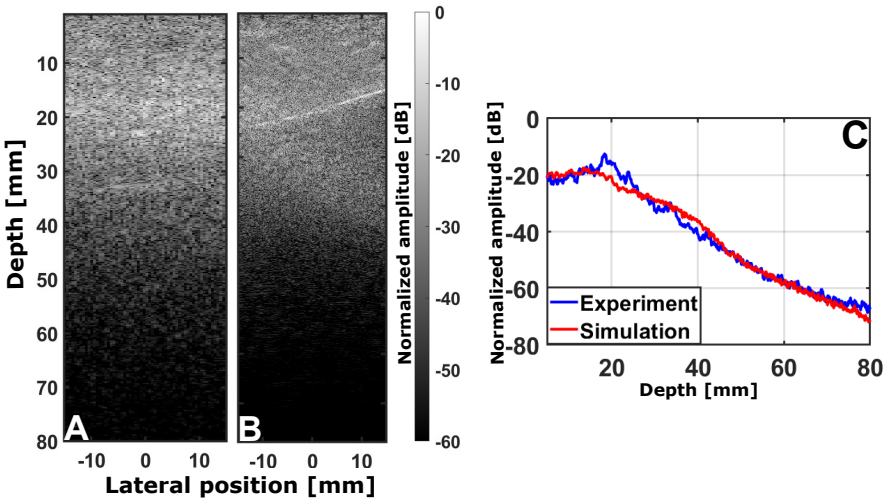

Figure 4.1: A, experimental B-mode image using a C5-2v transducer through porcine abdominal tissue. B, equivalent simulation B-mode generated by Fullwave. C, reverberation curves for experiment and simulation.

depth of 1.9 cm and 3 cm aperture. The scatterers had an average impedance mismatch of 5% relative to the background tissue. Following the guidelines for Point-of-Care LUS, both common imaging settings are modeled: oblique lung scanning, to provide good visualization of the pleural line, as well as parasagittal scans including the ribs. While the normal interstitial lung structures are of subwavelength lateral dimension [199], straight (in oblique view) and concave (in parasagittal view) tissue/air interfaces were introduced to model the native lung areas. To simulate the fascia and both pleural layers, a 0.4 mm thick connective tissue layer was added to the acoustic map at a depth of 1.9 cm. Air-filled structures were added directly under this layer.

Exudative subpleural lesions were modeled as bell-shaped structures composed of water and a staggered grid arrangement of air bubbles. Macrostructurally, the bell-shaped form was inspired by the shape of a secondary pulmonary lobule, which is the smallest unit of lung structure insulated by connective tissue septa [199]. Different lesions of lateral size ranging from 2x5 to 10x5 mm were simulated. The severity of the modeled exudation could be altered by changing size and shape (circle and ellipse) of the air bubbles (Fig. 4.2).

The simulations presented here are 2D, whereas the real air inclusions in affected lung are 3D objects. Volume indices, which are related to clinical assessments, were calculated in 2D as an equivalent volumetric fluid portion (EVFP) in an affected region (Table 4.1).

The centers of the described air bubbles are arranged both laterally and axially taking into account an average alveolar size [118] and assuming a decrease in axial layer-to-layer distance due to the lung deaeration

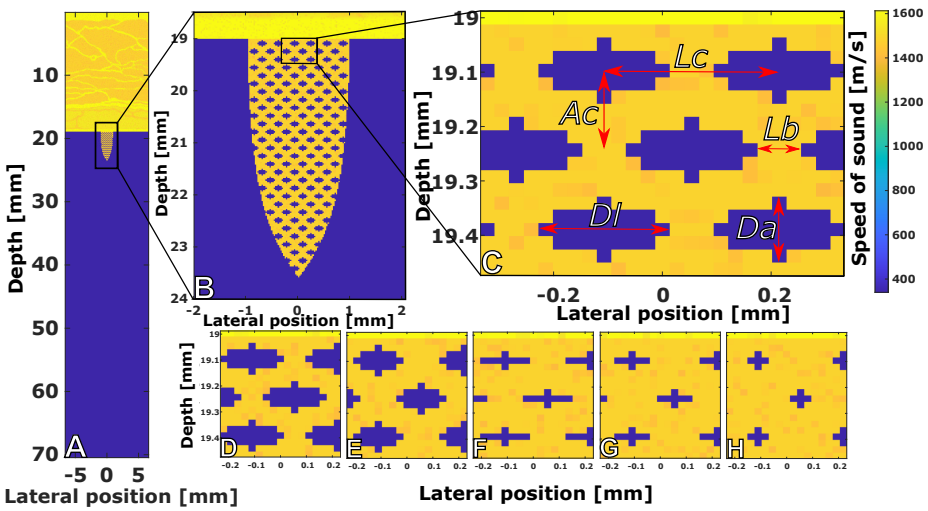

Figure 4.2: Speed of sound map fitted to the final B-mode image size (A) with its magnified version (B) to show the bell-shaped synthetic structure used to model a localized subpleural exudative lung lesion. (C) shows the same image at a higher magnification demonstrating the air bubbles arrangement and size pointers related to Table 4.1. Illustration of the air bubbles' shapes corresponding to the different fluid portions in an affected region: 0.18 (D), 0.55 (E), 0.71 (F), 0.88 (G) and 0.98 (H).

Table 4.1: Bubbles geometry and size description in different modeled lesions. Major (lateral) size (Dl), minor (axial) size (Da), lateral border-to-border distance (Lb) and equivalent volumetric fluid portion (EVFP) in an affected region

Shape of the air bubbles	Dl (μm)	Da (μm)	Lb (μm)	EVFP
Ellipse	206	102	102	0.18
Ellipse	154	102	154	0.55
Ellipse	154	51	154	0.71
Ellipse	102	51	206	0.88
Circle	51	51	257	0.98

and consolidation. This average bubbles' center-to-center distance was constant for all the simulations and set to 308 μm laterally (Lc) and 154 μm axially (Ac). Lateral distance between bubbles' borders (Lb), which corresponds to the single acoustic channel entrance, depends on the lateral size of the bubbles (Table 4.1). Each next (deeper) row of the bubbles is shifted laterally by a half of lateral distance between bubbles' centers (Lc/2). Due to the fineness of the actual alveolar walls (thickness within 2-10 μm) even at a fine spatial element size of 25.7 μm, the interstitial lung component has to be ignored.

In a clinical setting, scanning is bound to capture both affected and unaffected lung regions simultaneously, which in turn can alter an object's brightness on a B-mode image due to the amplitude normalization. Specifically, the co-existence of a normal bright pleural line and B-lines has an impact on the displayed

brightness of the latter. Additionally, in all of the presented simulations, the lesions containing water were surrounded by air, which corresponded to unaffected lung regions allegedly completely separated from the lesion by interlobular septa. That is consistent with the already mentioned approximation of the native lung tissue as a flat tissue/air interface.

The imaging configuration was performed in a range that is consistent with clinical lung ultrasound standards and recommendations [197, 43, 110, 169]. We used a 5 MHz phased array transducer emitting a 2.5 cycle, 0.1 MPa pulse focused at 19 mm, without an f number restriction. The ultrasound imaging sequence comprised 128, 256 and 320 independent transmit-receive events for simulations of oblique views, wide subpleural exudative lesion and parasagittal views with ribs, respectively.

For each event the transducer was shifted laterally by a beamwidth calculated as 205 μm. This shift is the equivalent of a walking aperture scheme. The simulation field was 30 mm wide and 70.5 mm deep in oblique views and 85 mm deep in parasagittal views. The time duration was adjusted to obtain a recommended penetration depth of 4-8 cm starting from the pleural line [43]. To achieve maximal energy deposition locally, the focal depth was set at the pleural line level (19 mm). The spatial step size was set to 25.7 μm, calculated relative to the 5 MHz transmit fundamental frequency. The temporal step size was set to 8.3 ns (simulations without bone components) and 4.2 ns (simulations with bone components) for a reference speed of 1540 m/s, which corresponds to a Courant-Friedrichs-Lewy condition of 0.5 and 0.25, respectively.

The generated RF data were beamformed using a conventional delay-and-sum algorithm. The received signals were sampled at a rate of 120 MHz. No filtering or interpolation were used, except for time gain compensation (TGC) with an exponential depth/time dependent gain based on attenuation coefficient 0.5 dB/cm/MHz assuming the tissue sound speed of 1540 m/s. All image processing was done in Matlab (Mathworks, Natick, MA, USA). The simulations were performed on a Linux Fedora 25 (v.4.10.13-200.fc25.x86 64) system running Intel Xeon® E5-2630 v4 Processors at 2.20 GHz, using the custom Fullwave simulation tool. Each full B-mode shown, comprises 128 individual simulated transmit/receive events, each of which requires 1.4 mins including beamforming. All 128 processes run in parallel.

4.3 Results

In the simplest simulation configuration, either soft-tissue or an air-filled region were placed under the human abdominal wall. The simulation of the B-mode image of a wave propagating through the

human abdomen and in a homogeneous medium is shown in Fig. 4.3A, and the equivalent sound speed map in Fig. 4.3B. B-mode images with reverberation artifacts characteristic for native lung (A-lines) and corresponding speed of sound map are shown in Fig. 4.3C and D, respectively.

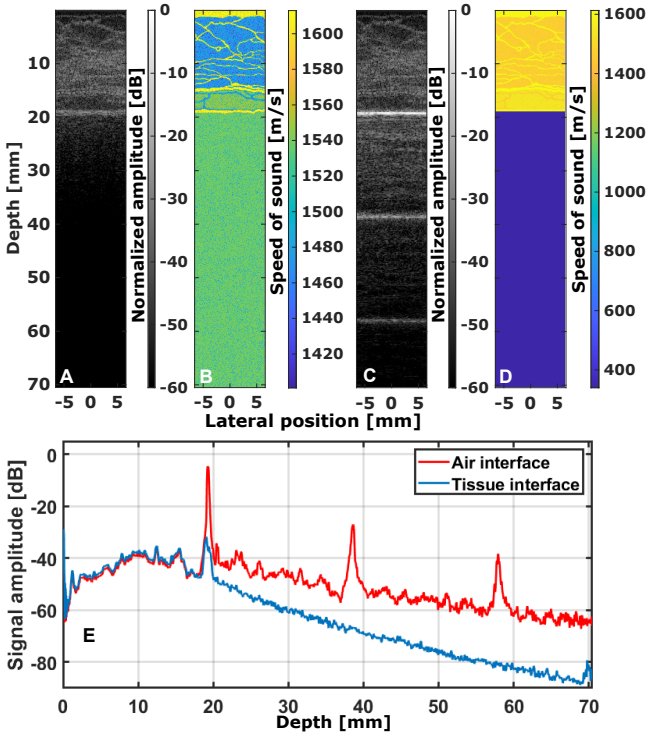

Figure 4.3: Ultrasound images simulated from an emission through the abdominal wall with different underlying materials: medium of soft tissue properties, B-mode image (A) and corresponding sound speed map (B); underlying straight tissue/air interface mimics pleural line, B-mode image (C). Note horizontal artifacts, A-lines *in silico*. D. Corresponding illustrative sound speed map. E. Curves of acoustic pressure averaged laterally for both cases. Three spikes correspond to hyperechoic pleural line (1st) and A-lines of fading brightness (2nd and 3rd).

In Fig. 4.3C, as we would expect in a normal human body scan, subcutaneous tissues were identified until approximately 19 mm of depth, followed by a hyperechoic horizontal line which is called the pleural line and corresponds to the interface between the pleura and the aerated lung tissue. The pleural line constitutes the brightest part of the image due to near complete reflection of the beam at the aerated lung interface. To facilitate the visual assessment of the modeled pleural line hyperechoicity, brightness of the both images (A and C) was normalized to the maximal level of the straight tissue/air interface image (Fig. 4.3C). Hyperechoic horizontal lines below the pleural line, regularly spaced at multiples of the distance between the probe and the pleural line, known as A-lines, are demonstrated. These reverberation artifacts are generated because of the strong reflectivity of the pleural line, with each ultrasound beam travelling several times between the probe

and pleura [60]. Gradual clarity degradation and progressive decrease of A-lines brightness with time-depth increase is observed as a natural result of ultrasound attenuation in soft tissue between the transducer and tissue/air interface (Fig. 4.3C). In Fig. 4.3E, the reverberation curves for images A and C are shown in blue and red respectively. In this plot it can be easily appreciated that the lines are mirror-images appearing at a constant interval of 19 mm (which is the distance of the transducer to the pleural line), as well as their loss of amplitude due to attenuation.

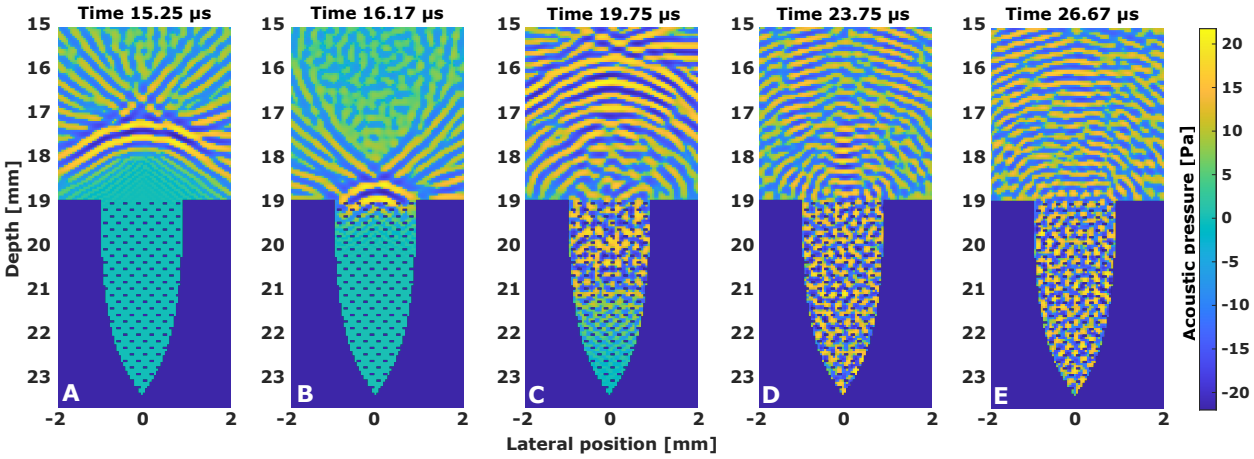

Figure 4.4: Illustration of the pulse propagation and multiple scattering in affected lung region at 5 elected moments in time. Acoustic pressure field (scale is compressed to emphasize small amplitudes). Air elements made visible for illustration purposes, note no sound propagation in the air. A. Ballistic pulse before hitting the lung surface, note trailing clutter. B. The wave is reflected from native lung areas and entering the affected lung region. C. The reflected wave travels back to the transducer, progressive wave propagation and multiple scattering occur in affected lung region. D. Continued backscattering, waves gradually leave the trap. E. Attenuation of the trapped wave, low intensity wave release is persisting.

To model simultaneous scanning of affected and intact lung areas, the regions mimicking exudative lesions mentioned in section II were centered laterally, placed axially at focal depth (19 mm) and surrounded by straight tissue/air interfaces. The affected region comprises acoustic channels of fluid surrounding staggered air bubbles. The air bubbles equate to the aerated part of the alveoli. This system of multiple air bubbles placed inside a fluid-filled area constitutes an acoustic trap, where multiple scattering and recurring reflections occur alongside the delayed gradual release of waves back to the transducer.

Supplementary file MM1.avi: Propagation of sound in areas of reduced aeration. The pressure field is shown on a compressed scale to facilitate visualization of the low pressure signal.

The propagation of sound in the areas of reduced aeration can be visualized as the acoustic pressure changes (Supplementary video 1). Due to the significant dynamic range, the pressure field is shown on a compressed scale to facilitate visualization of the low pressure signal along with the ballistic pulse. In addition, the simulated acoustic field snapshots combined with air elements are provided as separate frames at selected times in Fig. 4.4. These frames show the ballistic pulse before its interaction with the air elements (Fig. 4.4A) and the very moment of its entering the region of the acoustic channels (Fig. 4.4B). Fig. 4.4C-E demonstrate progressive sound propagation with multiple scattering, followed by the back propagation of the wave out of the trap. In the flat tissue/air interface, which models unaffected lung region and surrounds acoustic trap, only reflection is observed. Moving forward in time and comparing the pressure intensity, the sound attenuation can also be appreciated in Fig. 4.4 and Supplementary video 1.

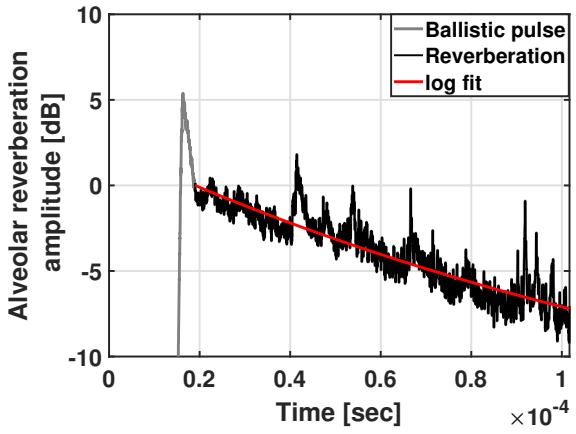

Figure 4.5: Ballistic pulse (gray) and subsequent reverberation signals (black) originating from the acoustic trap and measured at its entrance. In red, the fitted exponential on the reverberation curve.

To observe the aforementioned phenomena in time more clearly, Fig. 4.5 shows the signal amplitude, laterally averaged along the trap aperture, as a function of time. Initially, the ballistic pulse signal is observed, followed by decreasing signals originating from the trap. If these data would be interpreted by fitting, it could be observed that it follows an exponential decay, with a decay constant of 6187 s^{-1}, corresponding to an estimated characteristic length of 24.89 cm. Each simulation runs independently. Quantitatively, the reverberation time constant measured in the trap corresponds to 161 μs. This constant is long, relative to a single transmit event, typically around 100 μs. However, it is small compared to typically clinical frame-rates of 30 ms.

The link between fluid portion in the synthetic lesion and vertical reverberation artifacts appearance in B-mode images was observed. The minimal equivalent volumetric fluid portion necessary for generation of

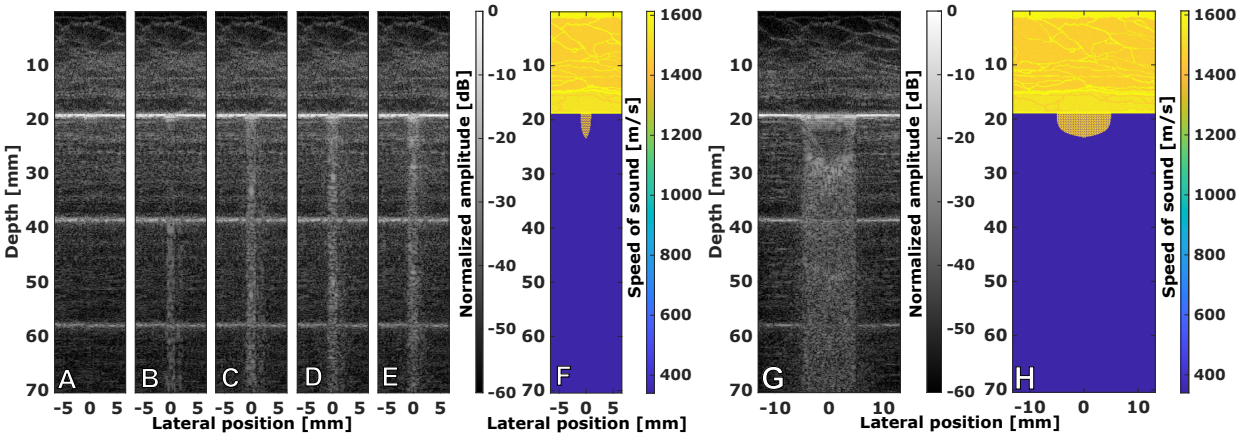

Figure 4.6: B-mode images showing step wise increase of EVFP in the affected area by: 0.18 (A), 0.55 (B), 0.71 (C), 0.88 (D) and 0.98 (E). Time gain compensation is applied. Note the interrupted vertical line in (B) that demonstrates fusion of bright elements only beneath the first A line. (F) Speed of sound map used to produce image (C) shown as an example, fitted to the final B-mode image size. (G) shows simulated B-mode image of one cm wide subpleural exudative lesion. EVFP in the affected area equals 0.88. Time gain compensation applied. (H) Speed of sound map fitted to the final B-mode image size.

tiny vertical artifact connected to pleural line, was 0.18 (Fig. 4.6A). In this case the artifact has length not more than 1 mm and is not a line per se, however can be seen and is connected to the pleural line. Technically, a vertical artifact can be categorized as a B-line when it starts and fuses into the pleural line, and without interruption persists throughout the image. In Fig. 4.6C-E, the generated B-lines extend from the pleural line and run perpendicularly to the existing A-lines throughout the entire image axially. At the same time, the interrupted vertical line in Fig. 4.6B would not be considered as actual B-line, due to the fact that there is no fusion at the pleural line. The gradual elongation and fusion of these vertical artifacts occur with an increase in the volume fraction of liquid in the order of 0.71. For fluid volumes lower than this threshold we hypothesize that the B-line does not fully form as a result of trapped wave's inability to leave the acoustic trap earlier than the second horizontal reverberation event (Supplementary video 1) due to the significant axial size of the air bubbles (Da) with the same both lateral size (Dl) and border-to-border distance (Lb) (Table 4.1). Supplementary video 1 clearly demonstrates slower pulse propagation in the trap of lower fluid part (marked as EVFP 0.55) as compared with lesion of higher fluid part (marked as EVFP 0.98). Another characteristic of the presence of B-lines is the cancellation of A-lines in proximity to the affected area. In our cases it can be clearly observed only within the vertical artifact borders. This can be explained by the abrupt changes in tissue acoustical properties between the affected and unaffected regions, which is more gradual in

a real affected lung. At the same time, gradual blurring and lateral population of the B-lines, phenomena characteristic to ground glass opacities were observed. This effect may be explained by more significant dispersion of directional angles of waves released from the acoustic trap back to the transducer due to the relatively larger acoustic channels' aperture. However, the amount of acoustical energy entering the trap remains the same, which in turn leads to decrease of its density. Finally, these B-mode images alongside with the corresponding speed of sound maps clearly show a link between the locations of acoustic traps and the vertical artifacts (Fig. 4.6F). Since our simulation tool enables complete control on the medium, which is represented by physical maps, it was possible to model larger exudative lesion shown in Fig. 4.6G. This image demonstrates lateral expansion of the coalescent B-line proportional to the extension of the input map (Fig. 4.6H) and blurring of the vertical artifact increasing with depth that can be observed in clinical LUS.

To provide us with a metric of B-line detectability, we utilize contrast-to-noise ratio (CNR) measurements, using the definition proposed by Patterson and Foster [123]:

$$CNR = \frac{S_i - S_o}{\sqrt{(\sigma_i^2 + \sigma_o^2)}} \tag{4.1}$$

where S_i and S_o are the spatial means of the image inside and outside the ROI, respectively, and σ_i and σ_o are the standard deviations of the image inside and outside the ROI, respectively. The areas where the measurements were performed are depicted in Fig. 4.7A.

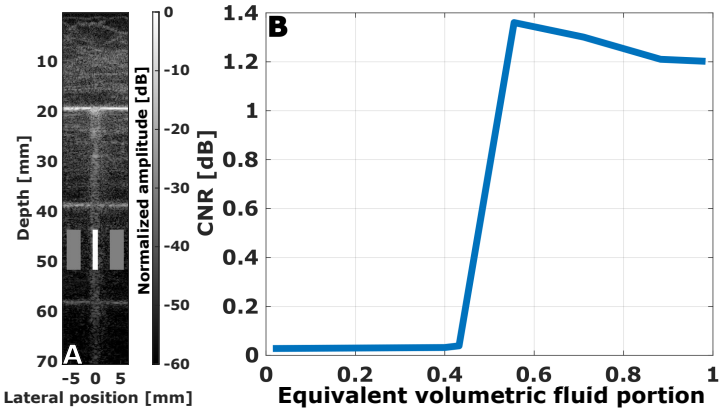

Figure 4.7: Contrast-to-noise ratio measurement technique and results. (A) B-mode image illustrating the location of the samples: white central bar shows a region of interest (signal), gray ones - background regions (for comparison). No time gain compensation. (B) Plot CNR versus equivalent volumetric fluid portion in the affected region of the lung.

The centers of the CNR sampling regions are arbitrarily located at a depth of 47.5 mm. Two background samples, each three times larger than the ROI, at the same depth, are compared.

The CNR of the lines as a function of fluid volume portion plot in Fig. 4.7B shows clear dependence of the vertical artifact detectability on the degree of exudation. A detectability threshold of 0.55 can be observed for a CNR value of 1.36 dB. The peak value of CNR at point is linked to the interrupted vertical line and its subsequent slight decline in cases of continuous B-lines can be explained by two factors. First, the release of relatively high energy waves back to the transducer in this particular case took place later (deeper in terms of the B-mode image) as seen in Fig. 4.4B and is related to conservation of the pulse energy after its first entrance into the trap without release of the waves back to the transducer (Supplementary video 1). Back-scattering from the trap in the short-time constants when the resonant cavity has not-yet reached a steady-state may be more absorptive than emissive. Second, with the increase of the fluid portion, B-lines become blurred and get laterally populated almost to the image borders that decreases contrast of their central parts.

As discussed in section II, we also simulated a parasagittal views, which clinically would include visible portions of the ribs. For this case we used the same visible human maps, segmented at a slice where the ribs are present, and set the sound speed, density and attenuation coefficient of the structures to match that of bone. The used sound speed maps are shown in Fig. 4.8B and D. In Fig. 4.8B, a simple concave tissue/air interface is modeled whereas in image D an exudative lesion, similar to the one in Fig. 4.6D was included. The resulting B-mode images are shown in Fig. 4.8A and C. Fig. 4.8A resembles a typical intercostal image of the healthy lung, showcasing the characteristic bat sign, where the wave is strongly reflected by the high speed bone edges. Fig. 4.8C also presents a B-line in the likeness of those we observed in exudative lesions simulated in oblique view.

4.4 Discussion & Conclusions

Simulations of ultrasound propagation in the abdominal wall and reflections from simple models of tissue/air interfaces of the lung can be used to model the reverberation physics responsible for the generation of key clinical diagnostic parameters. These simulations produce A-lines and B-lines similar to those of a clinical scanner at this frequency. These imaging features can be observed in both common views, longitudinal and oblique. A synthetic alveolar structure, which could be partially filled with fluid in a controlled manner,

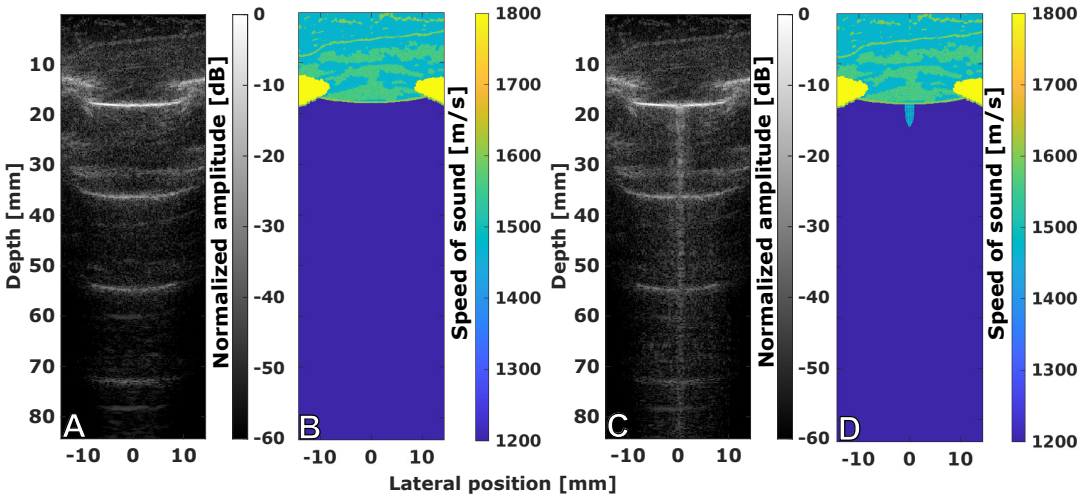

Figure 4.8: Simulated parasagittal (longitudinal) views with ribs. Note the ”bat sign” which identifies the upper and lower ribs with their acoustic shadows (the wings of the bat) and, a little deeper, the pleural line (the back of the bat). A. Tissue/air interface of concave shape mimics unaffected lung. A-lines *in silico*. B. Corresponding speed of sound map. C. Coalescent B-line *in silico*. Time gain compensation applied. D. Full and zoomed speed of sound maps. Acoustic trap simulates subpleural exudative lesion of size 2x5 mm. Volume portion of fluid in the affected area equals 0.88.

was introduced to model an acoustical trap at the body wall/lung interface. The complex reverberation physics arising from this simple soft tissue/air bell-shaped structure successfully trapped sound and then almost continuously re-emitted for the duration of the imaging sequence. Even though a single transmit-receive event lasts 0.05 ms the reverberation constant measured at alveolar surface was 0.16 ms. This persistence, results in the appearance of B-lines in the B-mode image at the location of the acoustic trap and below it and establishes that our simulation tool models the relevant reverberation physics from alveolar-like structures to reproduce clinical indicators of lung imaging. A limitation of the current work is that the alveolar model is synthetic. The alevolar structure, including air pocket size and distribution, can be derived from anatomical measurements, such as histology maps, to improve the realism.

The percentage of fluid in the alveolar structures was modified to reflect different disease states of the lung and thus to quantitatively link features of ultrasound imaging (B-line and A-line characteristics) to the underlying tissue morphology. The advantage of simulation approaches is that the underlying tissue structure is fully known and can be controlled while all other aspects related to imaging remain exactly constant. The percentage of fluid in the alveolar structure was gradually varied for a range of fluid fractions from 18 to 98%. There is a clear correlation between B-line detectability and brightness. B-line detectability was

established at a threshold of 55% fluid fraction present in the alveoli. This is broadly consistent with clinical observation where B-lines also appear in conjunction with fluid [82]. The specific threshold at which B-line detectability occurs may depend on the specific anatomical model, body wall thickness, alveolar size and shape distribution, as well as imaging parameters such as frequency, focal position, beamforming approach and others. Although this parameter space was not explored here, the simulation tool provides a direct basis for modeling it using propagation and reverberation physics. This provides a quantitative method to investigate the relationship between the lung properties and the received ultrasound field.

Furthermore, a simulation approach can be advantageous over experimental imaging in several respects. First, simulations provide control of the underlying lung morphology, air distribution, and abdominal properties, which is impossible to measure $in\ vivo$. Second, the pressure field can be measured throughout the simulation volume. We expect the ability to know the underlying acoustical maps and behavior will enable a more direct and physically realistic understanding of lung imaging and its diseased state. This approach can also enable the rational design and testing of lung-specific imaging or measurement methods. It can also be used to generate an anatomically detailed and tagged data sets for machine learning approaches where the cost functions can be tuned to be sensitive to the underlying tissue properties.

CHAPTER 5

ADAPTIVE MULTIFOCUS BEAMFORMING FOR CONTRAST-ENHANCED-SUPER-RESOLUTION ULTRASOUND IMAGING IN DEEP TISSUE

Contrast-enhanced-super-resolution ultrasound imaging, also referred to as ultrasound localization microscopy, can resolve vessels that are smaller than the diffraction limit and has recently been able to generate super resolved vascular images of shallow *in vivo* structures in small animals. To fully translate this technology to the clinic, it is advantageous to be able to detect microbubbles at deeper locations in tissue while maintaining a short acquisition time. Current implementations of this imaging method rely on plane wave imaging. This method has the advantage of maximizing the frame rate, which is important due to the large amount of frames required for super resolution processing. However, the wide planar beam used to illuminate the field of view produces poor contrast and low sensitivity bubble detection. Here, we propose an "adaptive multifocus" sequence, a new ultrasound imaging sequence that combines the high frame rate feature of a plane wave with the increased bubble detection sensitivity of a focused beam. This sequence simultaneously sonicates two or more foci with a single emission, hence retaining a high frame rate, yet achieving improved sensitivity to microbubbles. In the limit of one target, the beam reduces to a conventional focused transmission; and for an infinite number of targets, it converges to plane wave imaging. Numerical simulations, using the Fullwave code, are performed to compare the point spread function of the proposed sequence to that generated by the plane wave emission. Our numerical results predict an improvement of up to 15dB in the signal to noise ratio. *Ex vivo* experiments of a tissue-embedded microtube phantom are used to generate super resolved images and to compare the adaptive beamforming approach to plane wave imaging. These experimental results show that the adaptive multifocus sequence successfully detects 744 microbubble events at 60 mm, when they are undetectable by the plane wave sequence under the same imaging conditions. At a shallower depth of 44 mm, the proposed adaptive multifocus method detects 6.9 times more bubbles than plane wave imaging (1763 vs. 257 bubble events).

5.1 Introduction

The concept of contrast-enhanced-super-resolution (CESR) ultrasound imaging, also referred to as ultrasound localization microscopy, was first proposed in 2011 [26]. It can create images of microvessels at resolutions much smaller than the ultrasound diffraction limit [39, 120, 47]. This revolutionary technique was inspired by super localization microscopy in the optical imaging domain. Optical localization microscopy exploits the stochastic blinking of fluorescent sources and super-localizes the center of each source by virtue of its separability [12, 162]. Gas-filled encapsulated microbubble contrast agents, which typically have a mean diameter of less than 5 μm yet are highly echogenic, play the role of the fluorescent sources in ultrasound. Microbubble separability is also required in ultrasound super resolution imaging. To satisfy this requirement, the use of highly diluted contrast agents with conventional ultrasound scanners has been proposed [120, 19, 196, 3]. Using this strategy, super-resolved images of a mouse ear were demonstrated [19]. However, in these studies, techniques were only demonstrated on sparse vessel networks and conventional ultrasound scanners with low frame rates were used, which limits the acquisition time. In 2015, Errico et al. proposed a new method [47], which uses microbubbles at higher concentrations, to reconstruct detailed super-resolved images within far shorter and clinically relevant acquisition times (about 10 minutes). This technique relies on a spatiotemporal filter [34] to distinguish moving microbubbles from the surrounding tissue and static microbubble signals. Ultrafast acquisitions of thousand of frames [11] enabled by new software-based programmable ultrasound systems increase the number of bubble detection events while maintaining a clinically relevant time window. A contrast enhanced super resolution image can then be reconstructed by localizing the center of each separable microbubble, and accumulating their center positions from all the acquired images, as other super resolution imaging techniques do. In this study, 2D super-resolved vascular maps of rat brain slices were generated [47]. Following these studies, Lin *et al.* applied this technique with a mechanically scanned system to obtain 3D images of tumor-associated angiogenesis [83, 84].

The extraordinary ability of CESR imaging to image microvessels at a resolution of tens of microns can potentially improve ultrasound's applications to malignancy detection [55, 64], wound healing, and atherosclerotic vasa vasorum assessment. Compared with traditional multi-pulse contrast-enhanced imaging techniques like pulse inversion or amplitude modulation, or harmonic imaging techniques, CESR imaging no longer relies on the harmonic generation of microbbubles and no longer suffers from the tissue-generated harmonics during wave propagation [203]. Compared with other high resolution ultrasound imaging techniques,

such as Acoustic Angiography [59, 58, 165] which has been used to visualize microvascular angiogenesis patterns in small tumors, CESR imaging has some notable benefits: it can be performed with a standard array, rather than requiring a unique dual-frequency transducer; it can be performed at greater depths; it can resolve vessels as small as tens of microns rather than the ≈100 micron limit of Acoustic Angiography. Despite these benefits, CESR has some limitations such as the long acquisition time and poor sensitivity at depth, as well as the need for extensive post-processing. Detecting separable microbubbles in microvessels at depth is particularly challenging due to: 1) the low intensity of the signal backscattered from microbubbles; and 2) elevated microbubble destruction from high frame rate sonications. Because of the second challenge, the transmitted energy is limited in order to minimize microbubble destruction within the long imaging time, which compounds difficulties with the first challenge. Previous studies have proposed the use of larger microbubbles to increase the amplitude of the backscattered signals [85], however further improvements are needed to achieve super resolution at depths as great as 10 cm. To improve the potential clinical translation of this novel imaging approach to humans, the sensitivity of CESR imaging to contrast agents at depth in soft tissue is crucial.

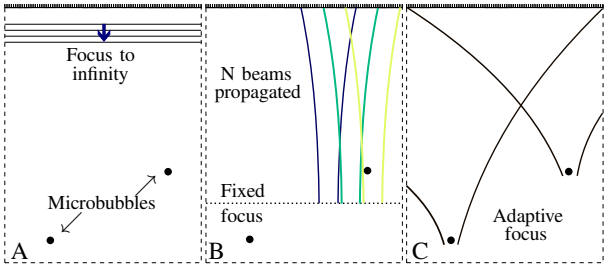

Figure 5.1: (A) Plane wave emission travelling along the vertical direction. (B) Conventional fixed focus sequence. Different colours mark different emissions. A total of 16 beams are propagated, 3 are shown here. (C) Adaptive multifocus sequence. An example emission is shown, with beams emitted following the direction of propagation.

Currently, plane wave sonications (see Fig. 5.1 **A**) can be used to acquire raw radio-frequency (RF) data at a very high frame rate. Theoretically, the achievable frame rate of a plane wave sequence is on the order of 10,000 frames per second, and it is only limited by the travel time needed for the wave to reach the microbubbles and return to the transducer. This maximum achievable frame rate is lowered by sequences that involve multiple transmit-receive events to generate an image, such as conventional focused imaging, and compounding, including plane wave compounding. Practically, for the application of contrast-enhanced-

super-resolution imaging, the frame rate is usually set to several hundreds frames per second, to avoid the rapid destruction of microbubbles from excessive sonication.

Here we propose an adaptive multifocus method that combines the advantages of the superior imaging quality of a focused transmission with the high frame rate of plane wave transmission, by focusing with one emission on multiple targets at the same time, to improve the imaging sensitivity and penetration depth. The objective of this article is to study the feasibility and quantify the improvement introduced by the adaptive multifocus sequence.

5.2 Methods

5.2.1 Adaptive Multi Focus Sequence

Three imaging methods, plane wave, conventional fixed focus, and the proposed adaptive multifocus imaging are implemented in the numerical and experimental parts of this study. Fig. 5.1 illustrates the different transmission strategies for plane wave imaging, conventional fixed focus imaging and adaptive multifocus imaging, respectively.

The proposed adaptive multifocus ultrasound sequence simultaneously focuses on several microvessel locations with a single emission. These multi-focus acquisitions are acquired at a high frame rate to obtain the large number of frames required by super resolution imaging. Furthermore these focal positions can adaptively target different regions in the imaging plane, specifically these target locations correspond to the microbubbles that exist in a single frame. As the bubble distribution changes due to vascular flow or destruction, the regions of imaging interest are adaptively re-targeted with a new multifocal emission. Since each transmit event consists of a single emission, the frame rate of this method is only limited by the travel time, just like plane wave imaging. Similar approaches have been considered in fast cardiac imaging, such as multi-line transmit [95, 183, 184].

The proposed multifocal approach can be used adaptively by using a single low frame rate target identification sequence interleaved with hundreds of high frame-rate multi-focal sequences. This first conventional fixed focus sequence is used to establish the regions of interest which contain microbubble signals from microvascular flow. Although this sequence has a low frame rate due to the conventional limits of focally interrogating the whole image plane, it exhibits a high bubble sensitivity due to its focused nature. Bubbles are localized in the targeting image, as explained in section II-E. These bubble positions are then

used to generate a transmit profile that focuses on each target simultaneously. Interleaving both sequences results in a high frame rate imaging method that adaptively targets bubbles that appear within the imaging frame and excludes regions where there are no bubbles or no vessels. This adaptive targeting approach takes advantage of conventional focused imaging, which remains the single most effective tool to improving sensitivity for ultrasound imaging at depth in the human body.

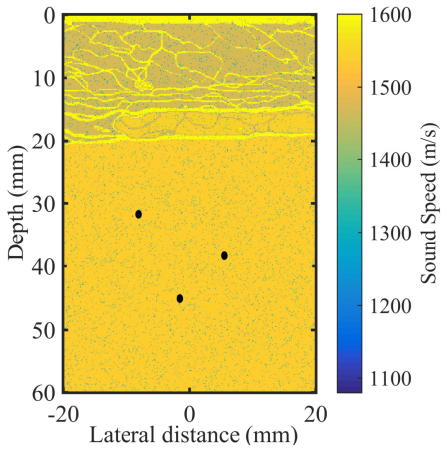

Figure 5.2: Sound speed map of an abdominal human model. The three black spots represent the point targets artificially added to mimic microbubbles. Note that the size is exaggerated for visualization purposes. The real diameter was one pixel.

Here, the fixed focus imaging sequence comprises 16 transmit beams focused at a constant depth (60 mm) but laterally shifted using a sub-aperture at the emission consistent with an F-number of 4. The entire transducer surface was used as the receive aperture. The lateral focus position was chosen equally spaced in a way that there is no overlap between each reconstructed zone. Fig. 5.1**B** illustrates the fixed focus transmit beams (note that only three transmit beams are shown for clarity). The raw data acquired from each transmitted beam was used to generate eight A-lines with a parallel beamforming method that uses a conventional delay-and-sum algorithm. After stitching the reconstructed zones from all the 16 transmitted beams generated, a B-mode image with $16 \times 8 = 128$ A-lines was generated. In this manner, the fixed focus sequence produced B-mode images within the same field of view generated by the plane wave and adaptive beamforming methods. Although the fixed focus method has a lower frame rate, it has a higher sensitivity to microbubble detection that arises from the well established contrast and signal to noise ratio (SNR) advantages of conventional focused imaging.

For rapid processing, the data acquired by the focused imaging sequence were beamformed on a comparatively coarse grid (4 points per wavelength). Then a spatio-temporal singular value decomposition

(SVD) filter [34] was used to remove the surrounding tissue and to generate a first estimate of the microbubble positions, which can then be used by the adaptive multifocus sequence to seed the initial target locations. A comprehensive description of the super-resolution processing is given in section II-E.

The adaptive multifocus method relies on the use of this first estimate of the microbubble position to create a single pulse with multiple focusing targets. For example, the simplest multifocal case consists of two bubbles located in the area of interest. Fig. 5.1**C** illustrates, in black, the beam that focuses on the two bubble targets. To determine this focal profile, an emission profile is designed based on two linearly super-imposed pulses with each focused on separate targets. Experimentally, the focal positions of the adaptive multifocus emission can be updated after a certain time when the microbubbles have moved or been destroyed, for example, after having acquired a few hundred images. When vessels within a target region have been mapped, that area can be tagged to avoid unnecessary re-targeting. This reduces the amount of redundant sonications which therefore decreases microbubble destruction. After the whole field of view is scanned, a complete CESR image can be obtained.

5.2.2 Simulation

The three ultrasound imaging sequences, plane wave, fixed focus, and adaptive multifocus imaging, were simulated using the Fullwave numerical solver [151]. This simulation tool is an acoustical numerical solver based on finite differences in the time domain. It models ultrasound propagation and imaging with high accuracy, and it can rapidly prototype the sequence development in 2D. The simulations were launched in two media. First in a homogeneous medium which mimics results that might be obtained in a water tank, and then in an abdominal numerical model, which constitutes a more realistic aberrating, reverberating and scattering environment as it would be observed *in vivo*. Fig. 5.2 shows the sound speed map of the abdominal model used in the simulation. This model has been obtained from photographic images of the female Visible Human data. This pictures were converted into a sound speed map using a number of image processing techniques to isolate different types of tissue, skin, fat, liver and connective tissue. Thus, tabulated sound speed values were assigned to the distinct types of tissue [46]. This model has been validated in Ref. [138, 139]. Randomly distributed scatterers, with a density of 20 scatterers per resolution cell, were added to the abdominal model to fully develop a speckle pattern. The sound speed of the scatterer was also set to be randomly distributed between 1460 m/s and 1540 m/s. In the same way that the sound speed maps were created, maps that represents the density and attenuation were also generated.

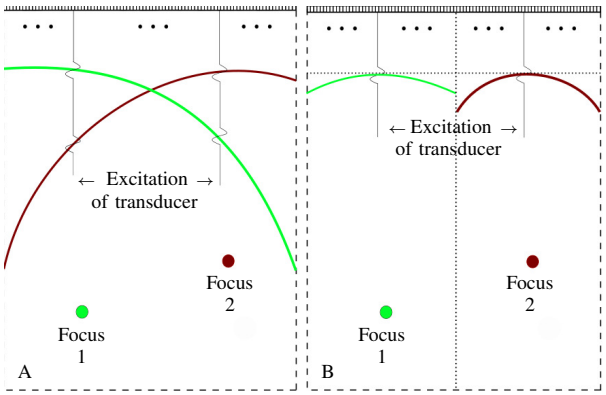

Figure 5.3: Theoretical (A) vs. experimentally realizable (B) focal profiles. Note that (B) represents a hardware, not a fundamental limitation. Different phase profiles and their respective foci are color coded with respect to the two foci. Lines marked as "excitation of transducer" are repeated throughout the length of the array.

Three point targets were positioned in different areas of both the homogeneous medium and a human abdominal model. These point targets were used to generate three point spread functions (PSFs). These targets are illustrated with black points in Fig. 5.2 (note that the actual point size is much smaller) along with the speed of sound map of the human abdominal model. The size of the simulation field was 60 mm deep and 40 mm wide, which is clinically relevant for humans and realizable with the commercially available transducer (ATL Philips L7-4, WA, USA) used subsequently in the experimental section. The transmit sequences were simulated at 5.2 MHz with a pulse duration of 1.5 cycles. The space discretization was set to 12 points per wavelength and a Courant-Friedrichs-Levi condition of 0.4 was used to define the temporal sampling in the simulation. These imaging simulations were performed with transmit-receive configurations corresponding to the three respective imaging sequences. They also match the imaging experiments performed subsequently.

These three imaging techniques are compared in terms of the full width at half max (FWHM) of the main lobe, the amplitude of the side lobes, the SNR and the size of the PSF at the three target positions. The SNR was measured from the root mean square of the signal in a small region that contains each target and was divided by the root mean square of a same sized region at the same depth but shifted laterally. The size of the PSF was measured as the area with an intensity above -50 dB.

5.2.3 Experimental implementation of the adaptive multifocus sequence

The adaptive multifocus technique uses simultaneous multi-pulse emissions to focus energy on two or more targets (Fig. 5.3**A**). From the point of view of the transducer array, the relative phase between the

emitted pulses changes, depending on the element. To implement this experimentally, a Verasonics Vantage research ultrasound scanner (Verasonics Inc., Redmond, WA, USA) was used. This scanner allows for the implementation of multi-pulse sequences. However, technical limits in the maximum delay between the pulses to approximately 4 μs (1024 internal clock periods) restrict the implementation of the multi-pulse emission to nearby targets or to small apertures. A second technical challenge is that the scanner does not allow for a sufficiently versatile design of the emitted pulse for cases where the delay between the pulses is smaller than the period of the pulse and where a summation of the pulses is necessary. Note that these technical limitations do not represent fundamental constraints of the method. In light of these constraints, a simplified emission was implemented as illustrated in Fig. 5.3**B**. The aperture was split into two, with each half of the transducer focusing on one target. It is likely that greater sensitivity could be achieved with a full aperture.

5.2.4 Ex vivo experiment

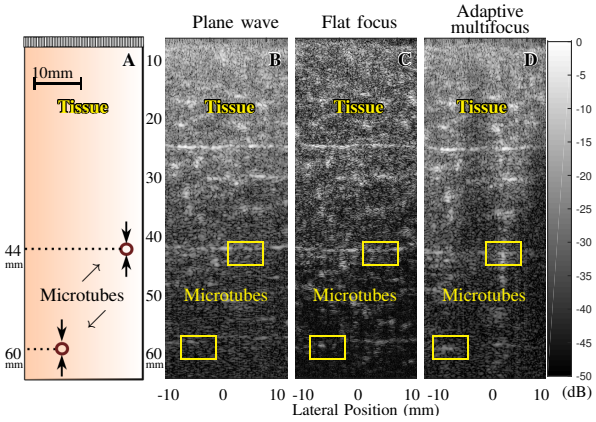

Figure 5.4: (A) Schematic of the porcine tissue phantom with two embedded microtubes.(B-D) B-mode images for the three imaging techniques. The dynamic range for all the B mode images is 50 dB.

To evaluate the effect of the proposed multifocus adaptive beamforming technique, *ex vivo* experiments were conducted with porcine muscle tissue embedded in a 5% gelatin phantom. Two thin-walled microtubes (Paradigm Optics Inc., WA, USA) with an inner diameter of 105 μm were embedded in the porcine tissue at depths of 44 mm and 60 mm. Note that these tubes were below the axial resolution of the imaging system otherwise. Lipid-encapsulated microbubble contrast agents containing decafluorobutane (SynQuest Labs, Alachua, FL, USA) were prepared as described in the reference [51]. The contrast agents were pumped through the microtubes, with the aid of an infusion pump (Harvard Apparatus, Holliston, Mass) at a steady

infusion rate of 25 μL/min. The tube established flow in the direction perpendicular to the imaging plane. The microbubble contrast agents had a polydisperse size distribution with a mean diameter of 0.9 μm and a concentration of 1×10^{10} bubbles per milliliter. They were diluted to a concentration of 1×10^{8} bubbles per milliliter. Imaging was performed with an ATL-Philips L7-4 linear probe (WA, USA). The transmit frequency of 5.2 MHz was chosen due to the imaging depth to be tested. If deeper tissue needs to be imaged, a lower frequency should be used to counteract the attenuation. After steady flow was established, plane wave imaging, fixed focus imaging and adaptive multifocus imaging were performed successively, without any flow interruptions. Fixed focus imaging used 16 focused beams with a fixed focal depth at 60 mm. Adaptive multifocus imaging used one beam with two simultaneous targeting foci at the locations determined by the fixed focus imaging (Fig. 5.3**B**). For all three techniques, a beam repetition rate of 700 Hz was used, resulting in a frame rate of 700 Hz for both plane wave imaging and adaptive multifocus imaging and a frame rate of 43.85 Hz for fixed focus imaging. Within the same amount of time, plane wave and adaptive multifocus methods acquired 5000 frames, while fixed focus method acquired 312 frames.

5.2.5 Contrast enhanced super resolution imaging

Fig. 5.4 shows the schematic of the tissue phantom and the resulting experimental B-mode images from the three techniques. These B-mode images were generated using a conventional delay-and-sum beamforming method. To determine the bubble location from the B-mode images, the stationary component of the image must be filtered out. Consequently, an SVD filter was applied to the acquired frames to detect the moving microbubbles [34]. This spatio-temporal filter is tuned to remove low frequency components and to preserve fast changing pixels where bubbles are localized. To determine the optimal cut-off of the SVD filter, a sweep in the cut-off values was performed. An optimal filter is the one that maximizes the number of detected bubbles, i.e. true positives. This cut off was found to be 2 out of 250. The SNR was computed as the mean signal amplitude at the microbbuble location divided by the mean amplitude of the background noise in a region at the same depth, and expressed in dB scale.

Each microbubble center was localized from all the frames of the SVD filtered images by cross-correlating with a simulated point spread function (PSF). The simulated PSF was generated with the same settings as the *ex vivo* experiments. Cross-correlation only measures the similarity between the reference and subsequent images, therefore to filter out noise, a threshold was applied. Here the threshold for microbubble detection was set to a cross-correlation coefficient of 0.7.

The final super resolution images were reconstructed by accumulating all the microbubble centers. Within the fixed acquisition time, 5000 frames were acquired for plane wave imaging and adaptive multifocus imaging, while only 312 frames were acquired for fixed focus imaging.This maintains an equal number of transmit-receive events because fixed focus imaging has a frame rate that is 16 times slower. Therefore, only the super resolution images reconstructed from the same number of frames are shown to generate a fair comparison. The super resolved images were compared by measuring the size of the tube as the full width at half max (FWHM), and by measuring the number of detected bubbles.

5.3 Results

5.3.1 Simulations

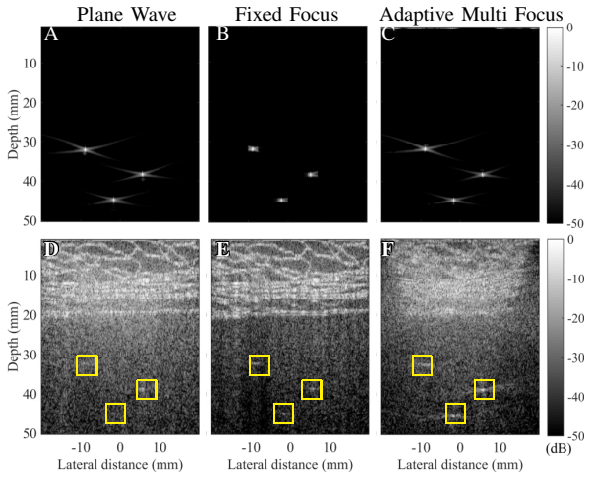

Figure 5.5: Simulation results in a homogeneous medium (A, B, C) and in a human abdominal model (D, E, F). A and D show the B-mode images from the plane wave emission. B and E show the B-mode images from 16 transmit receive events with a focal depth of 38.5 mm. C and F show the B-mode images using a simultaneous triple targeting focus at the bubble location (note that this consists of a single emission).

Table 5.1: Comparison of point spread functions for plane wave, fixed focus and multifocus imaging.

	Plane wave	Fixed focus	Multifocus
FWHM (μm)	397	365	361
Side lobe (dB)	-12.2	-12.3	-12.4
Area of PSFs (mm^2)	81.6	16.0	73.8

Fig. 5.5 shows the simulated B-mode images for the homogeneous medium (A-C) and for the abdominal model (D-F). In the homogeneous medium case, the PSF generated from the simulation has similar values

Table 5.2: Signal to noise ratio in dB

	Plane wave	Fixed focus	Multifocus	Delta
Target 1	2.69	5.92	6.28	3.59
Target 2	8.23	7.30	15.84	7.61
Target 3	1.72	8.77	12.60	10.88

for both the FWHM of the main lobe, which has an average value of 374 μm, and the side lobe, which is approximately -12.3 dB, for all three sequences. The side lobe level was measured by extracting the horizontal intensity profile at the maximum of the main lobe for each PSF. These measurements are summarized in Table 5.1. The relative similarity between these metrics is driven by the fact that there is no background ultrasound signal corrupting the point spread functions. The distinguishing feature between these three homogeneous sequences occurs in the size of the PSF, which was measured as the area with intensity above -50 dB. The PSF areas of the plane wave and of the Adaptive multifocus sequences are very similar with values of 81.6 and 73.8 mm^2, respectively. However the fixed focus has a much smaller PSF area of 16 mm^2, suggesting that it is less sensitive to off-axis clutter. The area of the respective PSFs are also summarized in Table 5.1. The PSF area for plane wave and multifocus imaging methods suggests that their clutter artifacts and resolutions in the B-mode images are approximately equivalent in this homogeneous case.

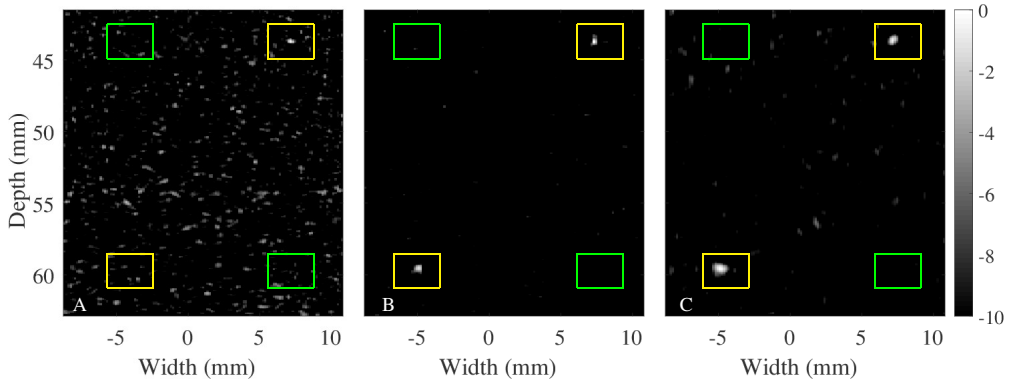

Figure 5.6: SVD filtered image for plane wave imaging (A), fixed focus imaging (B) and adaptive multifocus imaging (C). The dynamic range of all these images was 10 dB. Contrast to tissue ratio was calculated from the tube region (yellow box) and the surrounding tissue region (green box) at the same depth.

However, *in vivo* there are several sources of image degradation, such as reverberation clutter, trailing clutter, aberration etc. [135]. In fact, the point targets in the abdominal model are undetectable or almost undetectable (Fig. 5.5**D**) with the plane wave imaging sequence. This is because the echoes from the point targets are weak compared to reverberation clutter, off-axis clutter and other degrading effects from the

heterogeneous acoustical maps. The fixed focus sequence, on the other hand, clearly detects the three point targets (Fig. 5.5**E**). This is due to focusing, which deposits energy locally, in the neighborhood of the targets, compared to the plane wave sequence. This also demonstrates why a fixed focus sequence is preferable for the initialization of the regions of interest for the subsequent application of the adaptive multifocus sequence. Fig. 5.5**F** shows the B-mode image generated from the propagation of the adaptive multifocus beam with three focal regions, one targeting each of the point scatterers. Here the three point targets are clearly visible with a higher contrast than the fixed focus sequence. This is due to a combination of two factors. First, a variable focal depth is used in the adaptive multifocus case instead of a fixed focal depth. Second, the whole aperture is used to focus energy on the point targets, while in the fixed focus case only a partial aperture was used to focus on each lateral position. A supplementary movie shows the propagation of the wave front for the multifocus sequence, a single multi-pulse emission focused at three target simultaneously. Table II summarizes the measurements of the SNR for the three targets and for the three sequences. Most notably, compared to the plane wave image, the adaptive multifocus technique improves the point target intensity by 3 dB to 11 dB.

5.3.2 Ex vivo experiment

Table 5.3: Comparison of SNR from SVD filtered images for Plane waving imaging, fixed focus imaging and multifocus imaging.

	Plane wave	Fixed focus	Multifocus
Frame rate	700 Hz	43.85 Hz	700 Hz
Shallow microtube (44 mm)	1.9±1.6 dB	5.2±2.0 dB	5.6±3.2 dB
Deep microtube (60 mm)	0.2±1.2 dB	2.2±1.8 dB	4.4±3.2 dB

Fig. 5.4 A. shows a schematic representation of the tissue phantom and the resulting experimental B-mode images from the three imaging methods. The shallow microtube is clearly visible for the focused and adaptive multifocus imaging. In the plane wave imaging case, it is visible but near the limit of detectability . However, the deep microtube is only visible with the fixed focus and adaptive multifocus technique. Because of the attenuation of the tissue, the SNR decreases with depth, which in turn decreases the signal level from the deepest bubble to be lower than the noise floor. Fig. 5.6 shows one SVD filtered image from each technique. The yellow boxes outline the microbubble locations. On the displayed images (Fig. 5.6), the plane wave sonication detects only the shallow microtube, with a SNR of 2.8 dB for the shallow microbubble and a SNR

of 0.4 dB for the deep microbubble. The fixed focus sequence detects both bubbles, with a SNR of 3.8 dB and 5.5 dB, respectively, demonstrating experimentally that fixed focus can be used as a first estimate of the bubbles location for the adaptive multifocus technique. The adaptive multifocus method also successfully detects both microbubbles, with a SNR of 4.9 dB and 7.2 dB, respectively. From Fig. 5.6 we can see that, for the plane wave method, the bubbles are detected with an intensity comparable to the noise, which leads to false bubble detection. However for the fixed focus and adaptive multifocus methods, the bubble signals are significantly higher than the noise floor.

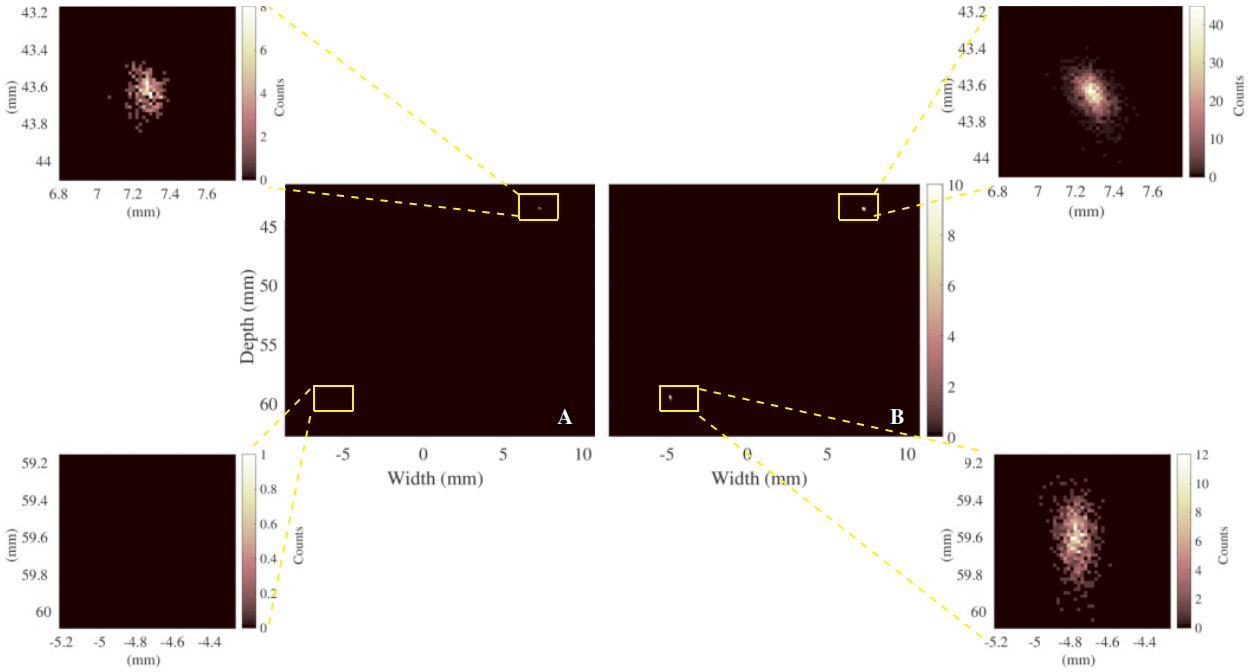

Figure 5.7: Super resolution image reconstructed from plane wave imaging (A) and adaptive multifocus imaging (B). The image intensity is the number of detected microbubble events. The dynamic range is 50 counts. Detected tubes are also shown enlarged. The dynamic range on zoomed images was 200 counts.

The average and standard deviation of the SNR values were also computed from 5000 frames that were SVD filtered. The results are summarized in Table 5.3. The standard deviation is expressed as an error notation. For the shallow tube located at a depth of 44 mm, the adaptive multifocus technique provides an average SNR improvement of 3.7 dB and 0.4 dB, compared with plane wave imaging and fixed focus imaging, respectively. For the deep tube located at 60 mm, the average SNR improvement is 4.2 dB and 2.2 dB, respectively. Note that the plane wave sequence produces a standard deviation higher than the average SNR for the deeper microtube. This indicates that no bubbles are detectable at this depth using plane wave imaging.

Table 5.4: Comparison of estimated microtube sizes for plane wave and multifocus imaging.

		Plane wave	Adaptive multifocus
Shallow tube	Axial size	160μm	144μm
	Lateral size	98μm	98μm
Deep tube	Axial size	N.d.	214μm
	Lateral size	N.d.	110μm

Figure 5.7 shows the super resolution images for plane wave imaging sequence (A) and adaptive multifocus sequence (B). The reconstructed tubes are magnified for clearer visualization. The shallow tube was successfully detected by both techniques. However, the tube reconstructed from adaptive multifocus imaging has a higher brightness than the one from plane wave imaging. At the shallow depth (44 mm) the adaptive multifocus method detects 1763 bubble events whereas conventional plane wave imaging detects 257 bubble events. The deep tube at 60 mm depth was *only* successfully detected by adaptive multifocus imaging with a total number of bubble events detected of 744.

Axial and lateral profiles of the detected tubes are presented in Fig. **??**. The image-derived sizes of the 105 micron inner diameter micro-tubes were measured by the full width at half maximum and are summarized in Table 5.4. For the shallow microtube, the plane wave measured a lateral size of 98 μm and an axial size of 160 μm. While, the adaptive multifocus measured a lateral size of 98 μm and an axial size of 144 μm. Thus the diameter measurements from both techniques are comparable. Data for the deep microtube is only provided for the adaptive multifocus technique, since plane wave was not able to detect it. The lateral size of the bottom microtube was found to be 110 μm and the axial size was 214 μm.

5.4 Discussion and conclusion

The proposed adaptive multifocus technique substantially increases the sensitivity to bubble detection in deep tissue. Both images and measured SNR values clearly demonstrate that adaptive multifocus imaging provides better SNR than fixed focus imaging, while maintaining a high frame rate near that of plane wave imaging (over 16 fold faster frame rate than focused imaging). At the shallow depth (44 mm) the adaptive multifocus method detects 6.9 times more bubble events than the conventional plane wave imaging. Plane wave imaging does not provide sufficient sensitivity at 60 mm depth with the tested bubble concentration and attenuation conditions, whereas the proposed multifocus technique has the ability to detect and resolve the 105 micron tube with high SNR. However, since adaptive multifocus beamforming is a more sophisticated

technique, two of the challenges observed are the needed beamformer flexibility to achieve the multi-focus emission, and the processing time required to calculate the targeted adaptive focus profile. Here two simultaneous locations were targeted but the number of effective targets could vary. An increase in the number of targets would in all likelihood decrease the SNR gains. In the limit of an infinite number of target locations the adaptive multifocus emission would correspond exactly to a single plane wave emission. Therefore, for a finite number of targets, one would expect the gains to be within a range that is in between the two target and plane wave imaging scenarios. The optimal number of targets depends on several parameters, including the depth of the region of interest, the microbubble concentration, and whether the imaging environment is challenging (e.g. a homogeneous phantom vs. abdominal imaging). For example, for shallow imaging in homogeneous phantoms, a plane wave may be sufficient to resolve shallow structures, however imaging deep in abdominal tissue, a low number of targets would be required.

We expect that the adaptive multifocus technique will be interleaved with the fixed focus sequence. Due to its high sensitivity to microbubble detection, the fixed focus sequence would be used to generate, from low number of frames, pre-estimates of the position of the bubbles. Subsequently, these pre-estimated positions would be used to produce the beam profiles that the adaptive multifocus sequence will emit. Interleaving both sequences would allow for updating the focal positions of the adaptive multifocus sequence, and therefore it will increase the robustness of the bubble detection in case that dynamic changes of the bubbles occur, namely, new bubbles appearing or disappearing. Optimal parameters associated with the interleaving of these two sequences, such as the number of frames per sequence or the number of targets at the multifocus emission, will depend on vascular features of the region of interest, depth of the vessels, concentration, etc, which may motivate future studies.

The multi-angle plane wave compounding consists of multiple emissions to produce B-mode images, therefore the frame rate decreases depending on the number of angles used [111]. To maintain a fair basis for comparison, compounding was not considered in this study. Nevertheless plane wave compounding could be compared to an equivalently compounded multi-focus sequence in future studies.

Although, microtube size estimates from the super-resolution images were close to the known microtube diameter (see Table 5.4), the size in the axial direction was consistently larger that the lateral size. This may be due to ultrasonic interactions between the microtube wall and the microbubbles. However this observation is not inherent to the proposed multifocus technique, since it also occurs in plane wave imaging.

In clinical applications, we envision using super resolution imaging to assess microvascular density and morphology associated with various pathologies [83, 84]. For anatomical regions such as breast and prostate, this may require imaging at depths of 3-5 cm. For liver or cardiac applications, depths in the order of 10 cm are required. An additional challenge is that the accurate evaluation of microvasculature in a tissue volume requires 3-D imaging. Given that current plane wave super-resolution techniques require seconds or even minutes per 2-D slice, and tens of minutes to reconstruct even a small 3-D volume, technologies to maintain high frame rate imaging while retaining the image sensitivity at substantial tissue depths are needed.

Here technical implementation constraints limited the aperture size. This suggests that a full aperture implementation would improve the quality of the adaptive multifocus CESR images even further.

CHAPTER 6

SUPER-RESOLUTION IMAGING THROUGH THE HUMAN SKULL

High resolution transcranial ultrasound imaging in humans has been a persistent challenge for ultrasound due to the imaging degradation effects from aberration and reverberation. These mechanisms depend strongly on skull morphology and they have high variability across individuals. Here we demonstrate the feasibility of human transcranial super-resolution imaging using a geometrical focusing approach to efficiently concentrate energy at the region of interest, and a phase correction focusing approach that takes the skull morphology into account. It is shown that using the proposed focused super-resolution method, we can image a 208 μm microtube behind a human skull phantom in both an out-of-plane and an in-plane configuration. Individual phase correction profiles for the temporal region of the human skull were calculated and subsequently applied to transmit-receive a custom focused super-resolution imaging sequence through a human skull phantom, targeting the 208 μm diameter microtube, at 68.5 mm in depth and at 2.5MHz. Microbubble contrast agents were diluted to a concentration of $1.6 * 10^6$ bubbles/mL and perfused through the microtube. It is shown that by correcting for the skull aberration, the RF signal amplitude from the tube improved by a factor of 1.6 in the out-of-plane focused emission case. The lateral registration error of the tube's position, which in the uncorrected case was 990 μm, was reduced to as low as 50 μm in the corrected case as measured in the B-mode images. Sensitivity in microbubble detection for the phase corrected case increased by a factor of 1.48 in the out-of-plane imaging case, while in the in-plane target case it improved by a factor of 1.31 while achieving an axial registration correction from an initial 1885 μm error for the uncorrected emission, to a 284 μm error for the corrected counterpart. These findings suggest that super-resolution imaging may be used far more generally as a clinical imaging modality in the brain.

6.1 Introduction

The ability to detect and to image small vessels in the human brain is crucial especially in the context of neurodegenerative disorders such as Alzheimer's disease [44] and vascular dementia [172], as well as

the assessment of stroke-related pathologies [50]. To appropriately identify the presence of cortical or subcortical infarcts or other stroke lesions using imaging methods, high spatial resolution is required [61]. Three dimensional Computed Tomography Angiography (CTA), one of the gold-standard imaging methods of brain vessels, can reliably resolve structures down to 0.4 mm [190]. Magnetic Resonance Angiography (MRA) offers comparable resolution with an effective voxel size of 0.39 mm [63], while two dimensional Digital Subtraction Angiography (DSA) offers reconstruction down to a pixel size of 0.34 mm [177]. With venous vessel sizes in the brain measuring as small as a few micrometers [166], the importance of increasing the resolution of standard imaging methods is evident.

Super-resolution ultrasound imaging has shown great promise in the field of vascular imaging. Also referred to as Ultrasound Localization Microscopy (ULM) [47, 84] among other terms, this imaging technique has gained tremendous popularity during recent years, and has been used to generate microvascular maps that surpass the ultrasound diffraction limit, and can potentially produce images resolving vascular structures with diameters in the range of 8-19 μm laterally, thus providing a $\lambda/10$ resolution limit [47, 19].

Inspired by the use of fluorescent "blinking targets" in optical super-resolution methods, ULM in ultrasound uses gas-filled encapsulated microbubbles with a mean diameter on the order of a few microns as contrast agents that are injected in the blood flow. These microbubbles stochastically appear and disappear in the field of view [27, 167]. At sufficiently low concentrations, the appearing microbubbles can be spatiotemporally separated, allowing for their localization at a sub-wavelength level [84].

One of the challenges of ULM is the isolation of the microbubbles from the surrounding tissue in the background. To achieve microbubble separation, various filtering methods have been employed, such as high-pass spatiotemporal filters which can distinguish fast moving components from slow ones [47], temporal median filters to calculate the background [2], or threshold-based averaging filters [19] to remove background signals. Singular value decomposition (SVD) filters [33, 84] can also be used for the separation by exploiting the variation in the coherence length between microbubbles and tissue, which is especially useful when the bubbles and tissue are moving at the same velocity, i.e. in the case of a frequency overlap. Following the filtering process, microbubbles can be localized using centroid detection techniques [195], which are robust and computationally efficient.Alternatively, in recent work, cross-correlation algorithms have been used to localize microbubble appearances [49]. Other localization methods explored in literature include localizing either the onset of the microbubble backscatter signal or the first point at which the signal intensity has reached 50% of its maximum. [21].

Early work in super-resolution imaging by Viessmann *et al*. [195] showed that microtubes of a diameter of 216 μm can be resolved *in vitro* with a 2 MHz transmit frequency. Errico *et al*. [47], proposed the injection of microbubble contrast agents at a concentration of 2×10^8 bubbles/mL and the use of a plane-wave compounded ultrafast imaging sequence, allowing for the generation of a super-resolved image within a clinically reasonable duration (150 s). Using this method, they produced super-resolved images of a rat brain that showcased structures as small as 8 μm. Other studies have also verified the method's *in vivo* feasibility. Namely, Ackermann *et al*. [2] imaged tumor angiogenesis in a tumor-bearing mouse and estimated microbubble flow speeds within the vessels and Lin *et al*. ([83, 84]) produced super-resolved images of tumor angiogenesis with vessel sizes ranging from 5 to 150 μm. Even more recently, the method's potential for tumor diagnosis has been shown in a clinical setting [119].

Although its capabilities far surpass the resolution limits of conventional ultrasound, super-resolution imaging is not devoid of challenges, especially from a clinical perspective. Depth penetration is a challenge in the *in vivo* environment, mainly as a result of the drop-off in bubble detectability with imaging depth, which can be attributed to several mechanisms, including attenuation, reverberation, multiple scattering effects and off-axis clutter that significantly degrade the images. Compared to conventional imaging, these effects are compounded by the low amplitude of the emissions, which is used to avoid microbubble destruction. Even though this is not an issue in shallow regions of interest, e.g. when imaging around 2 cm of depth [19, 84], imaging at greater depths has also been demonstrated. In recent studies, 150 μm sized microtubes have been successfully resolved at a depth of 6 cm through abdominal body wall, in an *ex vivo* experiment using a multi-focus approach [49].

Another challenge lies in the fact that to satisfy the separability condition, which is a prerequisite for bubble isolation and localization, a low concentration of microbubbles is used. When combined with the low flow rate in vessels (especially capillary vessels which have a flow rate in the order of 2 μL/min [161]), this results in the need for the acquisition of a considerable number of frames (on the order of thousands) to fully populate a vessel [83, 120]. This, subsequently, results in prolonged acquisition times which poses a challenge not only for patient time management, but also for motion correction, which attempts to reduce artifacts caused by breathing or heart cycles [65]. Recent studies have, however, used higher contrast agent concentrations to increase the size of the region of interest imaged while maintaining a short acquisition time [10].

In the context of using ultrasound in the human brain, in imaging and in therapy, the biggest challenge is ultrasonic propagation through the skull. The heterogeneous nature of the human skull bone at a microscopic level, causes considerable distortion of the ultrasonic beam, in the form of resolution compromising reverberations, refraction [90], multiple scattering, reflection between bone and tissue interfaces and mode conversion, with the three latter being the main sources of attenuation [130], while absorption plays a secondary role at the higher frequencies used in imaging [128]. More specifically, the skull thickness, density and sound velocity tend to vary across the length of the transducer causing phase aberration of the wavefront. The combination of these factors results in a decrease in amplitude, as well as a three dimensional shift in the position of the target in the resulting image.

To overcome this persistent challenge, several phase aberration correction techniques, based on time reversal [181, 179], speckle brightness [116], pitch-catch methods ([88]), have been developed. A large number of phase correction techniques have been developed for transcranial focused ultrasound therapy. Focused ultrasound can thermally or mechanically destroy malignant brain tissue. This topic has been investigated for the last 6 decades and has seen a resurgence in the last 2 decades, due to its non-invasive nature and its potential for localized ablation and efficient penetration [70]. Correction techniques have been successfully applied to correct the focal position accuracy and intensity on emission in transcranial ultrasound therapy, with registration error corrections with respect to the treatment location ranging from 0.5 mm to 2.3 mm [5, 97]. Such techniques have also been shown to substantially improve image quality and target resolution through the skull both in real-time and in conventional imaging [71].

It should be noted that in therapy, a one-way correction is necessary for the improvement of target focusing, whereas in imaging the correction must be calculated and applied twice, on both the emission and on the reception. This makes the process more sensitive to the quality of the correction. Moreover, when compared to ultrasound imaging, ultrasound therapy is performed at lower frequencies, at which the skull behaves in a less challenging way when compared to higher frequencies. This is due to several mechanisms, including the fact that the trabecular structure size distribution is comparable to the wavelengths employed in higher-frequency imaging (100-150 μm) [121], that lower frequencies are less attenuated, and that lower frequencies are less sensitive to aberration from the skull morphology.

The difficulties present in transcranial imaging have stalled its growth compared to therapy, and other imaging methods are usually preferred to depict the brain vasculature at high resolution. Most significant work in transcranial brain imaging has been performed using Transcranial Doppler ultrasound (TCD), a

robust method in vascular imaging and flow measurements in the brain that has been used for more than 50 years [108]. Due to its ability to record cerebral hemodynamic changes in real-time, TCD is often paired with cognitive studies [198]. Color Doppler Imaging (CDI) can demonstrate the relative direction and velocity of blood flow in brain vessels, superimposed on a conventional B-mode ultrasound image of the stationary tissue. Doppler imaging is subject to the same limitations as conventional ultrasound as far as image quality is concerned, namely significant registration errors and insufficient spatial resolution for detection of sub-wavelength targets. To address these limitations, groups have employed 3D helmet-like array structures with 3D Doppler capabilities in conjunction with phase corrections [87] which can generate images of millimeter sized vascular structures, but they are still not capable of imaging smaller vessel anomalies and capillary structures, which require sub-wavelength resolution.

One of the pioneer studies in the field of super-resolution transcranial imaging, showed that a 255 μm radially sized microtube can be successfully super-resolved transcranially using a sparse hemispherical receiver array at 612 kHz [120]. This type of array is typically used in therapeutic applications which use frequencies lower than the clinical imaging frequencies, lowering the resolution. Furthermore, grating lobes from the sparse transducer spacing reduce the contrast, and the helmet-like form factor requires a water path, which limits the clinical imaging translatability of such a design. Even with a total accumulation of 3000 frames, it was challenging to fully populate the tube with detected bubbles, leaving some uncertainty in the exact shape and size of the tube. Compared to the imaging proposed here, it is expected that the higher frequency of 2.5 MHz, which will increase the aberrating effects of the skull, could, nevertheless, improve the resolution by a factor of 4. The versatility of the multiple-target focused emission in the present work also allows for more effective energy deposition, especially in a scattering environment if it were to be applied *in vivo*. The transmit-receive aberration correction proposed here should improve the image accuracy and quality. Finally, the conventional clinical transducer array on which these imaging sequences rely, has been used extensively in clinical imaging and does not suffer from any translatability restraints.

Here, we demonstrate the feasibility of super-resolution imaging of 208 μm targets through an *ex vivo* human skull, by performing experiments using focused ultrasound and high frame-rate focused sequences on a clinical phased ultrasound transducer array. Two experimental configurations are presented, imaging a microtube placed in the out-of-plane direction and in the in-plane direction with respect to the transducer, both with a diameter of 208 μm, at a depth of 68.5 mm. Phase corrections that take into account the individual skull morphology are applied to improve the sensitivity in bubble detection and the accuracy of target registration

in both lateral and axial dimensions. Micro-Computed Tomography derived maps of a human skull are converted into acoustical properties, and then used as as input to a custom simulation tool (called Fullwave) that we have developed to model acoustic propagation through the skull [151, 144, 149]. Simulations of acoustic propagation through the skull are used to determine the expected maximum theoretical improvements for phase corrected imaging of sub-resolution targets.

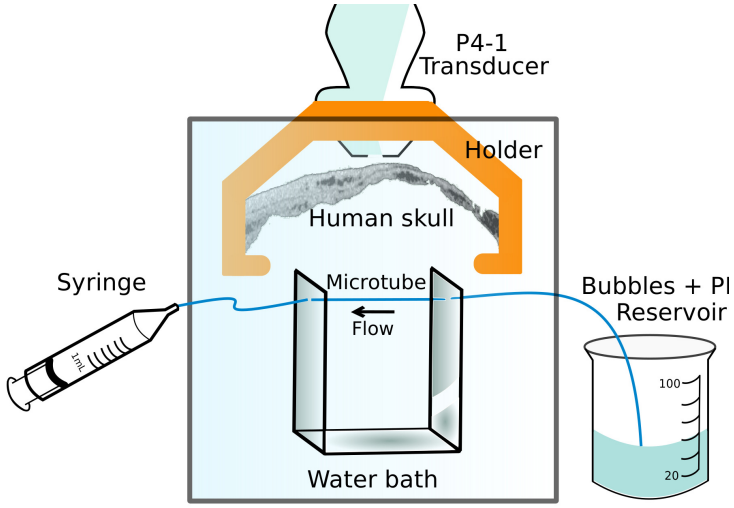

Figure 6.1: Schematic of the experimental setup. A custom 3D printed holder secured the skull in place while a separate tube holder allowed for both tube configurations with 90 degree rotations.

6.2 Methods

A cleaned human skull specimen was cut in half across the sagittal suture. The temporal region of the skull was used for imaging since it is relatively thin, and therefore provides a good acoustical window. To remove air trapped in the porous structure of the skull, it was degassed for 12 hours in water using a vacuum pump. A sketch of the experimental setup can be seen in Fig. 6.1. A custom designed skull and transducer holder was 3D printed and used to rigidly secure the skull in place with respect to the transducer. Since the phase correction is sensitive to movement, this holder ensured that the skull remained immobile throughout the duration of the whole experiment and also allowed for the attachment and detachment of the skull for different acquisitions, hence ensuring the stability and repeatability of the experiment. In addition, an adjustable microtube holder was built to secure a thin-walled polycarbonate microtube, with an inner diameter of 208 μm and an outer diameter of 250 μm (Paradigm Optics Inc., WA, USA), in place. The holder can rotate by 90 degrees around the axial dimension, which allowed the microtube to move from an

out-of-plane configuration to an in-plane one. These parts were placed in a 56 L tank filled with degassed water.

Lipid-encapsulated microbubble contrast agents containing decafluorobutane were formulated as described in previous work [86], and were diluted to a concentration of 1.6×10^6 bubbles/mL. These microbubbles were measured with an Accusizer (Accusizer 780, PALS-Particle Sizing Systems, FL, USA) and typically have a mean diameter of less than 1 μm. A pump driven syringe was attached to one end of the tube to induce constant flow of the microbubble contrast agent solution. The syringe was refilled through a continuously mixed reservoir of microbubble solution at a refill rate of 75 μL/min. This configuration allowed for the establishment of uninterrupted, continuous flow, as well as the capability of replacing the reservoir when needed. Since bubbles can burst and aggregate in the bottom of the container, to ensure that the concentration remains constant throughout the experiment, the bubble reservoir was mixed as well as replaced, and flow was re-established, after every 6 minutes.

Imaging was performed with a Verasonics Vantage research scanner (Verasonics Inc., Redmond, WA, USA) and a P4-1 phased array transducer that transmitting 1 cycle pulses at 2.5 MHz and at a framerate of 700 Hz. A focused wave with a focal depth set at the position of the microtube was emitted. A more detailed description of the imaging sequence is given in subsection 6.2.2.

The two experiments, with the microtube in two different orientations with respect to the transducer, as well as the extraction of the correction are described in detail in subsections 6.2.1,6.2.2 and 6.2.3.

6.2.1 Phase profile extraction for focal correction

Prior to mounting the skull, a microtube filled with air, oriented in the out-of-plane direction with respect to the imaging field, was aligned at the center of the transducer, laterally, and at 6.85 cm of depth. A single full-aperture focused emission, with the parameters mentioned above and with an amplitude of 168 kPa, targeted the microtube position. The whole aperture was also used to receive the RF data.

This data served as a reference while computing the skull-distorted version of the tube profile and the relative lag between the two. As expected, the backscattered reflection from the microtube appears as a hyperbolic phase profile. The phase associated with the microtube was isolated and flattened by subtracting the equivalent delay of the focused emission, which was also a hyperbola. In principle the emitted focused profile should be identical to the backscaterred phase profile. However, this was not exactly true, due to minor alignment errors in the positioning of the microtube. These alignment errors can be attributed to the manual

alignment of the microtube. A cross-correlation algorithm, which correlates data from each channel of the transducer to a reference channel of the same data set, was applied to extract the microtube profile.

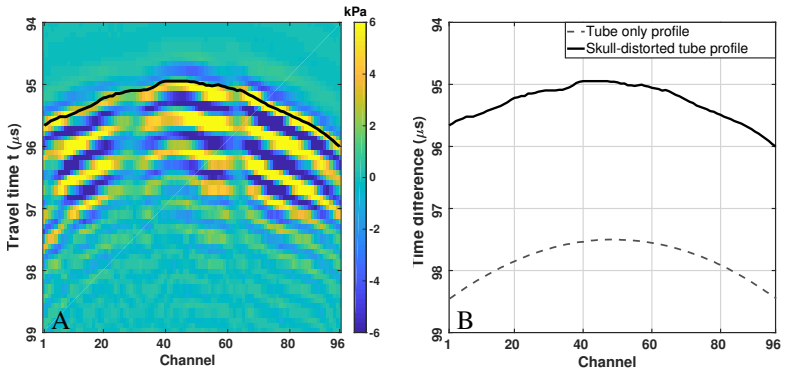

Figure 6.2: (A) The detected profile of the microtube underneath the skull measured with the correlation detection method (black line), plotted on the RF data. (B) Detected profile of the target without the skull and the target through the skull in time units. The RMS difference between the two profiles was measured as 90.3 ns.

Subsequently, without perturbing the position of the tube and transducer, the skull was mounted on the special holder and stabilized so that it remained in a fixed registered position throughout the experiment. A second acquisition, using the same single focus sequence, was performed at the same target, but at 2.21 MPa to account for the attenuation from the skull and to deliver approximately the same pressure amplitudes at the microtube location. The raw data acquired through the skull shown in Fig. 6.2 (A) corresponds to the backscattered signal from the microtube, after it has crossed the skull twice, on emission and reception. The interaction of the pulse with the skull causes variations in amplitude arising from interference in parts of the phase profile, as well as a distortion of the shape, which is no longer hyperbolic. The same process, of flattening the image and correlating to a reference channel, was repeated as described above, and yielded the skull-distorted phase profile. The extracted skull-distorted profile is plotted on top of the raw data as a black solid line.

The tube profile and the skull-distorted tube profile, can be seen in Fig. 6.2 (B). An average offset of 6.32 λ was measured between the two profiles. This offset is caused by the significant difference in the speed of sound between the skull and the medium. These profiles are also notably different in shape, which is a direct result of the aberration caused by the skull. The root mean square value for the difference in time between these two profiles, after the offset between the two profiles has been compensated for, can also serve as a quantitative measure of skull induced aberration. In this particular acoustic window, aberration in time

was estimated to be 90.3 ns (0.07λ). The skull-distorted profile served as input to the phase corrected version of the sequence that was implemented on the Vantage system to apply the correction on emission, and later the relative difference between the two profiles was used to correct on reception. The final B-mode images were thus corrected both ways.

6.2.2 Out-of-plane experiment

Once the profiles were extracted, microbubble flow was established in the microtube. Three acquisitions were performed: First, the microtube only, second, a skull-microtube experiment using an uncorrected conventional emission and lastly, a skull-microtube experiment with the focusing correction on emission and reception. To apply the correction on emission, the previously extracted skull-distorted profile, was inverted in time, and was used as a delay input in the single focus sequence described in subsection 6.2.1.

For each of the three acquisitions, 1000 frames were recorded. In the absence of the skull a 168 kPa emission was used whereas when the skull is mounted a 1.35 MPa emission was used. While the skull is absent, lower pressures must be applied to ensure that the bubbles will not burst, whereas with the attenuating skull present, higher pressures can be applied, still within a mechanical index lower than 1.5. Note that the amplitude is lower while the microbubble flow is being imaged, as compared to the 2.21 MPa used in subsection 6.2.1 for the air-filled microtube imaging, to further ensure the integrity of the microbubbles, but at the same time provide sufficient energy.

To correct on reception, each channel of the raw data from the corrected emission acquired, was delayed accordingly to the relative lag between the tube profile and the skull-distorted profile. This yields data that is corrected both ways. Following this step, all three datasets, were beamformed using a $\lambda/12$ spaced grid and a conventional delay-and-sum algorithm.

As a first microbubble detection step, an SVD filter was applied to the beamformed ultrasound images to isolate bubble appearances from the static background [33], by removing the highest 2 singular values. A range of values from 1 to 5 was explored for each emission case, in both the out-of-plane and in-plane configurations, and the final values were selected with the metric of success being noise minimization and bubble appearance frequency and brightness. Values greater than 5 were found to produce only background noise in all cases. A centroid localization algorithm was used to localize the microbubbles in the filtered images on a 40 μm grid. A bubble size filter was used to only detect bright spots that have a size larger than one wavelength, which is the minimum size of a point spread function. An upper limit was not set

for the bubble filter, since in a confined environment of a single microtube, and at a low concentration, we do not expect clusters of bubbles with a significantly large size that would alter our resulting images. The accumulation of the position of all the detected bubbles among the 1000 acquired frames lead to the final super-resolution image.

6.2.3 In-plane imaging

The microtube was subsequently placed in-plane with respect to the imaging plane. Three different cases were studied; no skull (the microtube alone), an uncorrected conventional emission through the skull and a corrected emission through the skull on emission and reception. To scan the entire length of the tube, the full aperture was steered along different angles. The imaging field was divided into 96 different locations spanning a distance of 30 mm, spaced at a constant interval of $\lambda/2$. The steering angle was calculated based on the grid spacing and ranged from -0.2 to 0.2 radians. The focal depth was kept constant at 6.85 cm for all focusing locations. The whole-aperture was also used to receive 1000 frames at each focal position. This resulted in a full field scan comprising 96 different acquisitions and a cumulative total of 96000 frames. A full lateral scan had a duration of 4 min. For the tube without the skull 168 kPa were emitted and for the cases where the skull is present, 1.35 MPa were emitted.

For the corrected emission through the skull, the correction extracted as described in section 6.2.1, was added to each steered delay profile for each focus. The same correction profile was overlaid on the steering profiles even though the correction is local in nature, i.e it is extracted from a target in the center of the transducer imaging field. This is consistent with the assumption that the relative distance between the skull and the transducer is smaller than the distance between the skull and the target. Therefore the spatial dependence of the skull distortion is assumed to be small. A more sophisticated approach would be to use different correction profiles for different imaging positions. However it was expected that a single phase correction would correct the registration errors in some neighborhood of the central target.

For the correction on receive, each of the 96 acquisitions was corrected using the relative lag between the tube and skull-distorted profiles prior to beamforming, as mentioned in section 6.2.2. Beamforming of the RF data was performed using a conventional delay-and-sum algorithm that took into account the steering angle. Each of the 96 sets of a 1000 frames was beamformed independently, and was subsequently filtered with the SVD filter which removed the 3 highest singular values for the microtube only case, and the 2 highest for both the experiments through skull. When the skull was present the removal of 2 values optimally reduced

diffuse clutter, likely from multiple reverberations between the skull and transducer face. In the absence of the skull the removal of 3 values optimally reduced local clutter from reflections from the microtube walls. Subsequently, bubble appearance events for each of the 96 sets were individually localized using the centroid detection algorithm across the whole imaging field. This resulted in 96 separate full-field super-resolution images. This is due to the fact that although the foci are localized, microbubbles are detected up to 1 mm away from the target position. The 96 individually generated super-resolution images were combined, by arithmetic summation, to produce the final super-resolved image depicting the whole microtube.

6.2.4 Simulations

The Fullwave Simulation tool is a numerical solver based on finite differences in the time domain (FDTD) [151] which can be used to model ultrasound propagation with a high dynamic range. This tool has been extensively used for various acoustic applications. A few examples include simulating the thermal effects of focused ultrasound in transcranial brain therapy [67], modeling of acoustic cavitation risk in the brain [7] and transcranial focused ultrasound parameter optimization [98].

Here this numerical tool was used to produce two dimensional simulations in which the experimental conditions were closely mimicked. The sources of image degradation in ultrasound imaging depend not only on aberration of phase profile clutter, which are corrected, but also on multiple scattering or reverberation artifacts, which are not corrected [131, 132]. Simulations also provide a more controlled acoustical environment, where the properties of interest can be investigated without the interference of the experimental setup. The aim of the simulations is to determine the imaging improvements under a best-case phase aberration correction scenario and allow us to investigate the one-way distortion of the ultrasonic beam, which can in turn provide us with a more effective means to phase correct.

A CT scan of the same skull specimen used in the experiment was converted to speed of sound, attenuation and density maps that were used in the simulations. A 2D field of view from the temporal region of the skull was selected. The maps of the simulation were calibrated with amplitude measurements at the focus to match the experimental pressure conditions. The density and speed of sound maps were calculated as linearly scaled versions of the CT image in Hounsfield units with maximum values of 1850 kg/m^3 and 2900 m/s, respectively [1, 8]. This map conversion process has been previously used and validated for focused ultrasound surgery and has been used for transcranial simulations with the Fullwave tool [132, 8]. The size of the simulation field was 80 mm in depth and 32 mm in width. Transmitted pulses had the same

parameters as described in the experimental setup. The grid size was set to 38.5 μm which is equivalent to 16 points per wavelength and a Courant-Friedrichs-Lewy [25] condition of 0.3 was used. A target, with a single pixel size, was placed at 6.85 cm in depth. The transducer was located at the top of the medium and the maximum pressure of 2.21 MPa at the emission was matched to hydrophone measurements for the P4-1 transducer. Simulations were performed on a Linux Fedora 25 (v.4.10.13-200.fc25.x86 64) system running Intel Xeon® E5-2630 v4 Processors at 2.20 GHz. The simulation code was written in C, and was on only one thread. Post-processing was performed on MATLAB. Each simulation for each individual emission case has a duration of 7 min. Although we are currently using only one thread to run each simulation, the system's parallel capabilities can be exploited to reduce total time for multiple simulations.

The simulated acquisition process was the same as the experimental process described previously in subsection 6.2.1. Three acquisitions were performed, one of the microtube without the skull, an uncorrected emission through the skull, and lastly a corrected emission through the skull. To derive the correction profile, the target was used as a point source, i.e. the experimentally described pulse was emitted directly from the target, propagating the wave through the skull, which was then received by the transducer above the skull (one way travel). In this manner, the wave crosses the skull only once, hence undergoes half the distortion. The received raw data was processed as described in subsection 6.2.1. By means of correlation, a skull-distorted profile was directly detected. A second emission was performed by adding this profile to the focused delay emitted from the transducer, which constituted the corrected emission. The received data were first corrected on reception, following the same process of imposing a relative lag to each channel, and then beamformed as previously described in section 6.2.

6.3 Results

6.3.1 Out-of-plane imaging and simulations

The B-mode images from the out-of-plane target experiment, shown in Fig. 6.3, can be used to characterize the conventional delay-and-sum point spread function (PSF) of the imaging system. The reference PSF of the microtube without the skull is shown in (A) and the B-mode image generated by the conventional uncorrected focused emission is shown in (B). The skull causes the point target to shift both laterally, as a result of aberration, and to move shallower, possibly as a result of aberration and definitely due to the increase in the average speed of sound. The shape of the PSF in (B) also appears to be degraded when compared to the

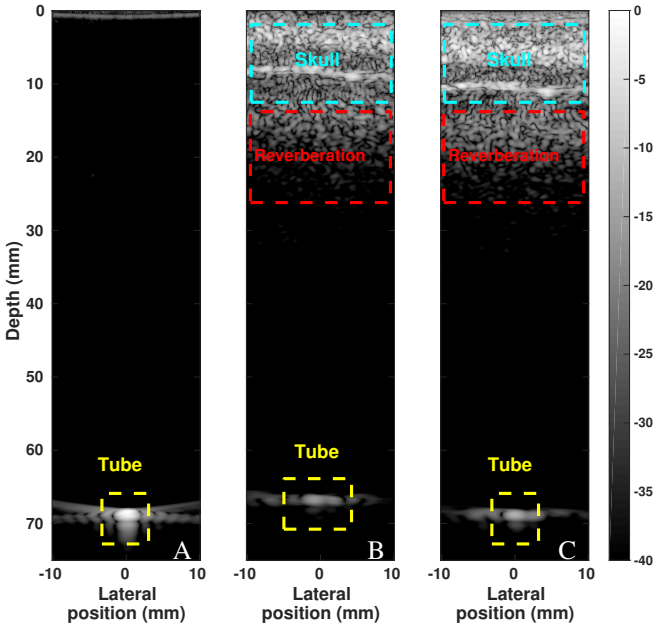

Figure 6.3: Standard B-mode images for (A) the tube without skull, (B) uncorrected and (C) corrected emissions through skull, all in the out-of-plane direction. Scale for all images is in dB. The amplitude improves by 3.9 dB in the corrected case.

microtube only B-mode image in (A). In the B-mode image generated by the corrected emission (Fig. 6.3C), the maximum signal amplitude compared to the uncorrected B-mode increases by a factor of 1.6 (3.9 dB), defined as the ratio of amplitudes I_c/I_u where c stands for the corrected and u for the uncorrected emission. In this image, the position appears to have been corrected and the shape also qualitatively improved. In both uncorrected and corrected B-modes (Fig. 6.3B and C), the skull is visible in the first 10 mm of depth, followed by a reverberation zone spanning approximately 20 mm.

To quantify the improvement produced by the phase correction, beamplots are plotted for each emission case Fig. 6.4. The beamplots were calculated by averaging across all the frames and extracting the profile as a function of lateral position at the depth where the target exhibited its maximum amplitude, since there is an offset in depth between the B-modes for each acquisition and a global depth cannot be determined. Fig. 6.4A shows the experimental beamplots derived from the three B-modes, corrected and uncorrected through the skull and the microtube only, on a normalized dB scale. The difference in position of the maximum of the main lobe between the corrected, uncorrected cases and the microtube (ground truth) yields the lateral registration error ΔL. The registration error laterally, was measured as 50 μm for the corrected case and at 990 μm for the uncorrected case yielding an improvement of 940 μm. Registration errors were also estimated axially, referred to as ΔD, to be 300 μm and 1790 μm respectively, exhibiting a 1490 μm improvement. The side lobes for the tube profile in Fig. 6.4 (A), are not symmetrical and deviatFe slightly from a classical point

Table 6.1: Summary comparison for the experimental B-mode images of the out-of-plane experiment.

	Experimental B-mode					
	ΔL (μm)	**ΔD (μm)**	I_c/I_u	**RSL (dB)**	**LSL (dB)**	**MLW (μm)**
Corrected	50	300	1.6	7	11	2533
Uncorrected	990	1790	-	3.7	10.5	4454
Tube	-	-	-	16.1	14	2011

Table 6.2: Summary comparison for the simulated B-mode images.

	Simulation B-mode					
	ΔL (μm)	**ΔD (μm)**	I_c/I_u	**RSL (dB)**	**LSL (dB)**	**MLW (μm)**
Corrected	62.5	210	2.76	12.3	21.7	2060
Uncorrected	625	620	-	13.3	12.2	2094
Tube	-	-	-	12.2	12.2	1630

Table 6.3: Summary comparison for the super-resolved images of the out-of-plane experiment.

	Super-Resolved			
	ΔL (μm)	**ΔD (μm)**	**Counts**	**Counts ratio**
Corrected	80	200	1040	1.48
Uncorrected	480	2000	700	-
Tube	-	1001	-	-

target shape due to minor alignment issues, and due to the fact that the microtube was manually aligned using live imaging, therefore there was a human error component present. Furthermore, since a solution of microbubbles was being imaged, the exact position of the microbubble can deviate from the actual center of the transducer and center of the microtube. The uncorrected profile is substantially degraded in shape, with asymmetrical side lobes that are hard to discern. The side lobe amplitude is 10.5 dB for the left side lobe (LSL) and 3.7 dB for the right side lobe (RSL). After applying the correction, the shape, especially of the main lobe, appears to be partially restored, however the side lobes remain high. Specifically, the left side lobe has an amplitude of 9 dB whereas the right an amplitude of 7 dB. At -6 dB, the main lobe width (MLW) of the corrected profile is estimated at 2533 μm (522 μm larger than the width of the microtube only profile), whereas the width of the uncorrected profile is estimated at 4454 μm (2443 μm larger), due to its degradation in shape.

The improvements from experimental phase aberration correction were compared with the best-case scenario from the simulations. These simulated plots (Fig. 6.4B), show the B-mode beamplots from the

same three scenarios, namely for the corrected, uncorrected and microtube only emissions. The registration error laterally, is 62.5 μm for the corrected case and 625 μm for the uncorrected case, an improvement of 562.5 μm.

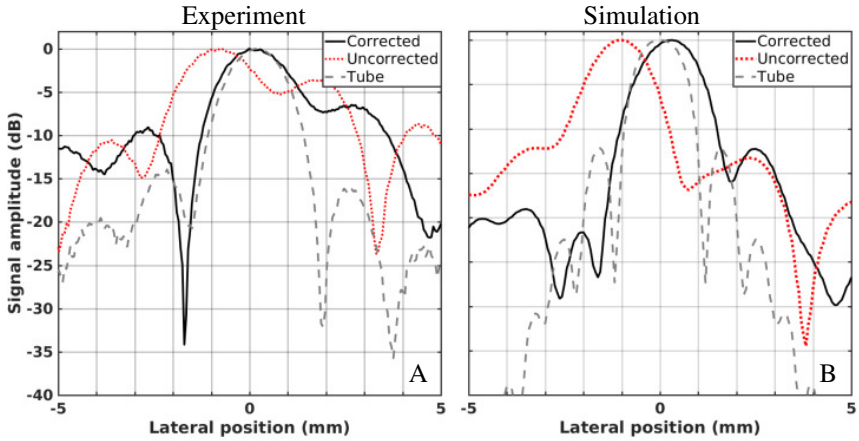

Figure 6.4: (A) Beamplots for all three experimental cases, the lateral registration error of the tube's position in the uncorrected case was 990 μm and in the corrected case it was 50 μm, as measured in the point target B-mode images. (B) Simulation beamplots for a different position of the skull in the temporal region. Correction was derived from a point source in the place of the target.

Axially, the registration error is 210 μm for the corrected B-mode image, and 620 μm for the uncorrected B-mode, an improvement of 410 μm. Additionally, the amplitude increased by a factor of 2.76 for the corrected B-mode when compared to the uncorrected counterpart. Fig. 6.4B, shows that the shape of the tube without the skull is as expected for a point target that is perfectly centered. The uncorrected emission through the skull degrades the shape of the side lobes and causes a noticeable lateral error due to aberration effects from the skull. After applying the correction derived from the one-way distorted profile, one could expect an almost full restoration of the shape and position of the beamplot. However, that is not the case even in this gold standard setting. At -6 dB, the main lobe width for the corrected emission is estimated at 2060 μm, which is larger by 430 μm compared to the microtube, and the size and symmetry of the side lobes still deviates considerably, with the left side lobe at 21.7 dB lower than the main lobe and the right one at 12.3 dB lower. Although aberration was completely removed in the simulation, multiple reverberations within the skull and between the skull and transducer, which cannot be corrected with a phase delay, still have a degrading effect on the image quality.

The super-resolved images produced from the out-of-plane experiment are shown in Fig. 6.5 for the conventional uncorrected emission in (A), and the corrected emission in (B), both through the skull. While

qualitatively assessing the images, an evident degradation in the shape of the microtube is observed in (A), especially in the lateral direction. The shape after the application of the correction appears substantially improved and rounder in (B). Sensitivity in bubble detection for the corrected and uncorrected emissions through the skull, was calculated as the sum of bubble counts among all the accumulated frames (1000 used in this case). Specifically, in the uncorrected case 700 bubble events were detected compared to 1040 bubble events in the corrected case, which amounts to an improvement in sensitivity of a factor of 1.48, defined as the ratio of counts, for the corrected case. If we were to assume no bubble destruction due to handling or acoustic pressure, for a single out-of-plane acquisition that lasts 3 sec, for the given flow rate and microbubble concentration of 1.6×10^6 bubbles/mL, we can place an upper bound of 6000 bubbles that could possibly be detected. Since the corrected acquisition detects 1040 bubbles, this implies that at least 17.3% of the total bubbles are being detected.

To quantify the detection accuracy of the microtube in both directions, the sum of the bubble counts as a function of lateral (A) and axial (B) position are shown in Fig. 6.6. The corresponding microtube only profiles are included for reference. In Fig. 6.6A, the lateral profiles have a registration error of 80 μm for the corrected super-resolved image, while for the uncorrected images the error is 480 μm, as estimated by the center of mass of the bubble positions. Size estimations of the detected microtube are also made by measuring the full width at half maximum (FWHM) for the curves. The corrected emission curve laterally estimates the size of the microtube at 200 μm, while in the uncorrected case, the size is estimated at 1 mm. Note that the actual size of the microtube is 208 μm. A histogram analysis was performed with bubble events binned on a 40 μm $\times$ 40 μm grid to calculate bubble appearance frequency as a function of radial distance from the center. Considering the detected center of the tube during the corrected emission, 72% of the total counts were found inside a 200 μm diameter, whereas the equivalent percentage of the uncorrected emission, for the corresponding detected center, is 41%. This is comparable to previous reports [120].

In Fig. 6.6B, the registration error in depth is 200 μm for the corrected super-resolved image and 2000 μm for the uncorrected counterpart, an improvement of 1800 μm. The corrected emission curve as a function of depth, estimates the FWHM axial size of the microtube at 240 μm, while in the uncorrected case the equivalent size is estimated at 160 μm. The deviation from the actual size in the axial direction is in the λ/20 range for the corrected emission profile.

These registration error estimations, for both the B-mode and super-resolved images, in both directions, as well as beamplot characteristics are summarized in Tables 6.1, 6.2 and 6.3, where ΔL denotes the lateral

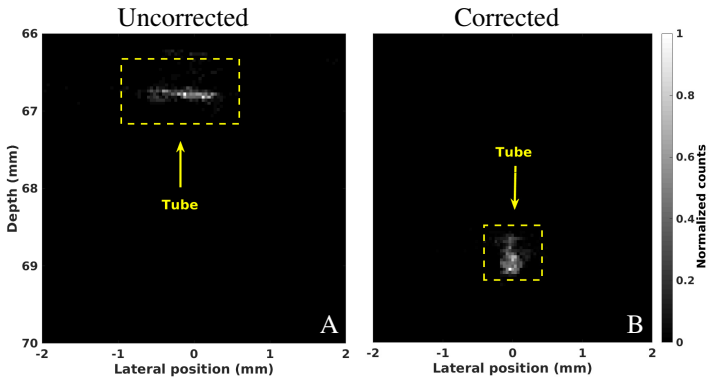

Figure 6.5: Super-resolved images for the (A) uncorrected and (B) corrected emissions through the skull. Scale in both cases is normalized number of bubble counts.

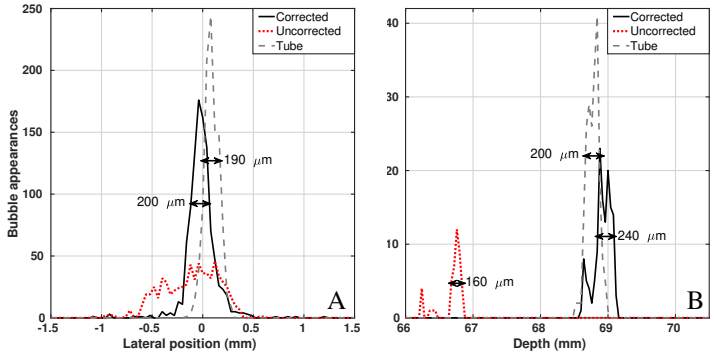

Figure 6.6: Sum of bubble counts as a function of (A) lateral position and (B) depth, for the uncorrected and corrected super-resolved images. The tube profiles are also provided for reference and registration error estimation ground truth. Sensitivity improves by a factor of 1.48 for the corrected case.

registration error, ΔD for the registration error in depth, I_c/I_u is the amplitude improvement ratio, RSL is the right side lobe amplitude, LSL the left side lobe amplitude and MLW stands for the main lobe width. Main lobe width estimations were performed at 6 dB of intensity. The estimates made from the B-mode images and the super-resolved images are consistent, with a maximum deviation of λ/20 between them.

6.3.2 In-plane transcranial imaging

The super-resolved images of the in-plane corrected and uncorrected emissions through the skull as well as the microtube without the skull are shown in Fig. 6.7, labeled as (A)-(C), respectively. For the uncorrected super-resolved image in (B), when compared to the microtube only super-resolved image in (C), a deviation from the true shape of the tube as well as an offset in depth can be qualitatively observed. However, even without applying a correction, the whole length of the microtube can still be resolved and observed, albeit with a large error in position. Both the shape and the offset in depth are improved after the application of the

correction, as shown in Fig. 6.7A. For the corrected emission 79965 bubble appearance events are detected, which compared to 61198 events in the uncorrected emission reveal an improvement of 31% in sensitivity in bubble detection.By comparing the number of detected bubbles to the total expected number of bubbles flowing through the tube for an acquisition of a duration of 4 min, and while still assuming zero bubble destruction, a volume of 300 μL would pass through the tube. Based on our concentration, a total of 480000 bubbles would be expected and 79965 were detected, i.e. 16.7% of the total expected bubbles. This sensitivity can also be calculated using a static estimate. For a tube of this given diameter, at the given concentration and with a length of 20 mm, assuming steady state conditions in the flow, and that bubbles are not detected more than once, we would expect 1100 bubbles to be present in the field of view at any given instant. We are detecting approximately 80 bubbles per single frame in time, therefore that would give us an estimate of 7% for the sensitivity. The lower limit of sensitivity is thus, depending on the approach and the assumptions made, between 7-16.7%. As a reference, the total bubble counts for the tube without the skull, which were at a lower pulse pressure, are 53427.

Fig. 6.7D, shows the bubble sum profiles as a function of depth for a given central lateral position, which is highlighted in Fig. 6.7A - 6.7C with boxes. The profile of the microtube without the skull is provided as an actual position reference. Axial size estimates of the detected microtube for all three aforementioned cases are given by the FWHM of each curve. In both uncorrected and corrected emissions through the skull, the axial size of the microtube is estimated at 200 μm. The registration error between the true position of the microtube, the detected position for the uncorrected image, and the corrected image in depth was estimated and then averaged for each lateral position spanning across the central 8 mm region of the tube. This yielded an estimate of 284$\pm$58 μm for the corrected emission and 1885$\pm$196 μm for the uncorrected emission.

6.3.3 Transcranial rat tail vein imaging

As a transition from ex vivo and phantom experiments the rat tail vein presents a great target for super-resolution transcranial imaging. It is an anatomically easy to isolate vessel, without breathing motion and its size is ideal for super-resolution applications at a frequency of 2.5 MHz.

For the experiment,a Fischer344 rat was anaesthetized using isofluorane and placed on a platform. The tail vein was accessed using a catheter attached to a 1 mL syringe and a microbubble solution of a concentration of 2 * 10^7 bubbles/mL was perfused at a flow rate of 15 μL/min through the tail vein. The tail was submerged in water as illustrated in Fig. 6.8. For the focused imaging sequence, 96 individual foci,

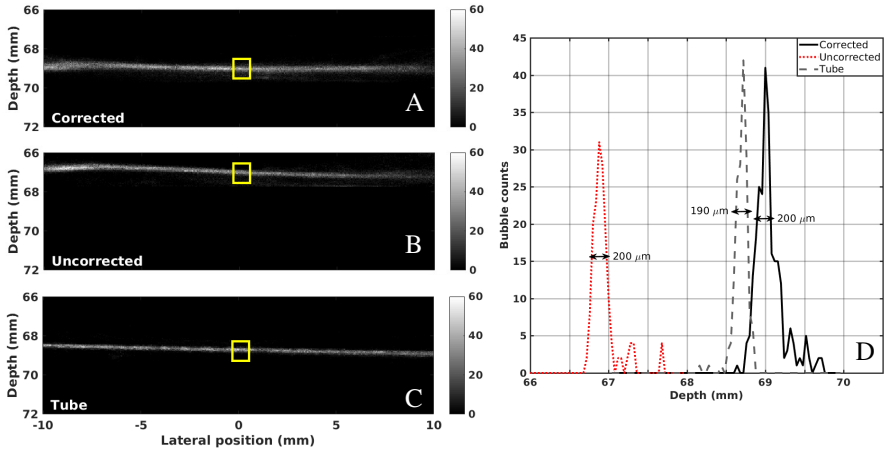

Figure 6.7: Super-resolved images for (A) the corrected emission through the skull, (B) the uncorrected emission through the skull and (C) the microtube without the skull. Scales are in number of bubble counts. (D) Laterally averaged counts as a function of depth for the corrected and uncorrected images with the skull and the microtube only as reference. Solid boxes show the location from where plot (D) was generated.

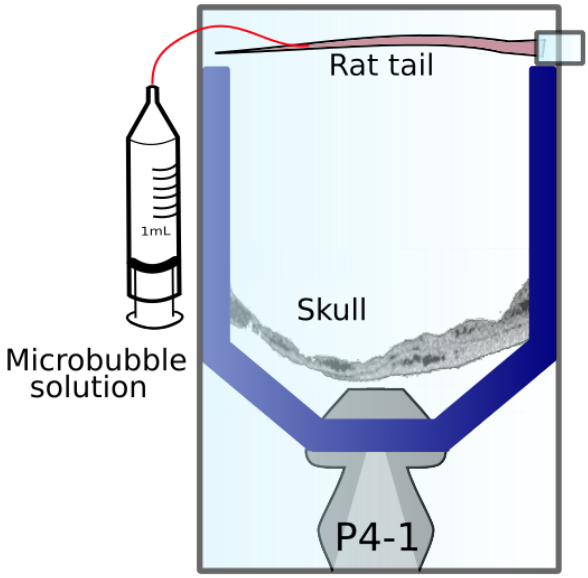

Figure 6.8: Schematic of the setup used for the rat tail vein experiments.

laterally spaced by lambda/2 were used at an equidistant depth focusing on the tail location. Each B-mode image for each focus was beamformed separately using a conventional delay and sum algorithm. The B-mode was subsequently filtered using a singular value decomposition filter to remove the bubbles from the static background. The bubble appearances were finally localized using a centroid localization algorithm, including a threshold, and the final super resolved image was the sum of all 96 individual images.

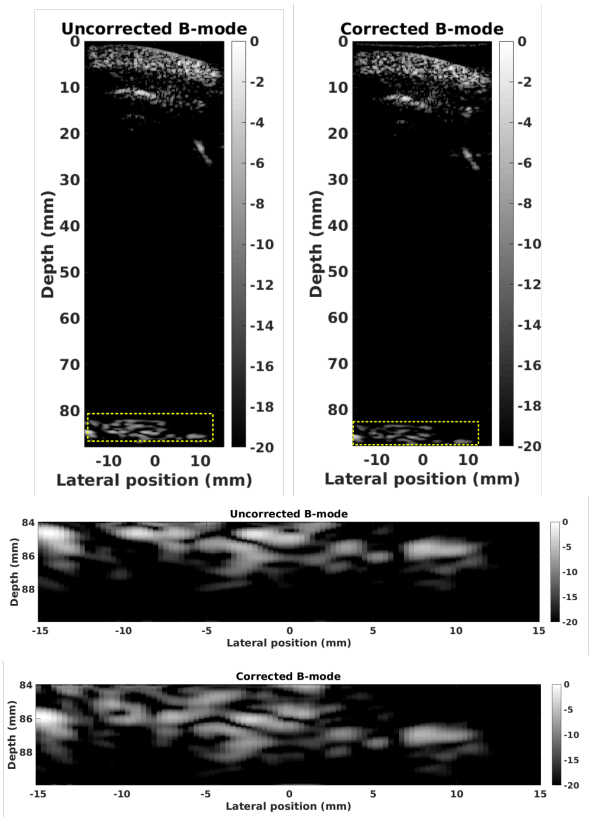

Figure 6.9: B-mode images of the rat tail vein through a human skull specimen and the zoomed in counterparts for an uncorrected focused emission and a phase corrected focused emission, as labeled. Units are in normalized dB.

For each focus, 1000 frames were acquired, resulting in a total of 96000 frames per final super-resolved image. In the super resolved tail vein images, 125921 bubble counts were recorded for the uncorrected image and 157342 bubble counts for the corrected counterpart, signifying a factor of 1.25 increase in sensitivity. The size of the vessel was estimated at 280 μm for both super-resolved images. It should be noted that the acquisitions were performed twice, once for a conventional focused imaging scheme, and once more while applying an aberration correction on emission and on receive as described in earlier chapters.

6.4 Discussion

We have shown that super-resolution imaging through a human skull specimen of out-of-plane and in-plane microtubes with a size of 208 μm (λ/3) is feasible at 2.5 MHz, even without phase correction depending on the application and the desired accuracy. In the uncorrected out-of-plane emission case, the shape of the microtube was degraded laterally and the accuracy of the size of the microtube was estimated at

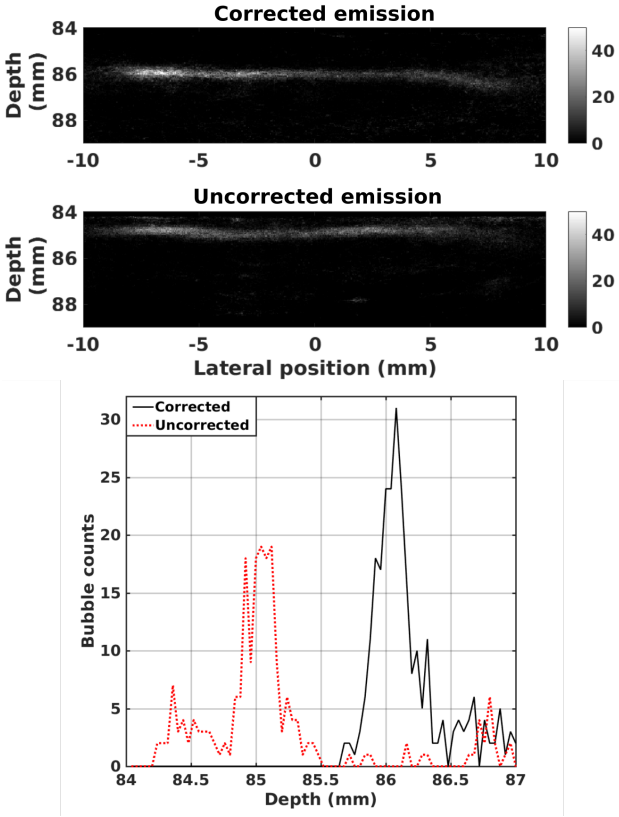

Figure 6.10: Top to bottom: Super-resolved image of the rat tail vein using a corrected transcranial emission, super-resolved counterpart using a conventional focused emission and axial profiles of the two images to establish Full-Width at Half-Max (FWHM) sizes of the vein.

1 mm, while its central position was approximated at 480 μm off-center. Nevertheless, there was a sufficient number of microbubble appearances to indicate the presence and approximate position of the microtube. Further phase correcting reduced the lateral registration error to 80 μm as measured in the super-resolved images. In the case of imaging the in-plane target through the skull, an adequate amount of microbubbles was detected to fully populate the vessel-like structure even without phase correcting. This however, may not always be the case, in an *in vivo* setting where attenuating tissue is present. Scattering from the tissue is expected to further decrease detectability of the microbubbles and may increase the need for correction. Furthermore, another improvement that would benefit detectability would be the use microbubbles of a mean diameter larger than 1 μm, considering the low frequency at which the experiments are performed.

Here, using a 2.5 MHz probe, the predicted diffraction-limited resolution is restricted to a minimum of 308 μm. However, according to Desailly *et al*. [40], the theoretical resolution limit based on the Cramer-Rao lower bound, is a few microns (2.1 μm) for a frequency of 3 MHz in liver (λ/244). In practice however, for injected microbubbles Desailly *et al*. [41] reported an upper bound of λ/11 in resolution using a 1.75 MHz probe. In more recent work, Christensen-Jeffries *et al*. [19] have resolved vascular structures as small as 20 μm (λ/10). Although an explicit resolution analysis has not been performed here, one would expect the resolution limit to be at best comparable to these results. It is more likely, however, that the added reverberation and aberration that the human skull introduces would lower this resolution estimate.

In addition to the lateral registration error, the shape of the tube prior to the correction is also notably degraded in shape laterally, even in the super-resolved images, as seen in Fig. 6.5A. This stems from the fact that the PSF, which is used by the centroid localization algorithm, is distorted, as seen in Fig. 6.3B. This degrades the estimate of its geometric center. This could possibly be corrected by using a distorted PSF as a reference in a correlation-based localization. After correcting for aberration, the shape of the PSF is not fully restored, even in the best case scenario provided by our simulations, which *completely* removes aberration. This shows that reverberation, which is not removed, has additional degrading effects on the image. It is worth mentioning also, that even in the corrected case, some distortion of the PSF persists. This could be attributed to reverberations from the skull, which cannot be corrected in this manner. Moreover, the lateral degradation of the tube shape as seen in the out-of-plane case is not evident in the in-plane configuration due to the direction of the tube with respect to the imaging plane. Even when targeting a single focal position laterally, multiple neighbouring microbubble events are still detected along the lateral axis.

The axial registration errors are largely a product of the speed of sound mismatch between the values for the skull and the water, and assuming that the skull's density distribution is homogeneous, it should be a constant global offset. That is however not exactly the case, since the shape of the skull is not perfectly flat. If we were to estimate the actual speed of sound values, based only on the information from the phase profiles that would be 1520 m/s through the skull, as opposed to 1482 m/s for the tube in water. This would provide us with a registration error of approximately 1.9 mm, which is very close to the final uncorrected images. The fact that this improves to the range of 200 μm means that the correction on reception, which compensates the effect of the speed of sound mismatch is effective, but what is more important and leads us to accept this correction as satisfactory, is the fact that it appears to be global, as shown in the shape of the corrected in-plane tube in Fig.7A, i.e. in an *in vivo* setting, as long as the axial correction is spatially homogeneous, it should not pose a limitation.

A single phase aberration correction profile was determined for the center of the field, and it was then applied to the entire field of view. This was performed under the assumption that a local correction is still effective across a lateral field of 30 mm, while also assuming that the distance of propagation between the skull and the transducer is sufficiently small. A more sophisticated version of the correction process would determine a specific correction for each imaging position, laterally and in depth. To obtain correction profiles that are specific not only to the imaging location, but also correspond to the steering angle being used, we would use simulation tools to pre-calculate the corrections. This could be similar to previous Fullwave simulations that were performed for human transcranial focused ultrasound therapy [144, 149]. Nevertheless in the current work, the imaging results did not show a noticeable decrease in bubble detection events, resolution, or accuracy as a function of lateral position, suggesting that the small distance assumption was valid.

Fullwave simulations of transcranial propagation, which provided a theoretical best-case scenario, showed improvements in both registration error and amplitude. The lateral registration error was 62.5 μm for the corrected image, and there was an improvement of almost λ from the uncorrected image, as well as a significant amplitude correction of a factor of 2.74. These simulation results therefore suggest that there may be room for improvement in the experimental phase aberration correction implementation. However the simulations also show that the width and shape of the main lobe and side lobes are not fully restored with phase aberration correction. This phenomenon was also observed experimentally and it is consistent with the interpretation that amplitude aberration and multiple reverberation also play a significant role in image

quality. Except for phase distortion, the skull also reduces the amplitude of the initial pulse, which may be partially compensated with amplitude correction techniques.

A limitation of the method as it was implemented, is that it is challenging to extract a correction from an aligned point target *in vivo*, since it is impossible to find such a target occurring naturally. This limitation has been previously addressed in focused ultrasound therapy, where pre-calculated simulation derived corrections for a specific registered location of the skull can be used [5]. These corrections can be produced as described in subsection 6.2.4 and, provided the CT scan used is accurately registered to the actual skull, they can be employed to phase correct a given region of interest, as previously performed in therapy transcranial ultrasound [97, 144, 149].

Currently, ultrasound is limited to the larger vascular structures in the brain (Circle of Willis, larger arteries), however, the ability to image 200 μm targets, suggests that smaller vascular structures in regions ranging from the mesencephalon to the cerebellum can be detected using the temporal window of the skull. Furthermore, since this method relies on the localization of individual bubbles, it can also be applied to track the microbubbles in the blood flow and provide velocity estimations at a higher resolution than traditional Doppler imaging.

6.5 Conclusion

In summary and conclusion, transcranial super-resolution imaging through a human skull is feasible at a frequency of 2.5 MHz, even without applying a phase correction, and with an existing clinical transducer. With the placement of the transducer in the temporal skull window when combined with phase correction, images of vessel-mimicking microtubes of a diameter of 208 μm with a lateral registration error as low as 80 μm were produced. The correction in the out-of-plane configuration thus reduced the error to the λ/8 range and increased sensitivity by a factor of 1.48 in the super-resolution images, as compared to the uncorrected emission. In the in-plane configuration the microtube was detectable with and without correction, however the correction increased sensitivity by a factor of 1.31 as compared to the uncorrected counterpart. This method has the potential to significantly improve the resolution and accuracy necessary for brain vascular mapping scenarios.

CHAPTER 7

CONCLUSIONS

In conclusion, we have developed an image quality improvement framework with applications to human transabdominal imaging, lung ultrasound imaging, and brain imaging, which are areas where improved resolution and contrast are crucial for the successful identification of structures and lesions that might aid in the diagnosis of pathological conditions. The role of two main sources of image degradation, phase aberration and multiple reverberations was studied in two challenging imaging environments: the human abdomen and the human brain. Their effects and relative contribution as a function of parameters such as target brightness, frequency and depth were characterized to better understand and design mechanisms for image quality improvement.

We also proposed a focused imaging super-resolution approach to improve the resolution of the brain vasculature by at least a factor of 10 compared to conventional B-mode ultrasound, as well as the sensitivity to contrast agent detection. We demonstrated that focused super-resolution approaches may not require phase aberration correction. Phase aberration was explored experimentally and $in\ silico$ and even though it resulted in measurable contrast agent detectability improvement, it was not necessary for the feasibility of transcranial super-resolution imaging through a temporal window.

APPENDIX A: PUBLICATIONS AND CONFERENCE PARTICIPATION

In the duration of this degree the following peer reviewed publications and conference proceedings were produced:

1. D. Espíndola, F. Lin, D.E. Soulioti, G.F. Pinton, Adaptive beamforming contrast enhanced super resolution imaging for improved sensitivity and resolution in deep tissues, Conference: Ultrasonics Symposium (IUS), 2017 IEEE International At: Washington, DC, USA, USA

2. D. Espíndola, F. Lin, D.E. Soulioti, G.F. Pinton, Adaptive Multifocus Beamforming for Contrast-Enhanced-Super-Resolution Ultrasound Imaging in Deep Tissue, IEEE transactions on ultrasonics, ferroelectrics, and frequency control, PP(99):1-1, 2018

3. D.E. Soulioti, D. Espíndola, P.A. Dayton, G.F. Pinton, Super-Resolution Imaging Through the Human Skull, IEEE Trans Ultrason Ferroelectr Freq Control. 2020 Jan;67(1):25-36, 2020

4. D.E. Soulioti, O. Ostras, G.F. Pinton, Diagnostic ultrasound imaging of the lung: A simulation approach based on propagation and reverberation in the human body, The Journal of the Acoustical Society of America 150, 3904, 2021 (co-first author)

5. D.E. Soulioti, F. Santibanez, G.F. Pinton, Deconstruction and reconstruction of degrading effects in ultrasound imaging: aberration, multiple reverberation, and trailing reverberation, (Submitted), 2022

The work ”Deconstruction and reconstruction of image-degrading effects in the human abdomen using Fullwave: phase aberration, multiple reverberation, and trailing reverberation” was presented during Ultrasonics Symposium (IUS), 2021 IEEE International was nominated as a finalist for the best student paper competition.

Other published work includes co-authorship of D.E. Soulioti alongside G.F. Pinton and Guillaume Renaud (Department of Imaging Physics, Delft University of Technology, The Netherlands, g.g.j.renaud@tudelft.nl) in a book chapter entitled ”Sources of image degradation and their correction in single-sided ultrasound imaging of heterogeneous tissues”, under editor review for publication under the title ”Innovative Ultrasound Imaging Techniques for biomedical applications”.

BIBLIOGRAPHY

[1] F A. Duck. *Physical Properties Of Tissue: A Comprehensive Reference Book*. Elsevier, 01 1990.

[2] D. Ackermann and G. Schmitz. Detection and tracking of multiple microbubbles in ultrasound B-Mode images. *IEEE Transactions on Ultrasonics, Ferroelectrics, and Frequency Control*, 63(1):72–82, Jan 2016.

[3] Dimitri Ackermann and Georg Schmitz. Detection and tracking of multiple microbubbles in ultrasound b-mode images. *IEEE transactions on ultrasonics, ferroelectrics, and frequency control*, 63(1):72–82, 2016.

[4] R Aljondi and S Alghamdi. Diagnostic value of imaging modalities for covid-19: Scoping review. *J Med Internet Res*, 22(8):e19673, 2020.

[5] Scott Almquist, Dennis L. Parker, and Douglas A. Christensen. Rapid full-wave phase aberration correction method for transcranial high-intensity focused ultrasound therapies. *Journal of Therapeutic Ultrasound*, 4(1):30, Dec 2016.

[6] Y Amatya, J Rupp, FM Russell, J Saunders, B Bales, and House DR. Diagnostic use of lung ultrasound compared to chest radiograph for suspected pneumonia in a resource-limited setting. *Int J Emerg Med.*, 11(1):8, 2018.

[7] C. D. Arvanitis, G. T. Clement, and N. McDannold. Transcranial assessment and visualization of acoustic cavitation: Modeling and experimental validation. *IEEE Transactions on Medical Imaging*, 34(6):1270–1281, June 2015.

[8] J-F Aubry, M Pernot, F Marquet, M Tanter, and M Fink. Transcostal high-intensity-focused ultrasound: ex vivo adaptive focusing feasibility study. *Physics in Medicine & Biology*, 53(11):2937, 2008.

[9] J.-F. Aubry, M. Tanter, M. Pernot, J.-L. Thomas, and M. Fink. Experimental demonstration of noninvasive transskull adaptive focusing based on prior computed tomography scans. *The Journal of the Acoustical Society of America*, 113(1):84–93, 2003.

[10] A. Bar-Zion, C. Tremblay-Darveau, O. Solomon, D. Adam, and Y. C. Eldar. Fast vascular ultrasound imaging with enhanced spatial resolution and background rejection. *IEEE Transactions on Medical Imaging*, 36(1):169–180, Jan 2017.

[11] Jeremy Bercoff, Gabriel Montaldo, Thanasis Loupas, David Savery, Fabien Meziere, Mathias Fink, , and Mickael Tanter. Ultrafast compound doppler imaging: providing full blood flow characterization. *IEEE Trans Ultrason Ferroelectr Freq Control*, 58:134–147, 2011.

[12] E Betzig, G H Patterson, R Sougrat, O W Lindwasser, S Olenych, J S Bonifacino, M V Davidson, J Lippincott-Schwartz, and H F Hess. Imaging intracellular fluorescent proteins at nanometer resolution. *Science*, 313:1642–1645, 2006.

[13] Anneloes E. Bohte, Bart G. P. Koot, Olga H. van der Baan-Slootweg, Tammo H. Pels Rijcken, Jochem R. van Werven, Shandra Bipat, Aart J. Nederveen, Peter L. M. Jansen, Marc A. Benninga, and Jaap Stoker. Us cannot be used to predict the presence or severity of hepatic steatosis in severely obese adolescents. *Radiology*, 262(1):327–334, 2012. PMID: 22106358.

[14] Nick Bottenus, Gianmarco Pinton, and Gregg Trahey. The impact of acoustic clutter on large array abdominal imaging. *IEEE transactions on ultrasonics, ferroelectrics, and frequency control*, 2019.

[15] Deborah D. Brahee, Chinwe Ogedegbe, Cynthia Hassler, Themba Nyirenda, Vikki Hazelwood, Herman Morchel, Rita S. Patel, and Joseph Feldman. Body mass index and abdominal ultrasound image quality: A pilot survey of sonographers. *Journal of Diagnostic Medical Sonography*, 29(2):66–72, 2013.

[16] E Brogi, E Bignami, A Sidoti, M Shawar, L Gargani, L Vetrugno, G Volpicelli, and F Forfori. Could the use of bedside lung ultrasound reduce the number of chest x-rays in the intensive care unit? *Cardiovasc Ultrasound*, 15(1):23, 2017.

[17] J Cardenas-Garcia, PH Mayo, and E Folch. Ultrasonographic evaluation of the pleura. *PLEURA*, pages 1–11, 2015.

[18] Sandhya Chandrasekaran, Bharat Tripathi, David Espındola, and Gianmarco Pinton. Modeling ultrasound propagation in the moving brain: applications to shear shock waves and traumatic brain injury. *arXiv, 2003.06446*, 2020.

[19] K. Christensen-Jeffries, R. J. Browning, M. Tang, C. Dunsby, and R. J. Eckersley. In vivo acoustic super-resolution and super-resolved velocity mapping using microbubbles. *IEEE Transactions on Medical Imaging*, 34(2):433–440, Feb 2015.

[20] K Christensen-Jeffries, O Couture, PA Dayton, YC Eldar, K Hynynen, F Kiessling, GF Pinton, G Schmitz, M Tang, M Tanter, and R van Sloun. Super-resolution ultrasound imaging. *Ultrasound Med Biol.*, 46(4):865–891, 2020.

[21] K. Christensen-Jeffries, S. Harput, J. Brown, P. N. T. Wells, P. Aljabar, C. Dunsby, M. Tang, and R. J. Eckersley. Microbubble axial localization errors in ultrasound super-resolution imaging. *IEEE Transactions on Ultrasonics, Ferroelectrics, and Frequency Control*, 64(11):1644–1654, Nov 2017.

[22] T. Christopher and K.J. Parker. New approaches to nonlinear diffractive field propagation. *J Acoust Soc Am*, 90:488–499, 1991.

[23] G.T. Clement and K. Hynynen. Micro-receiver guided transcranial beam steering. *IEEE Transactions on Ultrasonics, Ferroelectrics, and Frequency Control*, 49(4):447–453, 2002.

[24] R Copetti, G Soldati, and P Copetti. Chest sonography: a useful tool to differentiate acute cardiogenic pulmonary edema from acute respiratory distress syndrome. *Cardiovasc Ultrasound*, pages 6–16, 2008.

[25] R. Courant, Friedrichs K, and Lewy H. Über die partiellen differenzengleichungen der mathematischen physik. *Mathematische Annalen*, 100:32–74, 1928.

[26] Olivier Couture, Benoit Besson, Gabriel Montaldo, Mathias Fink, and Mickael Tanter. Microbubble ultrasound super-localization imaging (musli). In *Ultrasonics Symposium (IUS), 2011 IEEE International*, pages 1285–1287. IEEE, 2011.

[27] Olivier Couture, Benoit Besson, Gabriel Montaldo, Mathias Fink, and Mickael Tanter. Microbubble ultrasound super-localization imaging (MUSLI). In *Ultrasonics Symposium (IUS), 2011 IEEE International*, pages 1285–1287. IEEE, 2011.

[28] Franck Dagrau, Mathieu Renier, Regis Marchiano, and Francois Coulouvrat. Acoustic shock wave propagation in a heterogeneous medium: A numerical simulation beyond the parabolic approximation. *J Acoust Soc Am*, 130(1):20–32, 2011.

[29] J. J. Dahl, M Jakovljevic, Gf Pinton, and GE. Trahey. Harmonic spatial coherence imaging: an ultrasonic imaging method based on backscatter coherence. *IEEE Trans Ultrason Ferroelectr Freq Control.*, 59(4):648–659, 2012.

[30] J. J. Dahl, S. A. McAleavey, G. F. Pinton, M. S. Soo, and G. E. Trahey. Adaptive imaging on a diagnostic ultrasound scanner at quasi real-time rates. *IEEE transactions on ultrasonics, ferroelectrics, and frequency control*, pages 1832–1843, 2006.

[31] Jeremy J Dahl, Marko Jakovljevic, Gianmarco F Pinton, and Gregg E Trahey. Harmonic spatial coherence imaging: An ultrasonic imaging method based on backscatter coherence. *IEEE transactions on ultrasonics, ferroelectrics, and frequency control*, 59(4):648–659, 2012.

[32] Kazuyuki Dei, Adam Luchies, and Brett Byram. ADMIRE applied to fundamental and harmonic data acquired using a modern clinical platform. In Neb Duric and Brett C. Byram, editors, *Medical Imaging 2018: Ultrasonic Imaging and Tomography*, volume 10580, pages 75 – 83. International Society for Optics and Photonics, SPIE, 2018.

[33] C. Demené, T. Deffieux, M. Pernot, B. Osmanski, V. Biran, J. Gennisson, L. Sieu, A. Bergel, S. Franqui, J. Correas, I. Cohen, O. Baud, and M. Tanter. Spatiotemporal clutter filtering of ultrafast ultrasound data highly increases doppler and fUltrasound sensitivity. *IEEE Transactions on Medical Imaging*, 34(11):2271–2285, Nov 2015.

[34] C Demene, T Deffieux, M Pernot, B-F Osmanski, V Biran, S Franqui, J-M Correas, I Cohen, O Baud, and M Tanter. Spatiotemporal clutter filtering of ultrafast ultrasound data highly increases doppler and fultrasound sensitivity. *IEEE Trans Med Imaging*, 34:2271–85, 2015.

[35] L Demi, M Demi, R Prediletto, and G Soldati. Real-time multi-frequency ultrasound imaging for quantitative lung ultrasound - first clinical results. *J Acoust Soc Am.*, 148(2):998–1006, 2020.

[36] Libertario Demi, Thomas Egan, and Marie Muller. Lung ultrasound imaging, a technical review. *Applied Sciences*, 10(2), 2020.

[37] Libertario Demi, Thomas Egan, and Marie Muller. Lung ultrasound imaging, a technical review. *Applied Sciences*, 10(2):462, 2020.

[38] Libertario Demi, Wim van Hoeve, Ruud JG van Sloun, Gino Soldati, and Marcello Demi. Determination of a potential quantitative measure of the state of the lung using lung ultrasound spectroscopy. *Scientific reports*, 7(1):1–7, 2017.

[39] Y Desailly, O Couture, M Fink, and M Tanter. Sono-activated ultrasound localization microscopy. *Appl Phys Lett*, 103:174107, 2013.

[40] Y. Desailly, J. Pierre, O. Couture, and M. Tanter. Resolution limits of ultrafast ultrasound localization microscopy. *Phys. Med. Biol.*, 60:8723, Oct. 2015.

[41] Yann Desailly, Olivier Couture, Mathias Fink, and Mickael Tanter. Sono-activated ultrasound localization microscopy. *Applied Physics Letters*, 103(17):174107, 2013.

[42] M Di Serafino, M Notaro, F Iacobellis, V Delli Paoli, C Acampora, S Ianniello, L Brunese, L Romano, and G Vallone. The lung ultrasound: facts or artifacts? in the era of covid-19 outbreak. *Radiol Med.*, 125(8):738–753, 2020.

[43] CF Dietrich, G Mathis, M Blaivas, G Volpicelli, A Seibel, D Wastl, NS Atkinson, XW Cui, M Fan, and D Yi. Lung b-line artefacts and their use. *Journal of thoracic disease*, 8(6):1356–1365, 2016.

[44] Bei Ding, Hua-wei Ling, and Yong Zhang. Pattern of cerebral hyperperfusion in Alzheimer's disease and amnestic mild cognitive impairment using voxel-based analysis of 3D arterial spin-labeling imaging: Initial experience. *Clinical Interventions in Aging*, (9):493–500, 2014.

[45] Bin Du, Jinyan Wang, Haoteng Zheng, Chenhui Xiao, Siyuan Fang, Minhua Lu, and Rui Mao. A novel transcranial ultrasound imaging method with diverging wave transmission and deep learning approach. *Computer Methods and Programs in Biomedicine*, 186:105308, 2020.

[46] F.A. Duck. *Physical properties of tissue: a comprehensive reference book*. Academic Press, London, UK, 1990.

[47] C Errico, J Pierre, S Pezet, Y Desailly, Z Lenkei, O Couture, and M Tanter. Ultrafast ultrasound localization microscopy for deep super-resolution vascular imaging. *Nature*, 527:499–502, 2015.

[48] David Espíndola, Stephen Lee, and Gianmarco Pinton. Shear shock waves observed in the brain. *Physical Review Applied*, 8(4):044024, 2017.

[49] D. Espíndola, F. Lin, D. E. Soulioti, P. A. Dayton, and G. F. Pinton. Adaptive multifocus beamforming for contrast-enhanced-super-resolution ultrasound imaging in deep tissue. *IEEE Transactions on Ultrasonics, Ferroelectrics, and Frequency Control*, 65(12):2255–2263, Dec 2018.

[50] Mustapha A. Ezzeddine, Michael H. Lev, Colin T. McDonald, Guy Rordorf, Jamary Oliveira-Filho, Fatma Gul Aksoy, Jeffrey Farkas, Alan Z. Segal, Lee H. Schwamm, R. Gilberto Gonzalez, and Walter J. Koroshetz. CT angiography with whole brain perfused blood volume imaging. *Stroke*, 33(4):959–966, 2002.

[51] S Feingold, R Gessner, I M Guracar, and P A Dayton. Quantitative volumetric perfusion mapping of the microvasculature using contrast ultrasound. *Investigative radiology*, 45:669–674, 2010.

[52] M. Fink. Time reversal of ultrasonic fields - part i: Basic principles. *IEEE transactions on ultrasonics, ferroelectrics, and frequency control*, 39(5):555–56, 1992.

[53] S. W. Flax and M. O'Donnell. Phase-aberration correction using signals from point reflectors and diffuse scatterers: Basic principles. *IEEE transactions on ultrasonics, ferroelectrics, and frequency control*, 35(6):758–767, 1988.

[54] S. W. Flax and M. O'Donnell. Phase aberration correction in medical ultrasound using speckle brightness as a quality factor. *J Acoust Soc Am*, 85(5):1819–1833, 1989.

[55] J Folkman. Tumor angiogenesis: therapeutic implications. *N Engl J Med*, 285:1182–1186, 1971.

[56] F Frassi, A Pingitore, D Cialoni, and E Picano. Chest sonography detects lung water accumulation in healthy elite apnea divers. *J Am Soc Echocardiogr*, 21(10):1150–5, 2008.

[57] L Gargani and G Volpicelli. How i do it: lung ultrasound. *Cardiovasc Ultrasound*, 12:25, 2014.

[58] R C Gessner, S R Aylward, and P A Dayton. Mapping microvasculature with acoustic angiography yields quantifiable differences between healthy and tumor-bearing tissue volumes in a rodent model. *Radiology*, 264:733–740, 2012.

[59] R C Gessner, M Lukacs, M Lee, E Cherin, F S Foster, and P A Dayton. High-resolution, high-contrast ultrasound imaging using a prototype dual-frequency transducer: in vitro and in vivo studies. *IEEE Trans Ultrason Ferroelectr Freq Control*, 57:1772–1781, 2010.

[60] A Goffi, R Kruisselbrink, and G Volpicelli. The sound of air: point-of-care lung ultrasound in perioperative medicine. *Can J Anesth/J Can Anesth*, 65:399–416, 2018.

[61] Philip B. Gorelick, Angelo Scuteri, Sandra E. Black, Charles DeCarli, Steven M. Greenberg, Costantino Iadecola, Lenore J. Launer, Stephane Laurent, Oscar L. Lopez, David Nyenhuis, Ronald C. Petersen, Julie A. Schneider, Christophe Tzourio, Donna K. Arnett, David A. Bennett, Helena C. Chui, Randall T. Higashida, Ruth Lindquist, Peter M. Nilsson, Gustavo C. Roman, Frank W. Sellke, and Sudha Seshadri. Vascular contributions to cognitive impairment and dementia. *Stroke*, 42(9):2672–2713, 2011.

[62] S. A. Goss, R. L. Johnston, and F. Dunn. Comprehensive compilation of empirical ultrasonic properties of mammalian tissues. *The Journal of the Acoustical Society of America*, 64(2):423–457, 1978.

[63] Jian Guan, Michael Karsy, Scott McNally, Adam de Havenon, M. Yashar S. Kalani, Philipp Taussky, Seong-Eun Kim, and Min S. Park. High-resolution magnetic resonance imaging of intracranial aneurysms treated by flow diversion. *Interdisciplinary Neurosurgery*, 10:69 – 74, 2017.

[64] D Hanahan and R A Weinberg. The hallmarks of cancer. *Cell*, 100:57–70, 2000.

[65] S. Harput, K. Christensen-Jeffries, J. Brown, Y. Li, K. J. Williams, A. H. Davies, R. J. Eckersley, C. Dunsby, and M. Tang. Two-stage motion correction for super-resolution ultrasound imaging in human lower limb. *IEEE Transactions on Ultrasonics, Ferroelectrics, and Frequency Control*, 65(5):803–814, May 2018.

[66] WR Hedrick, DL Hykes, and DE Starchman. *Ultrasound physics and instrumentation 4th ed.* Elsevier Mosby, St. Louis, MO, 2005.

[67] Thomas J. Hudson, Thomas Looi, Samuel Pichardo, Joao Amaral, Michael Temple, James M. Drake, and Adam C. Waspe. Simulating thermal effects of MR-guided focused ultrasound in cortical bone and its surrounding tissue. *Medical Physics*, 45(2):506–519, 2017.

[68] J. Huijssen and M. D. Verweij. An iterative method for the computation of nonlinear, wide-angle, pulsed acoustic fields of medical diagnostic transducers. *The Journal of the Acoustical Society of America*, 127(1):33–44, 2010.

[69] K. Hynynen and F.A. Jolesz. Demonstration of potential noninvasive ultrasound brain therapy through an intact skull. *ltrasound Med Biol.*, 24(2):275–83, 1998.

[70] Kullervo Hynynen and Ferenc A Jolesz. Demonstration of potential noninvasive ultrasound brain therapy through an intact skull. *Ultrasound in Medicine & Biology*, 24(2):275 – 283, 1998.

[71] N. M. Ivancevich, J. J. Dahl, G. E. Trahey, and S. W. Smith. Phase-aberration correction with a 3-D ultrasound scanner: feasibility study. *IEEE Transactions on Ultrasonics, Ferroelectrics, and Frequency Control*, 53(8):1432–1439, Aug 2006.

[72] NM Ivancevich, GF Pinton, HA Nicoletto, E Bennett, DT Laskowitz, and SW Smith. Real-time 3-d contrast-enhanced transcranial ultrasound and aberration correction. *Ultrasound Med Biol.*, 34(9):1387–1395, 2008.

[73] J. A. Jensen. Field: A program for simulating ultrasound systems. *Med. Biol. Eng. Comp., col. 10th Nordic-Baltic Conference on Biomedical Imaging*, 4(1):351–353, 1996.

[74] J.A. Jensen and N.B.. Svendsen. Calculation of pressure fields from arbitrarily shaped, apodized, and excited ultrasound transducers. *IEEE Trans. Ultrason. Ferroelectr. Freq. Control*, 39(2):262–267, 1992.

[75] Vaibhav Kakkad, Jeremy Dahl, Sarah Ellestad, and Gregg Trahey. In vivo application of short-lag spatial coherence and harmonic spatial coherence imaging in fetal ultrasound. *Ultrasonic Imaging*, 37(2):101–116, 2015. PMID: 25116292.

[76] Manjush Karthika, Duane Wong, Suresh G Nair, Lalitha V Pillai, and Chris Sara Mathew. Lung ultrasound: The emerging role of respiratory therapists. *Respiratory Care*, 64(2):217–229, 2019.

[77] Jonathan D. Kirsch, Mahan Mathur, Michele H. Johnson, Gunabushanam Gowthaman, and Leslie M. Scoutt. Advances in transcranial doppler us: Imaging ahead. *RadioGraphics*, 33(1):E1–E14, 2013. PMID: 23322845.

[78] SJ Koenig, M Narasimhan, and PH Mayo. Thoracic ultrasonography for the pulmonary specialist. *Chest*, 140(5):1332–1341, 2011.

[79] Muyinatu A. Lediju, Gregg E. Trahey, Brett C. Byram, and Jeremy J. Dahl. Short-lag spatial coherence of backscattered echoes: imaging characteristics. *IEEE Transactions on Ultrasonics, Ferroelectrics, and Frequency Control*, 58(7):1377–1388, 2011.

[80] Muyinatu A. Lediju, Gregg E. Trahey, Brett C. Byram, and Jeremy J. Dahl. Short-lag spatial coherence of backscattered echoes: imaging characteristics. *IEEE Transactions on Ultrasonics, Ferroelectrics, and Frequency Control*, 58(7):1377–1388, 2011.

[81] DA Lichtenstein and Y Menu. A bedside ultrasound sign ruling out pneumothorax in the critically ill. lung sliding. *Chest*, 108(5):1345–1348, 1995.

[82] Daniel A Lichtenstein. Lung ultrasound in the critically ill. *Annals of intensive care*, 4(1):1–12, 2014.

[83] F Lin, J D Rojas, and P A Dayton. Super resolution contrast ultrasound imaging: Analysis of imaging resolution and application to imaging tumor angiogenesis. *IEEE Int Ultrason Symp*, pages 1–4, 2016.

[84] F Lin, S E Shelton, D Espíndola, J D Rojas, G Pinton, and P A Dayton. 3-d ultrasound localization microscopy for identifying microvascular morphology features of tumor angiogenesis at a resolution beyond the diffraction limit of conventional ultrasound. *Theranostics*, 7:196, 2017.

[85] F Lin, J K Tsuruta, J D Rojas, and P A Dayton. Optimizing sensitivity of ultrasound contrast-enhanced super-resolution imaging by tailoring size distribution of microbubble contrast agent. *Ultrasound in Medicine & Biology*, 2017.

[86] Fanglue Lin, James K. Tsuruta, Juan D. Rojas, and Paul A. Dayton. Optimizing sensitivity of ultrasound contrast-enhanced super-resolution imaging by tailoring size distribution of microbubble contrast agent. *Ultrasound in Medicine & Biology*, 43(10):2488 – 2493, 2017.

[87] B. D. Lindsey, E. D. Light, H. A. Nicoletto, E. R. Bennett, D. T. Laskowitz, and S. W. Smith. The ultrasound brain helmet: new transducers and volume registration for in vivo simultaneous multi-transducer 3-D transcranial imaging. *IEEE Transactions on Ultrasonics, Ferroelectrics, and Frequency Control*, 58(6):1189–1202, June 2011.

[88] B. D. Lindsey and S. W. Smith. Pitch-catch phase aberration correction of multiple isoplanatic patches for 3-D transcranial ultrasound imaging. *IEEE Transactions on Ultrasonics, Ferroelectrics, and Frequency Control*, 60(3):463–480, March 2013.

[89] Brooks D. Lindsey and Stephen W. Smith. Refraction correction in 3d transcranial ultrasound imaging. *Ultrasonic Imaging*, 36(1):35–54, 2014. PMID: 24275538.

[90] Brooks D. Lindsey and Stephen W. Smith. Refraction correction in 3D transcranial ultrasound imaging. *Ultrasonic Imaging*, 36(1):35–54, 2014. PMID: 24275538.

[91] D.-L. Liu and R. C. Waag. Correction of ultrasonic wavefront distortion using backpropagation and a reference waveform method for time-shift compensation. *J Acoust Soc Am*, 36(2):649–660, 1994.

[92] Dong-Lai Liu and R.C. Waag. A comparison of ultrasonic wavefront distortion and compensation in one-dimensional and two-dimensional apertures. *IEEE Transactions on Ultrasonics, Ferroelectrics, and Frequency Control*, 42(4):726–733, 1995.

[93] W. Long, N. Bottenus, and G. E. Trahey. Lag-one coherence as a metric for ultrasonic image quality. *IEEE Transactions on Ultrasonics, Ferroelectrics, and Frequency Control*, 65(10):1768–1780, 2018.

[94] N. F. Maklad, J. Ophir, and V. Balsara. Attenuation of ultrasound in normal liver and diffuse liver disease in vivo. *Ultrasonic Imaging*, 6(2):117–125, 1984. PMID: 6539974.

[95] Raoul Mallart and Mathias Fink. Improved imaging rate through simultaneous transmission of several ultrasound beams. In *New Developments in Ultrasonic Transducers and Transducer Systems*, volume 1733, pages 120–131. International Society for Optics and Photonics, 1992.

[96] R. Mallert and M. Fink. The van cittert-zernike theorem in pulsed ultrasound-implications for ultrasonic imaging. In *IEEE Symposium on Ultrasonics*, pages 1603–1607 vol.3, 1990.

[97] F Marquet, M Pernot, J-F Aubry, G Montaldo, L Marsac, M Tanter, and M Fink. Non-invasive transcranial ultrasound therapy based on a 3D CT scan: protocol validation and in vitro results. *Physics in Medicine & Biology*, 54(9):2597, 2009.

[98] L. Marsac, D. Chauvet, R. La Greca, A.-L. Boch, K. Chaumoitre, M. Tanter, and J.-F. Aubry. Ex vivo optimisation of a heterogeneous speed of sound model of the human skull for non-invasive transcranial focused ultrasound at 1mhz. *International Journal of Hyperthermia*, 33(6):635–645, 2017. PMID: 28540778.

[99] T. Douglas Mast. Two- and three-dimensional simulations of ultrasonic propagation through human breast tissue. *Acoustics Research Letters Online*, 3(2):53–58, 2002.

[100] T. Douglas Mast, Laura M. Hinkelman, Michael J. Orr, Victor Sparrow, and W. Robert C. Waag. Simulation of ultrasonic pulse propagation through the abdominal wall. *J Acoust Soc Am*, 102(2):1177–1190, 1997.

[101] PH Mayo, R Copetti, D Feller-Kopman, G Mathis, E Maury, S Mongodi, F Mojoli, G Volpicelli, and M Zanobetti. Thoracic ultrasonography: a narrative review. *Intensive Care Med.*, 45(9):1200–1211, 2019.

[102] Vojtech Melenovsky, Mads J. Andersen, Krystof Andress, Yogesh N. Reddy, and Barry A. Borlaug. Lung congestion in chronic heart failure: haemodynamic, clinical, and prognostic implications. *European Journal of Heart Failure*, 17(11):1161–1171, 2015.

[103] F Mento, G Soldati, R Prediletto, M Demi, and L Demi. Quantitative lung ultrasound spectroscopy applied to the diagnosis of pulmonary fibrosis: The first clinical study. *IEEE Transactions on Ultrasonics, Ferroelectrics, and Frequency Control*, 67(11):2265–2273, 2020.

[104] Federico Mento and Libertario Demi. On the influence of imaging parameters on lung ultrasound b-line artifacts, in vitro study. *The Journal of the Acoustical Society of America*, 148(2):975–983, 2020.

[105] Federico Mento, Tiziano Perrone, Veronica Narvena Macioce, Francesco Tursi, Danilo Buonsenso, Elena Torri, Andrea Smargiassi, Riccardo Inchingolo, Gino Soldati, and Libertario Demi. On the impact of different lung ultrasound imaging protocols in the evaluation of patients affected by coronavirus disease 2019. *Journal of Ultrasound in Medicine*, n/a(n/a).

[106] H Günhan Akarça1 Michael Jaeger, Elise Robinson and Martin Frenz. Full correction for spatially distributed speed-of-sound in echo ultrasound based on measuring aberration delays via transmit beam steering. *Physics in Medicine & Biology*, 60:4497, 2015.

[107] Marcelo Haertel Miglioranza, Luna Gargani, Roberto Tofani Sant'Anna, Marciane Maria Rover, Vitor Magnus Martins, Augusto Mantovani, Cristina Weber, Maria Antonieta Moraes, Carlos Jader Feldman, Renato Abdala Karam Kalil, Rosa Sicari, Eugenio Picano, and Tiago Luiz Luz Leiria. Lung ultrasound for the evaluation of pulmonary congestion in outpatients. *JACC: Cardiovascular Imaging*, 6(11):1141–1151, 2013.

[108] M Miyazaki and K Kato. Measurement of cerebral blood flow by ultrasonic doppler technique. *Jpn. Circ. J.*, 29:375–382, 1965.

[109] Kaustav Mohanty, John Blackwell, Thomas Egan, and Marie Muller. Characterization of the lung parenchyma using ultrasound multiple scattering. *Ultrasound in medicine & biology*, 43(5):993–1003, 2017.

[110] F Mojoli, B Bouhemad, S Mongodi, and D Lichtenstein. Lung ultrasound for critically ill patients. *Am J Respir Crit Care Med*, 199(6):701–714, 2019.

[111] G. Montaldo, M. Tanter, J. Bercoff, N. Benech, and M. Fink. Coherent plane-wave compounding for very high frame rate ultrasonography and transient elastography. *IEEE Transactions on Ultrasonics, Ferroelectrics, and Frequency Control*, 56(3):489–506, March 2009.

[112] Moein Mozaffarzadeh, Martin D. Verweij, Verya Daeichin, Nico De Jong, and Guillaume Renaud. Transcranial ultrasound imaging with estimating the geometry, position and wave-speed of temporal bone. In *2021 IEEE International Ultrasonics Symposium (IUS)*, pages 1–4, 2021.

[113] T.G. Muir and E.L. Carstensen. Prediction of nonlinear acoustic effects at biomedical frequencies and intensities. *Ultrasound in Medicine & Biology*, 6:345–357, 1980.

[114] Francisco MJ Neto, A Junior Rahal, FA Vieira, PS Silva, and MB Funari. Advances in lung ultrasound. *Einstein*, 14(3):443–448, 2016.

[115] G. C. Ng, S. S. Worrell, P. D. Freiburger, and G. E. Trahey. A comparative evaluation of several algorithms for phase aberration correction. *IEEE transactions on ultrasonics, ferroelectrics, and frequency control*, 41(5):631–643, 1994.

[116] Levin Nock, Gregg E. Trahey, and Stephen W. Smith. Phase aberration correction in medical ultrasound using speckle brightness as a quality factor. *The Journal of the Acoustical Society of America*, 85(5):1819–1833, 1989.

[117] G.V. Norton and J.C. Novarini. Including dispersion and attenuation directly in the time domain for wave propagation in isotropic media. *The Journal of the Acoustical Society of America*, 113(6):3024–3031, 2003.

[118] M Ochs, JR Nyengaard, A Jung, L Knudsen, M Voigt, T Wahlers, J Richter, and HJ Gundersen. The number of alveoli in the human lung. *Am J Respir Crit Care Med*, 169:120–124, 2004.

[119] Tatjana Opacic, Stefanie Dencks, Benjamin Theek, Marion Piepenbrock, Dimitri Ackermann, Anne Rix, Twan Lammers, Elmar Stickeler, Stefan Delorme, Georg Schmitz, and Fabian Kiessling. Motion model ultrasound localization microscopy for preclinical and clinical multiparametric tumor characterization. *Nature Communications*, 9(1527), 2018.

[120] MA O′Reilly and K Hynynen. A super-resolution ultrasound method for brain vascular mapping. *Med Phys*, 40:110701, 2013.

[121] A.Michael Parfitt. Trabecular bone architecture in the pathogenesis and prevention of fracture. *The American Journal of Medicine*, 82(1, Supplement 2):68 – 72, 1987. Medical Management of Cardiovascular Hypertensive, and Metabolic.

[122] M. S. Patterson and F. S. Foster. The improvement and quantitative assessment of b-mode images produced by an annular array/cone hybrid. *Ultrasonic Imaging*, 5(3):195–213, 1983. PMID: 6356553.

[123] M. S. Patterson and F. S. Foster. The improvement and quantitative assessment of b-mode images produced by an annular array/cone hybrid. *Ultrasonic Imaging*, 5(3):195–213, 1983.

[124] M Pernot, J-F Aubry, M Tanter, J-L Thomas, and M Fink. High power transcranial beam steering for ultrasonic brain therapy. *Physics in Medicine & Biology*, 48(16):2577, 2003.

[125] T Perrone, G Soldati, L Padovini, A Fiengo, G Lettieri, U Sabatini, G Gori, F Lepore, M Garolfi, I Palumbo, R Inchingolo, A Smargiassi, L Demi, EE Mossolani, F Tursi, C Klersy, and A Di Sabatino. A new lung ultrasound protocol able to predict worsening in patients affected by severe acute respiratory syndrome coronavirus 2 pneumonia. *J Ultrasound Med*, 2020.

[126] E Peschiera, F Mento, and L Demi. Numerical study on lung ultrasound b-line formation as a function of imaging frequency and alveolar geometries. *J Acoust Soc Am.*, 149(4):2304, 2021.

[127] E Picano and PA Pellikka. Ultrasound of extravascular lung water: a new standard for pulmonary congestion. *Eur Heart J*, 37(27):2097–2104, 2016.

[128] G. Pinton, J.-F. Aubry, E. Bossy, M. Muller, M. Pernot, and M. Tanter. Attenuation, scattering, and absorption of ultrasound in the skull bone. *Medical Physics*, 39(1):299–307, 2011.

[129] G. Pinton, J. Dahl, S. Rosenzweig, and G. Trahey. A heterogeneous nonlinear attenuating full-wave model of ultrasound. *Ultrasonics, Ferroelectrics and Frequency Control, IEEE Transactions on*, 56(3):474–488, 2009.

[130] G. Pinton, M. Pernot, E. Bossy, J. Aubry, M. Muller, and M. Tanter. Mechanisms of attenuation and heating dissipation of ultrasound in the skull bone: Comparison between simulation models and experiments. In *2010 IEEE International Ultrasonics Symposium*, pages 225–228, Oct 2010.

[131] G. Pinton, G. E. Trahey, and J. Dahl. Sources of image degradation in fundamental and harmonic ultrasound imaging using nonlinear, full-wave simulations. *IEEE Transactions on Ultrasonics, Ferroelectrics, and Frequency Control*, 58(4):754–765, April 2011.

[132] G. F. Pinton, J. Aubry, and M. Tanter. Direct phase projection and transcranial focusing of ultrasound for brain therapy. *IEEE Transactions on Ultrasonics, Ferroelectrics, and Frequency Control*, 59(6):1149–1159, June 2012.

[133] G. F. Pinton, J. J. Dahl, and G. E. Trahey. Impact of clutter levels on spatial covariance: Implications for imaging. *In Proc IEEE Ultrason Symp*, page 2171–2174, 2010.

[134] G. F. Pinton, G. E. Trahey, and J. J. Dahl. Erratum: Sources of image degradation in fundamental and harmonic ultrasound imaging: a nonlinear, full-wave, simulation study [apr 11 754-765]. *IEEE Transactions on Ultrasonics, Ferroelectrics, and Frequency Control*, 58(6):1272–1283, June 2011.

[135] G. F. Pinton, G. E. Trahey, and J. J. Dahl. Sources of image degradation in fundamental and harmonic ultrasound imaging using nonlinear, full-wave simulations. *IEEE Transactions on Ultrasonics, Ferroelectrics, and Frequency Control*, 58(4):754–765, April 2011.

[136] G. F. Pinton, G. E. Trahey, and J. J. Dahl. Spatial coherence in human tissue: implications for imaging and measurement. *IEEE transactions on ultrasonics, ferroelectrics, and frequency control*, 61(12):1976–1987, 2014.

[137] Gianmarco Pinton. Fullwave simulations of ultrasound propagation in the human body: Applications to imaging and motion estimation. *The Journal of the Acoustical Society of America*, 141(5):3547–3547, 2017.

[138] Gianmarco Pinton. Ultrasound imaging of the human body with three dimensional full-wave nonlinear acoustics. part 1: simulations methods. *IEEE Transactions on Ultrasonics, Ferroelectrics, and Frequency Control (Under revision)*, 2018.

[139] Gianmarco Pinton. Ultrasound imaging of the human body with three dimensional full-wave nonlinear acoustics. part 2: sources of image degradation in intercostal imaging. *IEEE Transactions on Ultrasonics, Ferroelectrics, and Frequency Control (Under revision)*, 2018.

[140] Gianmarco Pinton. Ultrasound imaging of the human body with three dimensional full-wave nonlinear acoustics. part 1: simulations methods. *arXiv, 2003.06934*, 2020.

[141] Gianmarco Pinton. Ultrasound imaging of the human body with three dimensional full-wave nonlinear acoustics. part 1: simulations methods, 2020.

[142] Gianmarco Pinton. Ultrasound imaging with three dimensional full-wave nonlinear acoustic simulations. part 2: sources of image degradation in intercostal imaging. *arXiv, 2003.06927*, 2020.

[143] Gianmarco Pinton. A fullwave model of the nonlinear wave equation with multiple relaxations and relaxing perfectly matched layers for high-order numerical finite-difference solutions, 2021.

[144] Gianmarco Pinton, Jean-Francois Aubry, Mathias Fink, and Mickael Tanter. Effects of nonlinear ultrasound propagation on high intensity brain therapy. *Medical physics*, 38(3):1207–1216, 2011.

[145] Gianmarco Pinton, Jean-Francois Aubry, Mathias Fink, and Mickael Tanter. Effects of nonlinear ultrasound propagation on high intensity brain therapy. *Medical Physics*, 38(3):1207–1216, 2011.

[146] Gianmarco Pinton, Jean-Francois Aubry, Mathias Fink, and Mickael Tanter. Numerical prediction of frequency dependent 3d maps of mechanical index thresholds in ultrasonic brain therapy. *Medical physics*, 39(1):455–467, 2012.

[147] Gianmarco Pinton, Mathieu Pernot, Emmanuel Bossy, Jean-François Aubry, Marie Muller, and Mickaël Tanter. Attenuation, scattering and absorption of ultrasound in the skull bone. *Medical Physics*, pages 455–467, 2011.

[148] Gianmarco F Pinton. A fullwave model of the nonlinear wave equation with multiple relaxations and relaxing perfectly matched layers for high-order numerical finite-difference solutions. *Arxiv*, 2021.

[149] Gianmarco F Pinton, Jean-Francois Aubry, and Mickael Tanter. Direct phase projection and transcranial focusing of ultrasound for brain therapy. *IEEE transactions on ultrasonics, ferroelectrics, and frequency control*, 59(6):1149–1159, 2012.

[150] Gianmarco F. Pinton, Jeremy Dahl, Stephen Rosenzweig, and Gregg E. Trahey. A heterogeneous nonlinear attenuating full- wave model of ultrasound. *IEEE Transactions on Ultrasonics, Ferroelectrics, and Frequency Control*, 56(3):474–488, March 2009.

[151] Gianmarco F Pinton, Jeremy Dahl, Stephen Rosenzweig, and Gregg E Trahey. A heterogeneous nonlinear attenuating full-wave model of ultrasound. *IEEE transactions on ultrasonics, ferroelectrics, and frequency control*, 56(3):474–488, 2009.

[152] Gianmarco F. Pinton, Jeremy Dahl, and Gregg Trahey. Clutter and sources of image degradation in fundamental and harmonic ultrasound imaging. In *2009 IEEE International Ultrasonics Symposium*, pages 2300–2303, 2009.

[153] Gianmarco F Pinton, Gregg E Trahey, and Jeremy J Dahl. Sources of image degradation in fundamental and harmonic ultrasound imaging using nonlinear, full-wave simulations. *IEEE transactions on ultrasonics, ferroelectrics, and frequency control*, 58(6):1272–1283, 2011.

[154] Gianmarco F Pinton, Gregg E Trahey, and Jeremy J Dahl. Spatial coherence in human tissue: Implications for imaging and measurement. *IEEE transactions on ultrasonics, ferroelectrics, and frequency control*, 61(12):1976–1987, 2014.

[155] Elke Platz, Allison A. Merz, Pardeep S. Jhund, Ali Vazir, Ross Campbell, and John J. McMurray. Dynamic changes and prognostic value of pulmonary congestion by lung ultrasound in acute and chronic heart failure: a systematic review. *European Journal of Heart Failure*, 19(9):1154–1163, 2017.

[156] Imke Puls, Daniela Berg, Mathias Mäurer, Mira Schliesser, Gerd Hetzel, and Georg Becker. Transcranial sonography of the brain parenchyma: comparison of b-mode imaging and tissue harmonic imaging. *Ultrasound in Medicine & Biology*, 26(2):189–194, 2000.

[157] R. Cobbold R. J. Zemp, J. Tavakkoli. Modeling of nonlinear ultrasound propagation in tissue from array transducers. *J Acoust Soc Am*, 113(1):139–152, 2003.

[158] A Reissig and C Kroegel. Transthoracic sonography of diffuse parenchymal lung disease: the role of comet tail artifacts. *J Ultrasound Med.*, 22(2):173–180, 2003.

[159] Guillaume Renaud, Pieter Kruizinga, Didier Cassereau, and Pascal Laugier. In vivo ultrasound imaging of the bone cortex. *Physics in Medicine & Biology*, 63(12):125010, jun 2018.

[160] K. W. Rigby, C. L. Chalek, B. H, R. S. Lewandowski Haider, M. O'Donnell, L. S. Smith, and D. G. Wildes. Impact of clutter levels on spatial covariance: Implications for imaging. *In Proc IEEE Ultrason Symp*, 2:1645–1653, 2000.

[161] C. Riva, B. Ross, and G.B. Benedek. Laser doppler measurements of blood flow in capillary tubes and retinal arteries. *Investigative Ophthalmology & Visual Science*, 11(11):936, 1972.

[162] M J Rust, M Bates, and X Zhuang. Sub-diffraction-limit imaging by stochastic optical reconstruction microscopy (storm). *Nat Methods*, 3:793–795, 2006.

[163] Sergio J. Sanabria, Marga B. Rominger, and Orcun Goksel. Speed-of-sound imaging based on reflector delineation. *IEEE Transactions on Biomedical Engineering*, 66(7):1949–1962, 2019.

[164] A Saraogi. Lung ultrasound: Present and future. *Lung India*, 32(3):250–257, 2015.

[165] S E Shelton, Y Z Lee, M Lee, E Cherin, F S Foster, S R Aylward, and P A Dayton. Quantification of microvascular tortuosity during tumor evolution using acoustic angiography. *Ultrasound Med Biol*, 41:1896–1904, 2015.

[166] Yuji Shen, Ida M. Pu, Trevor Ahearn, Matthew Clemence, and Christian Schwarzbauer. Quantification of venous vessel size in human brain in response to hypercapnia and hyperoxia using magnetic resonance imaging. *Magnetic Resonance in Medicine*, 69(6):1541–1552, 2012.

[167] M. Siepmann, G. Schmitz, J. Bzyl, M. Palmowski, and F. Kiessling. Imaging tumor vascularity by tracing single microbubbles. In *2011 IEEE International Ultrasonics Symposium*, pages 1906–1909, Oct 2011.

[168] G Soldati, M Demi, A Smargiassi, R Inchingolo, and Demi L. The role of ultrasound lung artifacts in the diagnosis of respiratory diseases. *Expert Rev Respir Med.*, 13(2):163–172, 2019.

[169] G Soldati, A Smargiassi, R Inchingolo, D Buonsenso, T Perrone, DF Briganti, S Perlini, E Torri, A Mariani, EE Mossolani, F Tursi, F Mento, and L Demi. Proposal for international standardization of the use of lung ultrasound for patients with covid-19: A simple, quantitative, reproducible method. *J Ultrasound Med*, 39(7):1413–1419, 2020.

[170] G Soldati, A Testa, FR Silva, L Carbone, G Portale, and NG Silveri. Chest ultrasonography in lung contusion. *Chest*, 130(2):533–538, 2006.

[171] Gino Soldati, Marcello Demi, Riccardo Inchingolo, Andrea Smargiassi, and Libertario Demi. On the physical basis of pulmonary sonographic interstitial syndrome. *Journal of ultrasound in medicine: official journal of the American Institute of Ultrasound in Medicine*, 35(10):2075–2086, 2016.

[172] S. Sorbi, J. Hort, T. Erkinjuntti, T. Fladby, G. Gainotti, H. Gurvit, B. Nacmias, F. Pasquier, B. O. Popescu, I. Rektorova, D. Religa, R. Rusina, M. Rossor, R. Schmidt, E. Stefanova, J. D. Warren, and P. and Scheltens. EFNS-ENS guidelines on the diagnosis and management of disorders associated with dementia. *European Journal of Neurology*, 19(9):1159–1179, 2012.

[173] D. E. Soulioti, D. Espíndola, P. A. Dayton, and G. F. Pinton. Super-resolution imaging through the human skull. *IEEE Transactions on Ultrasonics, Ferroelectrics, and Frequency Control*, 67(1):25–36, 2020.

[174] Danai E Soulioti, Francisco Santibanez, and Gianmarco F Pinton. Deconstruction and reconstruction of image-degrading effects in the human abdomen using fullwave: phase aberration, multiple reverberation, and trailing reverberation. *ArXiv*, 2021.

[175] KirkT Spencer, James Bednarz, PatrickG Rafter, Claudia Korcarz, and RobertoM Lang. Use of harmonic imaging without echocardiographic contrast to improve two-dimensional image quality. *The American Journal of Cardiology*, 82(6):794–799, 1998.

[176] V Spitzer, M Ackerman, A Scherzinger, and D Whitlock. The visible human male: a technical report. *Journal of the American Medical Informatics Association*, 3(2):118–130, 1996.

[177] Nisreen Sulayman, Moustafa Al-Mawaldi, and Qosai Kanafani. Semi-automatic detection and segmentation algorithm of saccular aneurysms in 2D cerebral DSA images. *The Egyptian Journal of Radiology and Nuclear Medicine*, 47(3):859 – 865, 2016.

[178] Yoichi Sumino and Robert C. Waag. Measurements of ultrasonic pulse arrival time differences produced by abdominal wall specimens. *The Journal of the Acoustical Society of America*, 90(6):2924–2930, 1991.

[179] Mickaël Tanter, Jean-Louis Thomas, and Mathias Fink. Focusing and steering through absorbing and aberrating layers: Application to ultrasonic propagation through the skull. *The Journal of the Acoustical Society of America*, 103(5):2403–2410, 1998.

[180] Mickaël Tanter, Jean-Louis Thomas, and Mathias Fink. Focusing and steering through absorbing and aberrating layers: Application to ultrasonic propagation through the skull. *The Journal of the Acoustical Society of America*, 103(5):2403–2410, 1998.

[181] J. L. Thomas and M. A. Fink. Ultrasonic beam focusing through tissue inhomogeneities with a time reversal mirror: application to transskull therapy. *IEEE Transactions on Ultrasonics, Ferroelectrics, and Frequency Control*, 43(6):1122–1129, Nov 1996.

[182] DM Tierney, JS Huelster, JD Overgaard, MB Plunkett, LL Boland, CA St Hill, VK Agboto, CS Smith, BF Mikel, BE Weise, KE Madigan, AP Doshi, and Melamed RR. Comparative performance of pulmonary ultrasound, chest radiograph, and ct among patients with acute respiratory failure. *Crit Care Med*, 48(2):151–157, 2020.

[183] L. Tong, H. Gao, and J. D'hooge. Multi-transmit beam forming for fast cardiac imaging-a simulation study. *IEEE Transactions on Ultrasonics, Ferroelectrics, and Frequency Control*, 60(8):1719–1731, August 2013.

[184] L. Tong, A. Ramalli, R. Jasaityte, P. Tortoli, and J. D'hooge. Multi-transmit beam forming for fast cardiac imaging - experimental validation and in vivo application. *IEEE Transactions on Medical Imaging*, 33(6):1205–1219, June 2014.

[185] G. E. Trahey, D. Zhao, J. A. Miglin, and S. W. Smith. Experimental results with a real-time adaptive ultrasonic imaging system for viewing through distorting media. *IEEE transactions on ultrasonics, ferroelectrics, and frequency control*, 37(5):418–427, 1990.

[186] G.E. Trahey, P.D. Freiburger, L.F. Nock, and D.C. Sullivan. In vivo measurements of ultrasonic beam distortion in the breast. *Ultrasonic Imaging*, 13(1):71–90, 1991.

[187] Gregg Trahey, Nick Bottenus, and Gianmarco Pinton. Beamforming methods for large aperture imaging. *The Journal of the Acoustical Society of America*, 141(5):3610–3611, 2017.

[188] F Tranquart, N Grenier, V Eder, and L Pourcelot. Clinical use of ultrasound tissue harmonic imaging. *Ultrasound in medicine & biology*, 25(6):889—894, July 1999.

[189] Bradley E Treeby and Benjamin T Cox. k-wave: Matlab toolbox for the simulation and reconstruction of photoacoustic wave fields. *Journal of biomedical optics*, 15(2):021314–021314, 2010.

[190] Ashley P. Tregaskiss, Adam N. Goodwin, Linda D. Bright, Craig H. Ziegler, and Robert D. Acland. Three dimensional ct angiography: A new technique for imaging microvascular anatomy. *Clinical Anatomy*, 20(2):116–123, 2006.

[191] Tzu-Hsiu Tsai, Jih-Shuin Jerng, and Pan-Chyr Yang. Clinical applications of transthoracic ultrasound in chest medicine. *Journal of Medical Ultrasound*, 16(1):7–25, 2008.

[192] Talat Uppal. Tissue harmonic imaging. *Australasian Journal of Ultrasound in Medicine*, 13(2):29–31, 2010.

[193] Luigi Vetrugno, Tiziana Bove, Giovanni Maria Guadagnin, Daniele Orso, Alessandro Brussa, and Giovanni Volpicelli. Advances in lung ultrasound in critically ill patients. *Journal of Emergency and Critical Care Medicine*, 3(0), 2019.

[194] Storti Via G, Gulati E, Neri G, Mojoli L, and Braschi A F. Lung ultrasound in the icu: from diagnostic instrument to respiratory monitoring tool. *Minerva Anestesiol.*, 78(11):1282–1296, 2012.

[195] O M Viessmann, R J Eckersley, K Christensen-Jeffries, M X Tang, and C Dunsby. Acoustic super-resolution with ultrasound and microbubbles. *Physics in Medicine & Biology*, 58(18):6447, 2013.

[196] OM Viessmann, RJ Eckersley, Kirsten Christensen-Jeffries, MX Tang, and C Dunsby. Acoustic super-resolution with ultrasound and microbubbles. *Physics in Medicine & Biology*, 58(18):6447, 2013.

[197] G Volpicelli, M Elbarbary, M Blaivas, DA Lichtenstein, G Mathis, AW Kirkpatrick, L Melniker, L Gargani, VE Noble, G Via, A Dean, JW Tsung, G Soldati, R Copetti, B Bouhemad, A Reissig, E Agricola, JJ Rouby, C Arbelot, A Liteplo, A Sargsyan, F Silva, R Hoppmann, R Breitkreutz, A Seibel, L Neri, E Storti, and T Petrovic. International liaison committee on lung ultrasound (ilc-lus) for international consensus conference on lung ultrasound (icc-lus). international evidence-based recommendations for point-of-care lung ultrasound. *Intensive Care Med*, 38(4):577–591, 2012.

[198] B. P. Watt, J. M. Burnfield, E. J. Truemper, T. W. Buster, and G. R. Bashford. Monitoring cerebral hemodynamics with transcranial doppler ultrasound during cognitive and exercise testing in adults following unilateral stroke. In *2012 Annual International Conference of the IEEE Engineering in Medicine and Biology Society*, pages 2310–2313, Aug 2012.

[199] WR Webb. Thin-section ct of the secondary pulmonary lobule: anatomy and the image–the 2004 fleischner lecture. *Radiology*, 239(2):322–38, 2006.

[200] MO Wielpütz, CP Heußel, FJ Herth, and HU Kauczor. Radiological diagnosis in lung disease: factoring treatment options into the choice of diagnostic modality. *Dtsch Arztebl Int.*, 111(11):181–187, 2014.

[201] James Wiskin, Bilal Malik, Rajni Natesan, and Mark Lenox. Quantitative assessment of breast density using transmission ultrasound tomography. *Medical Physics*, 46(6):2610–2620, 2019.

[202] Law W.K., L.A. Frizzell, and F. Dunn. Determination of the nonlinearity parameter b/a of biological media. *Ultrasound in Medicine & Biology*, 11:307–318, 1985.

[203] Desailly Y, Tissier AM, Tanter M Correas JM, Wintzenrieth F, and Couture O. Contrast enhanced ultrasound by real-time spatiotemporal filtering of ultrafast images. *Physics in Medicine & Biology*, 62:31–42, 2017.